A Determination of the Electroweak Quark Couplings Using Final State Photon Emission in Z^0 Decays

DISSERTATION

zur Erlangung des Doktorgrades
des Fachbereichs Physik
der Universität Hamburg

vorgelegt von
Petra Hüntemeyer
aus Georgsmarienhütte

Hamburg 2001

Gutachter der Dissertation: Prof. Dr. A. Wagner
Prof. Dr. B. Naroska
Gutachter der Disputation: Prof. Dr. A. Wagner
Prof. Dr. F.-W. Büßer

Datum der Disputation: 30. 05. 2001

Dekan des Fachbereichs Physik und
Vorsitzender des Promotionsausschusses: Prof. Dr. F.-W. Büßer

Abstract

The final state photon radiation off the quark is measured with the OPAL detector at LEP in the reaction $e^+e^- \rightarrow Z^0 \rightarrow$ hadrons $+ \gamma$. The observed number of events with photons as well as the jet rates in such events are compared with results of a matrix element calculation of the order $\mathcal{O}(\alpha\alpha_s)$. The value for the strong coupling constant in first order $\alpha_s^{(1)} = 0.177^{+0.038}_{-0.015}$ is determined. Combining the measurement of the partial width of hadronic Z^0 decays with a final state photon with the total hadronic width of the Z^0 allows to determine the electroweak coupling of up- and down-type quarks. The resulting values are

$$c_{up-type} = 1.107^{+0.166}_{-0.095} \qquad \text{and} \qquad c_{down-type} = 1.508^{+0.063}_{-0.111}.$$

They correspond to the partial decay widths

$$\Gamma_{up-type} = 286^{+43}_{-24}\text{MeV} \qquad \text{and} \qquad \Gamma_{down-type} = 390^{+17}_{-29}\text{MeV}.$$

The values are in good agreement with the Standard Model predictions.

Zusammenfassung

Die Photonabstrahlung vom Quark in der Reaktion $e^+e^- \rightarrow Z^0 \rightarrow$ Hadronen $+ \gamma$ wird mit dem OPAL-Detektor bei LEP gemessen. Die Anzahl von Ereignissen mit Photonen und die Jet-Raten in solchen Ereignissen werden mit den Ergebnissen einer Matrixelement-Berechnung der Ordnung $\mathcal{O}(\alpha\alpha_s)$ verglichen. Daraus wird der Wert für die starke Kopplungskonstante in erster Ordnung, $\alpha_s^{(1)} = 0.177^{+0.038}_{-0.015}$, bestimmt. Die Kombination der Messung der partiellen Breite von hadronischen Z^0-Zerfällen mit einem Endzustandsphoton mit der Gesamtbreite der hadronischen Z^0-Zerfälle erlaubt die Bestimmung der elektroschwachen Kopplungen von Up- und Down-type Quarks. Die sich ergebenden Werte sind

$$c_{up-type} = 1.107^{+0.166}_{-0.095} \qquad \text{und} \qquad c_{down-type} = 1.508^{+0.063}_{-0.111}.$$

Sie entsprechen den partiellen Zerfallsbreiten

$$\Gamma_{up-type} = 286^{+43}_{-24}\text{MeV} \qquad \text{und} \qquad \Gamma_{down-type} = 390^{+17}_{-29}\text{MeV}.$$

Die Werte stimmen gut mit der Vorhersage des Standardmodells überein.

Contents

Chapter 1

Introduction

The photon is well known as the quantum of light and as the exchange particle of electromagnism. It received its name in 1926, when the chemist Gilbert N. Lewis wrote in a letter to the editor of the science magazine Nature: "I therefore take the liberty of proposing for this hypothetical new atom, which is not light but plays an essential part in every process of radiation, the name photon." [1] As the exchange boson of the electromagnetic interaction the photon mediates the force between electric charges. The present measurement utilises the photon coupling to the electric charge to measure the couplings of another exchange particle: the Z^0 boson. The Z^0 boson is one of the exchange particles of the weak interaction. Both particles are mediators of forces which are described in the framework of the Standard Model of elementary particle physics. The Standard Model consists of theories which are able to describe three of four fundamental forces, which have been identified in nature: electromagnetism, weak and strong interactions. One of its integral parts is the theory of strong interactions (Quantum Chromodynamics, QCD [2–5]), the other is the theory of electroweak interactions unifying electromagnetic and weak interactions in one model. The latter was developed by Glashow, Salam and Weinberg [6–8] in the 1960s. In the picture of these theories the forces are mediated by vector bosons: the gluons which mediate the strong force, the photon and the Z^0 boson, mentioned above, and the $W^\pm$ mediating the electromagnetic and the weak forces. While the gluons and the photon are massless, the Z^0 and the $W^\pm$ are massive bosons (a fact which led to the introduction of the mass generating Higgs formalism in the Standard Model [9]). All the bosons are listed with their masses in table 1.1. It is possible to learn about the nature of the forces by studying the couplings of their exchange bosons to the matter particles. The matter particles in the Standard Model picture are grouped in three families or generations of fermions: there are three lepton doublets (ν_e, e^-; ν_μ, μ^-; ν_τ, τ^-) and three quark doublets, where each

Gauge bosons	Mass (GeV)
γ	0
$W^\pm$	80.419 ± 0.056
Z^0	91.188 ± 0.002
gluons	0

Table 1.1: The masses of the fundamental gauge bosons taken from [10]. The usual convention $\hbar = c = 1$ is used here and in the following.

quark is referred to a quark flavour: u(p), d(own); c(harm), s(trange); t(op), b(ottom). The quarks u, c, and t, which have a third component of the weak isospin of 1/2, are called up-type quarks, the quarks d, s, and b, which have a third component of the weak isospin of −1/2 are called down-type quarks. The weak isospin is the charge of the weak interaction. For every lepton and quark an antiparticle exists, which has the same properties except for opposite signs of the charge-like quantum numbers.

In the present analysis, the nature of the electroweak interaction is studied in the framework of the Standard Model performing a measurement of the Z^0 couplings to fermions and antifermions. The massive Z^0 boson can be produced at a high rate in e^+e^- annihilations, given that the centre-of-mass energy at which electron and positron react approximately equals the Z^0 mass. The massive Z^0 boson is unstable and decays into quarks or leptons. Measuring the final states of such reactions, $e^+e^- \rightarrow Z^0 \rightarrow f\bar{f}$, allows an insight in the nature of the coupling of the weak neutral current to other particles. General observables sensitive to the electroweak couplings of fermions are decay widths of the Z^0 boson into quarks and leptons as well as forward-backward charge asymmetries and polarisation asymmetries for various final states of a Z^0 decay. Experimental techniques to access these observables for quark flavours in the case of heavy quarks species are based on the exploitation of the different masses and lifetimes of the c- and b-quarks. The progress in the identification and separation of the latter in recent years mainly resulted from high-precision vertex detectors which were installed in the new colliding beam experiments at the beginning of the 1990s and which were gradually improved during the years of operation. The vertex detectors permitted the reconstruction of secondary vertices of long-lived heavy quarks, thereby supplying a direct method of heavy-flavour 'tagging'. Light flavour tagging (u-,d-,s-quarks) is more difficult, however several methods have been developed, identifying high-energy hadrons and using these as flavour tag.

In this thesis, a measurement of the partial Z^0 decay widths into up- and down-type quarks is presented using an alternative approach. As mentioned in the beginning, it utilises the immanent property of the photon coupling to the electric charge. The electric charge of up-type quarks u, c, and t is +2/3, that of down-type quarks d, s, and b is −1/3. Thus, by selecting hadronic Z^0 decays with final state photons radiated off the quark or antiquark, a subsample can be extracted which is enriched in up-type quarks since the strength of the coupling is proportional to the squared charge. Combining the measured rates of hadronic events with radiated final state photons with the total rate of hadronic Z^0 decays permits the simultaneous determination of the electroweak couplings of up-type and down-type quarks. However, compared to the previously mentioned analyses dealing with either heavy or light quark flavours the present one determines the electroweak coupling of up- and down-type quarks for the flavour admixture present on the Z^0 resonance.

There are several places around the world where the studies of the electroweak sector of the Standard Model have taken place and are still ongoing. One of these is the Large Electron-Positron Collider (LEP) of CERN in Geneva. It was operated in two phases, LEP1 (1989-1995) and LEP2 (1995-2000). During phase 1, reactions at energies around the Z^0 mass were studied and electroweak parameters became accessible with a precision never reached before. During phase 2, centre-of-mass energies of up to 209 GeV have been reached, the highest energy in e^+e^- collisions achieved so far. Main issue of the research during both phases was to precisely measure all couplings which describe the interactions within the Standard Model. A very important task of LEP1 was to determine the coupling of the neutral current to the fermions. The centre-of-mass energies at LEP2 permitted to extract the self coupling of the vector bosons. All these studies provided a primary examination of the Standard Model theories and any significant deviation between its predictions and the measurements would have been a hint for 'new' physics.

The present work focuses on LEP1, where a large amount of data was collected. It still provides the input for various interesting precision analyses performed within the four collaborations which have maintained the four detectors ALEPH, DELPHI, L3 and OPAL. The Z^0 production started in 1989, when about 20 Z^0 decays per experiment were detected in a *pilot* physics run. Between that time and 1995 the data of more than 5 million Z^0 decays, approximately 70% of which were decays into hadronic final states (reactions of the form $e^+e^- \rightarrow Z^0 \rightarrow q\bar{q}$), were collected by each experiment. The whole hadronic data set taken by the OPAL experiment between 1989 and 1995 has been available for the present analysis.

The thesis is organised as follows. Chapter 2 introduces the theoretical framework in which final state photon radiation in hadronic decays at the Z^0 peak is treated. Matrix element calculations allowing to describe final state radiation exactly in a predefined phase space region are presented. The extraction of the electroweak couplings with the help of these matrix elements requires a short discussion of the limitations in perturbative QCD calculations of a fixed order and of the implications for the value of the strong coupling constant. The evolution of hadronic final states in Z^0 events is described in the last part of the chapter. Chapter 3 gives an overview of the OPAL detector, with emphasis on the electromagnetic calorimeter, the main instrument for reconstructing photons. The method which is used to identify photons with the electromagnetic calorimeter is described in more detail in Chapter 4, where its performance is compared to its simulation. The analysis is presented in Chapter 5. After having explained how interesting events are selected, a discussion of background sources and of the signal detection and selection efficiencies follows. Particular emphasis is put on the neutral hadron/γ-separation with the electromagnetic calorimeter. Systematic uncertainties are discussed in detail. The measured photon rates are compared to the matrix element predictions presented in Chapter 2 and the electroweak coupling constants are determined. Finally, the observed results are discussed and compared to other measurements. Chapter 6 summarises the results of the work presented in this thesis.

Chapter 2

Final State Radiation in Multihadronic Z^0 Decays

One of the two lowest order Feynman diagrams for the process studied in this thesis, the photon bremsstrahlung off quarks in Z^0 decays is shown in figure 2.1(a). The data analysed are taken at a centre-of-mass energy of $\sqrt{s} \approx m_{Z^0}$, where the Z^0 exchange graph is dominant.

Final states photons are, as was discussed in the previous chapter, a probe to study the composition of the hadronic final states at the Z^0 resonance. The main difficulty in exploiting this probe is that the process of final state radiation competes with the production of photons from initial state radiation – that is, the radiation of photons off the incoming leptons. Events taken at the Z^0 resonance have the interesting property that the rate of FSR is much enhanced relative to the one of ISR, which is suppressed. This is shown in figure 2.2.

In this plot, the total cross-sections of e^+e^- reactions at centre-of-mass energies $\sqrt{s}$ in the range between 40 and 180 GeV as measured and predicted by OPAL [11] are shown, in comparison with the relative contributions to prompt photon production by the three different sources in such reactions as calculated in Born approximation by Laermann, Walsh, Schmitt, and Zerwas [12]. The prompt photon rate depends on the radiation of photons off the incoming leptons (ISR), off the outgoing quarks (FSR) and on the interference between both processes (for the initial state radiation contribution see the Feynman graph to lowest order in figure 2.1(b)). As can be seen in the bottom plot of figure 2.2, the relative contribution by final state radiation reaches a maximum if the centre-of-mass energy equals the Z^0 mass, corresponding to the relative initial state radiation contribution reaching a minimum. The relative contribution by the interference term is small on the Z^0 peak changing its sign from negative to positive. The behaviour of the prompt photon production yield can be explained by the total cross-section depicted in the top plot of figure 2.2. On the resonance the cross-section is enhanced by about three orders of magnitude. The probability to produce a $q\bar{q}$ final state is much increased, with a resulting much larger rate of final state photons. Changing the centre-of-mass energy to be slightly above or below the resonance reduces the contribution of final state photons relative to the initial state photons drastically. At the same time, because of the much increased contribution of final state photons at the Z^0 resonance, the importance of the interference becomes negligible. Moreover, the mediating Z^0 has a finite life time, and therefore the initial

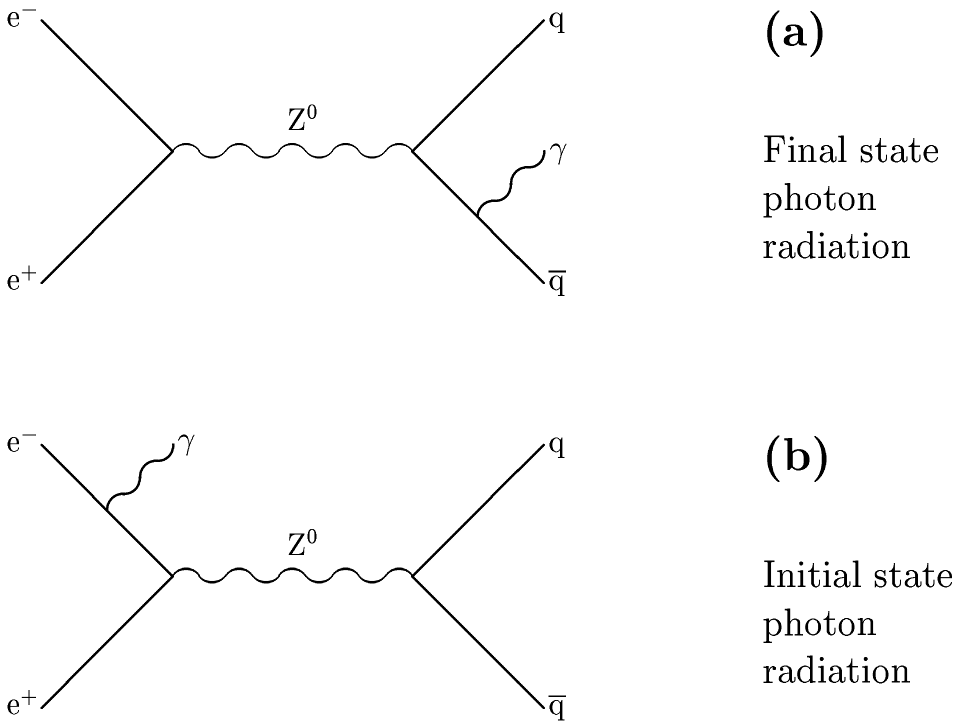

Figure 2.1: Feynman graphs showing prompt photon production to lowest order in Z^0 events: (a) final state radiation (FSR); (b) initial state radiation (ISR).

state radiation is decoupled from the final state radiation as long as the energy of the observed photon is greater than the Z^0 width of $\Gamma(Z^0)$ =2.49 GeV (which as we will see applies to the present analysis). Note that the relative contributions to prompt photon production shown in figure 2.2 are calculated for a restricted polar angle range of the photon of $|\cos\theta| < 0.7$[1] [12]. To summarise, the prompt photon production in e^+e^- annihilations on the Z^0 resonance (in an angular range of $|\cos\theta| < 0.7$) is dominated by final state radiation, so that at LEP one has the unique opportunity to measure real photons produced by FSR directly.[2]

In the following, the theoretical description of large angle photon radiation off quarks will be discussed. The parametrisation of this process in order to develop flexible simulation programs (Monte Carlo generators) will be presented. Such a generator allows to compare the measured photon rates and distributions in data with reliable theoretical predictions. The resulting restriction of the phase space in which a theory-compatible measurement may be performed is

---

[1] compare to the selection cuts in this analysis as listed in 5.1.2

[2] At lower energies, evidence for photon radiation off quarks in the final state of e^+e^-annihilations was provided by ealier measurements at the PEP storage ring at SLAC and the PETRA storage ring at DESY [13–15]. However, for the reasons discussed above it was not possible to measure directly the final state photon rate. The analyses at that time exploited a charge asymmetry of the quarks with respect to the electron direction in the events which is an effect of the interference between initial and final state radiation.

also discussed. A description of the extraction of the strong coupling constant α_s in first order then follows. Its value is used as an input for the measurement of the electroweak coupling constants c_u and c_d. In the last section, some general explanations are given concerning the evolution of hadronic Z^0 decays and their description in the framework of phenomenological models as they are implemented in commonly used Monte Carlo generators. The section, which may be regarded as belonging to the more technical side of the analysis, but which is also closely linked to the theoretical aspects of FSR in Z^0 decays, is completed by a short remark on the application of jet finder algorithms in such events.

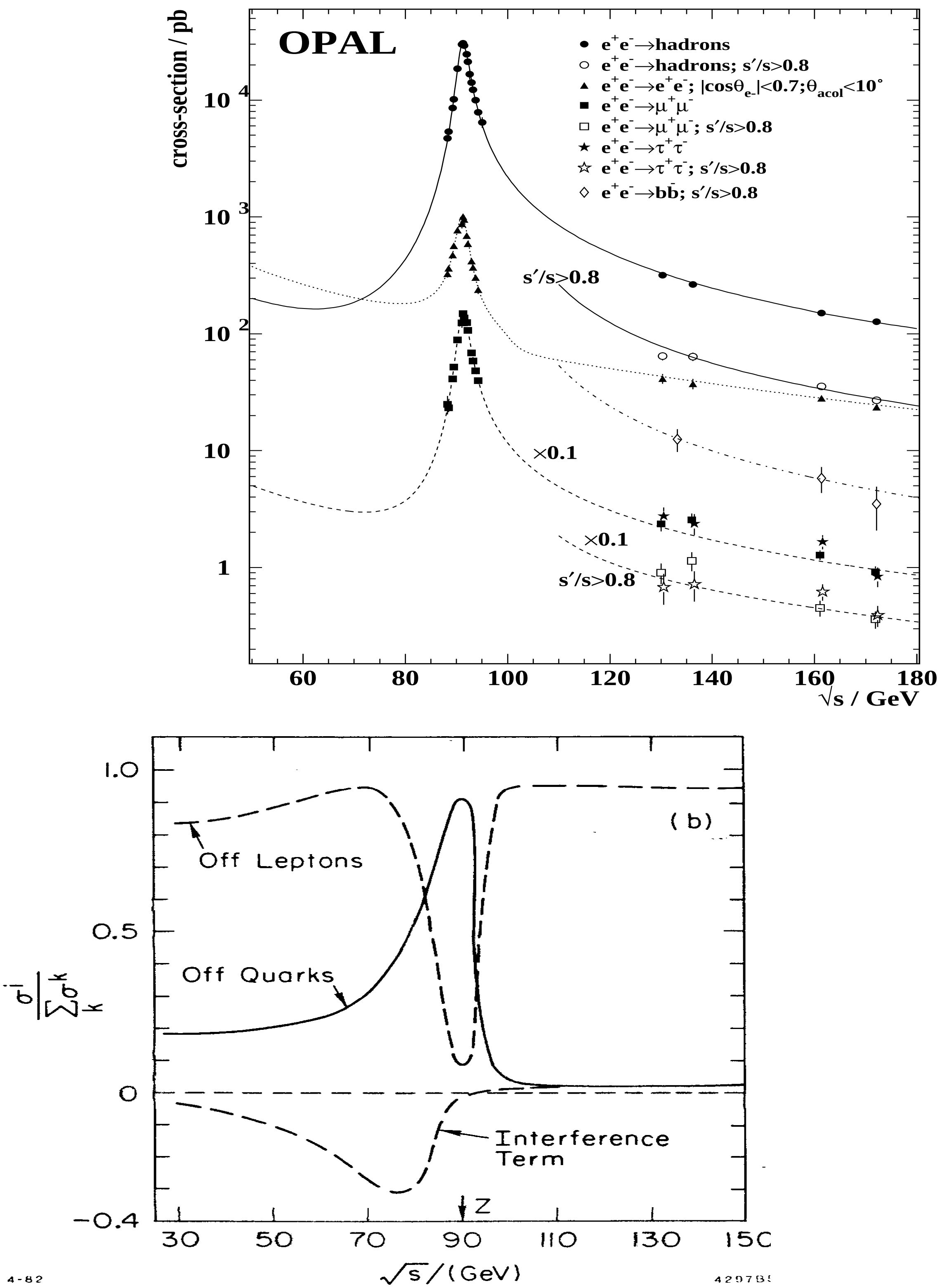

Figure 2.2: Top plot: the total cross-section for different final states in e$^+$e$^-$annihilations for centre-of-mass energies between 40 and 180 GeV as measured and predicted by OPAL [11]; bottom plot: the relative contribution $\sigma^j(q\bar{q}\gamma)/\sum_k \sigma^k(q\bar{q}\gamma)$ of FSR (off quarks), of ISR (off leptons), and of the interference term between both [12].

2.1 Theoretical Approaches to Describe Final State Radiation in Z^0 Decays

2.1.1 Theoretical Basis

There are two different categories of photon radiation off final state quarks in e$^+$e$^-$ annihilations which are distinguished by the transverse momentum of the radiated photon with respect to the radiating quark. The first category is large angle photon radiation resulting in hard photons isolated from the hadronic rest of the event. The second category is photon radiation within a small cone around the radiating quark. This classification is a consequence of the QCD description of inclusive photon production in e$^+$e$^-$$\rightarrow$ *hadrons.* The photon has a hadronic component, which is reflected by the appearance of collinear photon-quark singularities in the framework of a perturbative treatment of such a process. However, according to the 'factorisation theorem' [16–18], well defined cross-sections in perturbative QCD in all orders of α_s may be obtained by subtracting these singularities and absorbing them in quark-to-photon fragmentation functions. Such fragmentation functions calculated in leading-order QCD [19,20] and the inclusive prompt photon energy spectra they predict are found to be in agreement with measured data [21, 22]. Figure 2.3 shows the energy spectrum of prompt photons as measured in [22] in comparison with predictions from various parametrisations and extensions of [19, 20].

In the present work, only isolated photons of the first category will be studied and used to measure the electroweak coupling constants. Restricting the measurement to isolated photons allows to use exact matrix element calculations of the Standard Model theories. In the following, the theoretical basis of isolated photon radiation in Z^0 decays will be explained.

The coupling of the weak neutral current mediated by the Z^0 boson has two components: the vector and the axial vector component

$$g_v^f = I_3^f - 2 \cdot q_f \sin^2\theta_W, \tag{2.1}$$

$$g_a^f = I_3^f, \tag{2.2}$$

where I_3^f is the third component of the fermion's weak isospin, q_f is the fermion charge, and θ_w is the weak mixing or Weinberg angle. $\sin^2\theta_W$ has been measured with great precision at the Z pole. According to a global fit to all data performed by the LEP electroweak working group $\sin^2\theta_W = 0.23117 \pm 0.00016$ [10]. Both components, g_v^f and g_a^f can be combined to the electroweak coupling constant

$$c_f = 4 \cdot \left((g_v^f)^2 + (g_a^f)^2\right). \tag{2.3}$$

The standard model values for the vector coupling, the axial vector coupling, and their combination obtained in the case of Z^0 decaying into quark and antiquark are listed in table 2.1. For completeness, the couplings for leptons are also shown. Thus, the total hadronic width of

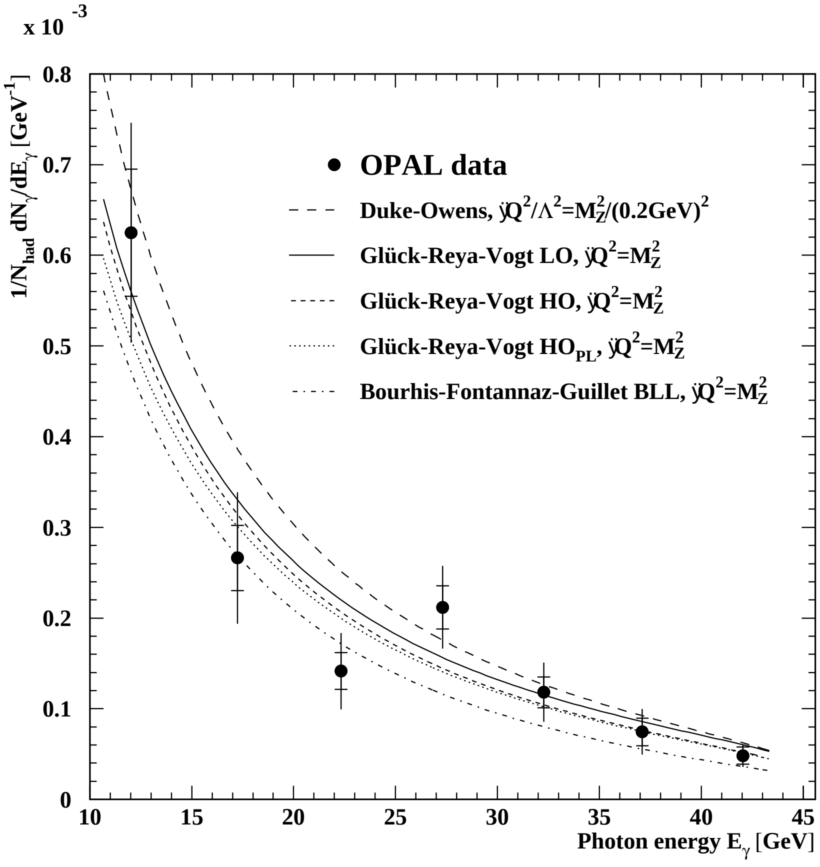

Figure 2.3: The energy spectrum of prompt photons measured in hadronic Z^0 decays [22] and various theoretical predictions [23–26].

f	q_f	g_v^f	g_a^f	c_f
uc	2/3	0.192	0.5	1.148
dsb	-1/3	-0.346	-0.5	1.477
e$\mu\tau$	1	-0.038	-0.5	1.004
ν	0	0.5	0.5	2

Table 2.1: The electroweak couplings of quarks and leptons as calculated within the standard model using $\sin^2\theta_W$=0.231 [10]. The fermion charge q_f is given in units of the electron charge. (See text for further explanations.)

the Z^0 can be expressed as a function of the electroweak coupling constants as

$$\Gamma(\mathrm{Z}^0 \to \mathrm{hadrons}) = \frac{G_F m_{\mathrm{Z}^0}^3}{24\sqrt{2}\pi} N_C K_{QCD}(2c_u + 3c_d). \tag{2.4}$$

Here, G_F is the Fermi constant, m_{Z^0} is the Z^0 mass, and the factor $N_C = 3$ is due to the colour charges of the quarks.

$$K_{QCD} = 1 + \frac{\alpha_s}{\pi} + 1.409\frac{\alpha_s^2}{\pi^2} - 12.77\frac{\alpha_s^3}{\pi^3} \tag{2.5}$$

represents the universal part of the QCD corrections for massless quarks with α_s being the strong coupling constant at $\sqrt{s} = m_{Z^0}$ [10]. The indices of the electroweak coupling constants c_u and c_d denote up(u)-type quarks (u,c) and down(d)-type quarks (d,s,b), respectively.[3] The factors in front of them count the number of u- and d-type quarks which can be produced at the available energy.

The partial width of hadronic Z^0 decays with a photon radiated off one quark in the final state is given by

$$\Gamma(Z^0 \to \text{hadrons} + \gamma) = \frac{G_F m_{Z^0}^3}{24\sqrt{2}\pi} N_C F \frac{\alpha}{2\pi}(q_u^2 2c_u + q_d^2 3c_d), \tag{2.6}$$

where F is a correction factor determined in perturbative calculations of a limited order in α and α_s. Equation 2.6 may be established by treating photon radiation in a similar way to gluon radiation.[4] It may be derived from equation 2.4 using the second term of the QCD corrections in 2.5 and replacing the strong coupling constant α_s by the electromagnetic coupling constant α. Moreover, the photon, as mediating boson of the electromagnetic interaction, couples to the electric charge which is reflected in the factors q_u^2 and q_d^2 in front of the electroweak coupling constants in equation 2.6: $q_u^2 = 4/9$ and $q_d^2 = 1/9$ are the charges squared of up- and down-type quarks, respectively.[5] As a consequence, the probability for bremsstrahlung off up-type quarks is higher by a factor of four than the probability for bremsstrahlung off down-type quarks. This is exploited by the presented analysis to measure the electroweak couplings c_u and c_d or correspondingly the partial decay widths of the Z^0 into up- and down-type quarks: Γ_u and Γ_d. Earlier measurements using the photon as tag for up-type quarks are based on fewer data [27–32].

As mentioned before, the exact perturbative treatment of final state radiation involves restrictions of the phase space to regions in which the theoretical calculations predict finite cross-sections for the considered processes. To be more precise, photon and gluon singularities arising in the framework of perturbation theory have to be excluded by isolation cuts.

An additional complication emerges because the theoretical calculations are performed on the level of partons. Ad hoc, the parton level topology is not comparable to the event structure generated by stable hadrons or particles as they are measured with the detector. On the level of hadrons and on the level of detected particles, the situation is more complicated, since one faces on average 30 four-vectors, compared to a usually much smaller number of four-vectors on the parton level, which in the case of the description with the aid of perturbative calculations moreover is limited by the fixed order. It is desirable to put the four-vectors on all levels in a similar structure, to find a region of the phase space where the detector level corresponds more closely to the parton level.

---

[3] At the considered energies a decay into top quarks is kinematically forbidden.

[4] Both are massless bosons with spin 1, and negative parity.

[5] Charges are always given in units of the electron charge.

A consistent description of both, the allowed phase space region and the event structure, matching theory and experiment, is achieved by using jet finder algorithms. They are applied to the four-vectors on every level combining partons, stable hadrons, and measured objects in clusters or jets. A Z^0 decay is counted as event with isolated FSR if the photon it produces is isolated from these jets.

There exists a variety of jet finder philosophies. Widely used are jet finder algorithms based on the so-called y separation or resolution parameter [33–36],

$$y_{ij} = \frac{M_{ij}^2}{s}, \tag{2.7}$$

where $\sqrt{s}$ is the centre-of-mass energy, and M_{ij} may be the invariant mass of two objects i and j or the minimum transverse momentum of one object with respect to the other one. In the considered case, on parton level, these objects can be for example the partons and a photon at the end of a parton shower. As suggested by G. Kramer and B. Lampe, in principle a photon is accepted as isolated if $y_{\gamma i} > y_{cut}$ for all partons i of the event.[6] On the basis of this jet-finder-like definition, they provide a pertubative calculation of the partial width of $Z^0 \rightarrow hadrons + \gamma$ decays which thus becomes y_{cut}-dependent, but can be compared relatively easily to a measurement on detector level:

$$\Gamma(Z^0 \rightarrow n\text{Jets} + \gamma)(y_{cut}) = \frac{G_F m_{Z^0}^3}{24\sqrt{2}\pi} N_C F(y_{cut}) \frac{\alpha}{2\pi} (\frac{4}{9} 2c_u + \frac{1}{9} 3c_d). \tag{2.8}$$

The appropriate y_{cut}-dependent corrections $F(y_{cut})$ are determined by matrix element calculations, which will be further explained in the following section.

2.1.2 Matrix Element Calculations and Monte Carlo

Matrix elements in general give energy, momentum or angular dependent probabilities for the transition of an initial state $|i\rangle$ to a final state $|f\rangle$. The observables of such transitions (e.g. cross-sections) can be predicted based on a calculation of the matrix elements. The advantage of matrix element calculations is, that they allow an exact treatment of the physics process, without any model assumptions. The disadvantage is, that in practice they are limited to a fixed order in the parameters of the perturbation theory. Accordingly, the description of photon radiation in decays of the type $Z^0 \rightarrow q\bar{q}$ with matrix element calculations is deduced from first principles of QED and QCD, but at the same time is of limited order in α and α_s. As a result, the number of particles in the final state which can be theoretically described is limited, too. Matrix element calculations are therefore unable to describe in detail the properties of complete multihadronic final states. However, they are powerful in describing the properties of highly energetic, large angle final state radiation, which usually occurs at an early stage of a Z^0 decay. Matrix element calculations thus allow a model independent extraction of the electroweak

---

[6] Kramer and Lampe used methods and results from their preceding publication where they calculated jet cross-sections up to the order $O(\alpha_s^2)$. They just replaced one gluon in their calculation by a photon and removed the colour factors accordingly. In other words, they interpreted the photon as an 'electromagnetic jet'. [37]

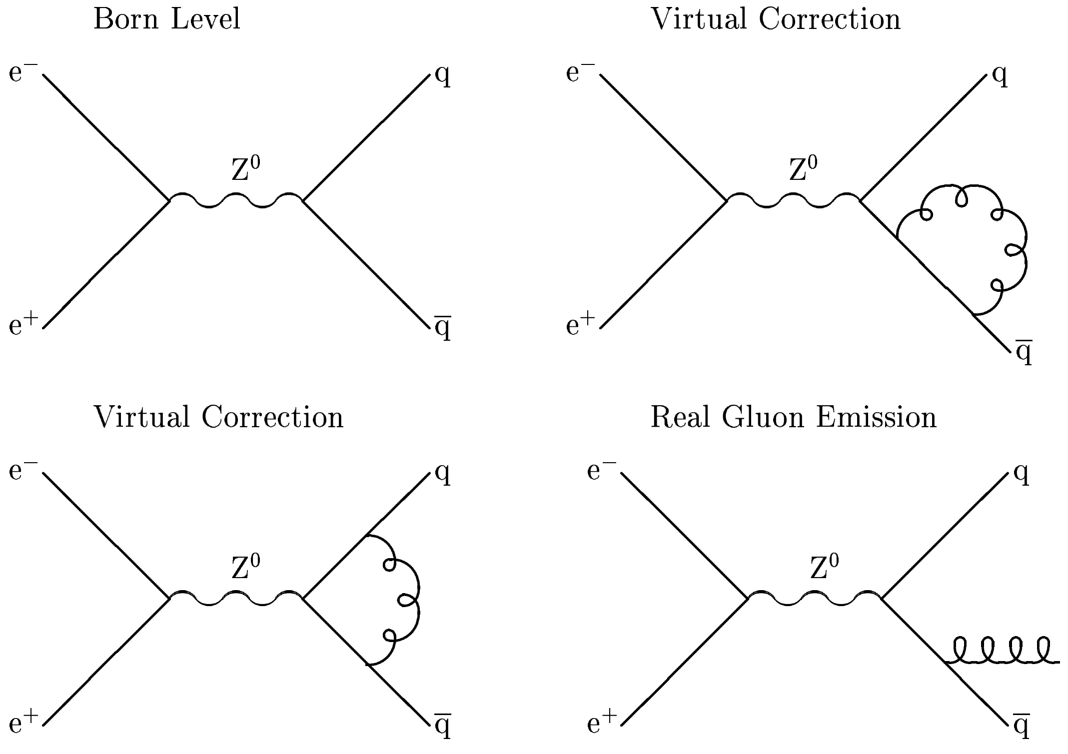

Figure 2.4: Some typical Feynman diagrams contributing to the QCD corrections as implemented in $\mathcal{O}(\alpha\alpha_s)$ matrix element calculations of the FSR cross-section in Z^0 decays.

coupling constants, since they provide an exact prediction of the final state photon rate, at least in regions of the phase space where they are known to yield an adequate description.

Several approaches exist to describe isolated hard photon radiation in e^+e^- annihilation in general and on the Z^0 peak in particular [12,37–43]. Matrix element calculations treating hard and isolated final state photon radiation in Z^0 decays are available up to the order $\mathcal{O}(\alpha\alpha_s)$. They are able to describe final states of up to three partons plus one photon produced in e^+e^- annihilations at a centre-of-mass energy of $\sqrt{s} = M_{Z^0}$. The computed Feynman graphs corresponding to the $\mathcal{O}(\alpha_s)$ QCD corrections are depicted in figure 2.4. Contributions from two final states enter in the partonic cross-section:

$$e^+e^- \to Z^0 \to q\bar{q}\gamma, \tag{2.9}$$

and

$$e^+e^- \to Z^0 \to q\bar{q}g\gamma. \tag{2.10}$$

The differential cross-section of the first contribution in lowest order ($\mathcal{O}(\alpha)$) is proportional to the inverse of the scaled invariant masses squared between the photon and the quark resp. antiquark, which is defined as a function of their four momenta p_i, p_j and of the centre-of-mass energy $\sqrt{s}$,

$$y_{ij} = \frac{(p_i + p_j)^2}{s}, \qquad i = q, \bar{q}, \quad j = \gamma. \tag{2.11}$$

In the next-to-leading order additional gluon loop corrections are introduced, so that

$$\frac{d^2\sigma^{(1)}(q\bar{q}\gamma)}{dy_{q\gamma}dy_{\bar{q}\gamma}} \sim \frac{M^{(0)}_{q\gamma}}{y_{q\gamma}} + \frac{M^{(0)}_{\bar{q}\gamma}}{y_{\bar{q}\gamma}} + virt.\ corr. \tag{2.12}$$

The cross-section contribution by the second final state $\mathrm{Z}^0 \to q\bar{q}g\gamma$ generated by real gluon emission from the quark or antiquark can be written as

$$d\sigma^{(1)}(q\bar{q}g\gamma) = \left(\frac{M^{(1)}_{q\gamma}}{y_{q\gamma}} + \frac{M^{(1)}_{qg}}{y_{qg}} + \frac{M^{(1)}_{\bar{q}\gamma}}{y_{\bar{q}\gamma}} + \frac{M^{(1)}_{\bar{q}g}}{y_{\bar{q}g}} \right) dPS(4), \tag{2.13}$$

where $M^{(1)}_{ij}$ are functions of the scaled invariant masses y_{kl} between the partons or between a parton and the photon. $dPS(4)$ denotes the 4-particle phase space over which to integrate [44]. In the above expressions, it can be seen that the cross-section of the photon production in hadronic decays diverges in the framework of perturbation theory for soft photons or for photons which are radiated collinear to the quark or antiquark ($y_{q\gamma}, y_{\bar{q}\gamma} = 0$) as well as for soft or collinear gluon radiation ($y_{qg}, y_{\bar{q}g} = 0$). Therefore, two steering cut-off parameters are introduced and in the gluonic case a so-called 'phase space slicing method' is applied.[7] In the matrix element Monte Carlo GNJETS [39], which is used in the present analysis, the cut-off parameters are y_γ and y_0:

- $\boldsymbol{y_\gamma}$ is the cut-off in the phase space of the photon emission and is used to remove the singularity of the $y_{q\gamma}, y_{\bar{q}\gamma}$ poles. In the matrix element calculations, it is required that

  $$y_{q\gamma}, y_{\bar{q}\gamma} \geq y_\gamma. \tag{2.14}$$

- $\boldsymbol{y_0}$ is chosen such that the gluonic singularities cancel the virtual corrections in the $q\bar{q}\gamma$ cross-section so that finite results are derived. For

  $$y_{qg}, y_{\bar{q}g} < y_0 \tag{2.15}$$

  a $q\bar{q}g\gamma$ event is interpreted as $q\bar{q}\gamma$ event.[8] The corresponding differential cross-section is integrated over the phase space region $y_{qg}, y_{\bar{q}g} \leq y_0$ including the (anti)quark-gluon poles and combined with the virtual gluon loop cross-section of $q\bar{q}\gamma$. The resulting cross-section is y_0-dependent but the dependence disappears as soon as the $q\bar{q}g\gamma$ cross-section for

  $$y_{qg}, y_{\bar{q}g} \geq y_0 \tag{2.16}$$

  is added.

---

[7] Beside the 'phase space slicing method' which is used in the matrix element based Monte Carlo GNJETS [39] other techniques exist to cancel singularities in a perturbative calculation. Whereas the calculations of [40] employ a slightly modified 'phase space slicing method', in reference [41] a different procedure is applied called 'subtraction method'. This method is independent of a 'slicing' cut, but depends on other unphysical parameters (see [41] for details).

[8] The gluon is 'hidden' inside the quark jet [44].

		lower limit	upper limit
limits of theoretical calculation	y_γ y_0	$5 \cdot 10^{-4}$ -	10^{-3} 10^{-5}
range of comparison between	y_{cut} (Durham)	0.006	0.1
photon rates in data and GNJETS	y_{cut} (Jade E0)	0.02	0.2

Table 2.2: An overview of the y parameters relevant for the calculation of the $n\ jet + \gamma$ cross-section in the matrix element Monte Carlo GNJETS. The y_{cut} as defined by the Durham and the Jade jet finder scheme will be specified in section 2.3.4.

If a jet finder is applied to the partonic topology of a Z^0 event plus final state photon computed with matrix element probabilities, it must be guaranteed that the calculated $n\ jet+\gamma$ cross-sections are not y_0-dependent. This means that the transition behaviour between the $n\ jet+\gamma$ cross-sections determined in the 3-particle and 4-particle phase space has to be steady in the limit $y_{qg}, y_{\bar{q}g} \rightarrow 0$. It can be shown that, as a consequence, a perfect photon isolation from the gluon cannot be required in the $q\bar{q}g\gamma$ case. A cut $y_{g\gamma} \geq y_\gamma$, i.e. a restriction of the phase space for gluon emission, would weaken the y_0 dependence of the cross-section calculated in the 4-particle phase space whereas the y_0 dependence of the cross-section calculated in the 3-particle phase space remains unchanged. This asymmetric treatment of the 3-particle and the 4-particle cases would make the combined result of the integration y_0-dependent. The photon isolation in the 4-particle phase space is thus ensured by the cuts

$$y_{\bar{q}\gamma}, y_{qg\gamma} \geq y_\gamma \qquad \text{and} \qquad y_{q\gamma}, y_{\bar{q}g\gamma} \geq y_\gamma, \tag{2.17}$$

where $y_{ijk} = (p_i + p_j + p_k)^2/s$ with $i, j, k = q, \bar{q}, \gamma$.

Both cut-off parameters were studied for GNJETS in [44]. y_γ and y_0 were varied over a certain range and 'safe' regions of the phase space boundaries were found. The upper limits of y_γ and y_0 have to be chosen such that there is no bias introduced in the computation of the cross-sections. This is ensured by avoiding that the phase space boundaries of the matrix element calculation cut into the analysed phase space in data which is defined by the chosen y_{cut} values. The lower limits are defined by both physical and technical limitations of the matrix element calculation. The lower limit of y_γ is fixed by the fact that higher order corrections which are not implemented in GNJETS become important for very small values of y_γ. Moreover, if $M_{q\gamma} = \sqrt{y_{q\gamma}}\sqrt{s}$ is of the order of the hadron mass scale, non-pertubative QCD effects which are not included in the $\mathcal{O}(\alpha\alpha_s)$ calculations can play an important role. For y_0, the upper limit is not only chosen to be far away from the boundaries of the analysed phase space in data but also to take into account that terms vanishing with $y_0 \rightarrow 0$ have been neglected in the matrix element calculations of GNJETS. The lower limit of y_0 is due to technical reasons and determined by the size of the statistical fluctuations of the Monte Carlo integration near the $qg, \bar{q}g$ poles.[9] The values for y_γ, y_0, and the y_{cut} within which the n jet + photon rates are computed are summarised in table 2.2.

---

[9] More details on the Monte Carlo generation using matrix element calculations, especially concerning their phase space boundaries, can be found in [44].

The alternative ansatz, the treatment of final state radiation off quarks in the framework of phenomenological parton shower models, on which multi-purpose event generators in particle physics are based, is described in subsection 2.3.1.

2.2 Interpretation of FSR Cross-sections using Matrix Elements

In the previous section, the definition of the phase space region in which the matrix element calculations yield reliable results was described. Another parameter of the matrix element calculations which needs to be fixed before they can be applied for the determination of the electroweak couplings is the strong coupling constant α_s in first order. The following section discusses how a value of $\alpha_s^{(1)}$ is fixed. Subsequently, the relevant expressions of the relations between the rate of photon radiation in hadronic Z^0 events and the electroweak couplings are given.

2.2.1 Fixing the Strong Coupling Constant

As mentioned above, matrix element calculations, e.g. GNJETS, are only available in the first order of α_s. A value for $\alpha_s^{(1)}$ is is fixed in the present analysis by comparing the selected data with the matrix element predictions for various values of $\alpha_s^{(1)}$.

The strong coupling constant $\alpha_s^{(1)}$ affects the total photon rate as well as the relative proportions of two and three jet rates, whereas the electroweak coupling constants only affect the total rate. Three jet events are due to a gluon emission by a quark, where both partons could be resolved as separate jets, so that the ratio

$$R_{23}^{\gamma} = \frac{\sigma_{3jet+\gamma}}{\sigma_{2jet+\gamma} + \sigma_{3jet+\gamma}}, \tag{2.18}$$

is a measure for the strong coupling constant $\alpha_s^{(1)}$. It is determined in data and then compared to the ratios R_{23}^{γ} derived with the $\mathcal{O}(\alpha\alpha_s)$ matrix element Monte Carlo GNJETS for various values of $\alpha_s^{(1)}$.[10] The value which produces the best fit of the ratio R_{23}^{γ} in data and GNJETS Monte Carlo is taken as reference value for $\alpha_s^{(1)}$. This reference value is chosen as input for GNJETS to calculate the corrections $F(y_{cut})$ appearing in equation 2.8. As the matrix element calculations are only of first order α_s and thus describe final states of three partons at most, the validity of its predictions for the $n\ jet$ rate proportions is restricted to y_{cut} ranges, where the number of selected FSR events with more than 3 jets is small. Moreover, one has to keep in mind that the value for α_s is only extracted in first order. The R_{23}^{γ} measurement together with the presented matrix element predictions does not provide a direct access to a higher order and thus more precise value of the strong coupling constant.

---

[10] As the calculation is only of first order, it has no explicit dependence on the renormalisation scale.

2.2.2 Measuring the Electroweak Coupling Constants

As can be inferred from the expressions 2.4 and 2.8, the measurement of the total hadronic width of the Z^0 and the measurement of the partial width of hadronic Z^0 decays with a highly energetic, large angle photon emitted in the final state before fragmentation allows a determination of the electroweak coupling constants c_u and c_d defined by equation 2.3. The total hadronic width is measured in analyses independent from the present one, so that the partial width for hadronic Z^0 decays with FSR can be extracted by the rate of such decays normalised to the number of multihadronic Z^0 decays. Since the $\mathcal{O}(\alpha\alpha_s)$ corrections to the partial width are calculated y_{cut}-dependently, the partial width itself as calculated with the available matrix element Monte Carlos becomes y_{cut}-dependent. Therefore, the final state photon rate in hadronic Z^0 decays also has to be measured y_{cut}-dependently. The measured partial width is given by

$$\begin{aligned}\Gamma(\mathrm{Z}^0 \to n\mathrm{Jets} + \gamma)(y_{cut}) &= \Gamma(\mathrm{Z}^0 \to \text{hadrons}) \times \frac{N_{\mathrm{Z}^0\to(n\mathrm{Jets}+\gamma)}(y_{cut})}{N_{\mathrm{Z}^0\to\mathrm{Hadrons}}} \\ &= \Gamma(\mathrm{Z}^0 \to \text{hadrons}) \times R_{\mathrm{Z}^0\to(n\mathrm{Jets}+\gamma)}(y_{cut}). \end{aligned} \tag{2.19}$$

From 2.4 and 2.6 one derives for c_u and c_d,

$$c_u = \left(\frac{3\pi R_{\mathrm{Z}^0\to(n\mathrm{Jets}+\gamma)}(y_{cut})}{\alpha F(y_{cut})} - \frac{1}{6K_{QCD}}\right) \times \frac{\Gamma(\mathrm{Z}^0 \to \text{hadrons})}{h} \tag{2.20}$$

and

$$c_d = \left(-\frac{2\pi R_{\mathrm{Z}^0\to(n\mathrm{Jets}+\gamma)}(y_{cut})}{\alpha F(y_{cut})} + \frac{4}{9K_{QCD}}\right) \times \frac{\Gamma(\mathrm{Z}^0 \to \text{hadrons})}{h}, \tag{2.21}$$

where

$$h = N_c \frac{G_F m_{\mathrm{Z}^0}^3}{24\sqrt{2}\pi}. \tag{2.22}$$

Alternatively, the partial widths of the Z^0 decay into up- and down-type quarks might be calculated:

$$\begin{aligned}\Gamma_{up-type} &= \left(\frac{3\pi}{\alpha}\frac{K_{QCD}}{F(y_{cut})} R_{\mathrm{Z}^0\to(n\mathrm{Jets}+\gamma)}(y_{cut}) - \frac{1}{6}\right) \times \Gamma(\mathrm{Z}^0 \to \text{hadrons}), \\ \Gamma_{down-type} &= \left(-\frac{2\pi}{\alpha}\frac{K_{QCD}}{F(y_{cut})} R_{\mathrm{Z}^0\to(n\mathrm{Jets}+\gamma)}(y_{cut}) + \frac{4}{9}\right) \times \Gamma(\mathrm{Z}^0 \to \text{hadrons}). \end{aligned} \tag{2.23}$$

The expressions 2.20, 2.21, and 2.23 reflect the nature of the photon coupling to charge which is exploited as probe for Z^0 decays into up-type quarks versus down-type quarks. As can be seen, the coupling c_u of the Z^0 to the up-type species and relatedly $\Gamma_{up-type}$ depends linearly on the FSR rate in hadronic events. Note that K_{QCD} is known to $\mathcal{O}(\alpha_s^3)$, whereas the corrections $F(y_{cut})$ are computed to $\mathcal{O}(\alpha_s)$. The values of c_u and c_d as well as of $\Gamma_{up-type}$ and $\Gamma_{down-type}$ shall be calculated in y_{cut} regions where the theoretical and experimental uncertainties are small. This is the intermediate sector of the global y_{cut} range which is fixed by the matrix element calculations explained in section 2.1.2. Further discussions concerning this will follow in chapter 5.

2.3 Hadronic Final States at LEP 1

The final state evolution of an event like $e^+e^-\rightarrow$ *hadrons* at LEP 1 is subdivided into three phases: the perturbative parton shower phase, the non-perturbative fragmentation (or hadronisation) phase, and the hadron decay phase. These three phases are treated in the following sections.
An alternative approaches to the previously mentioned matrix element calculations is given by the parton shower models for hadronic Z^0 decays. These models are usually used in the simulation of hadronic Z^0 events with Monte Carlo event generators. To be able to compare the measured photon yield with the yield of photons given by the matrix element calculations on parton level, the parton shower model based event generators are also used in the present analysis to estimate the efficiencies of the photon rate measurement and to correct for them. Parton shower models are therefore explained in more detail.

2.3.1 Parton Shower Phase and Final State Photon Radiation

2.3.1.1 Theoretical Approaches

There exist two traditional approaches to describe the perturbative parton shower phase. The matrix element method, in which Feynman diagrams are calculated order by order, has been introduced in 2.1.2 The second possible method is the parton shower model approach.

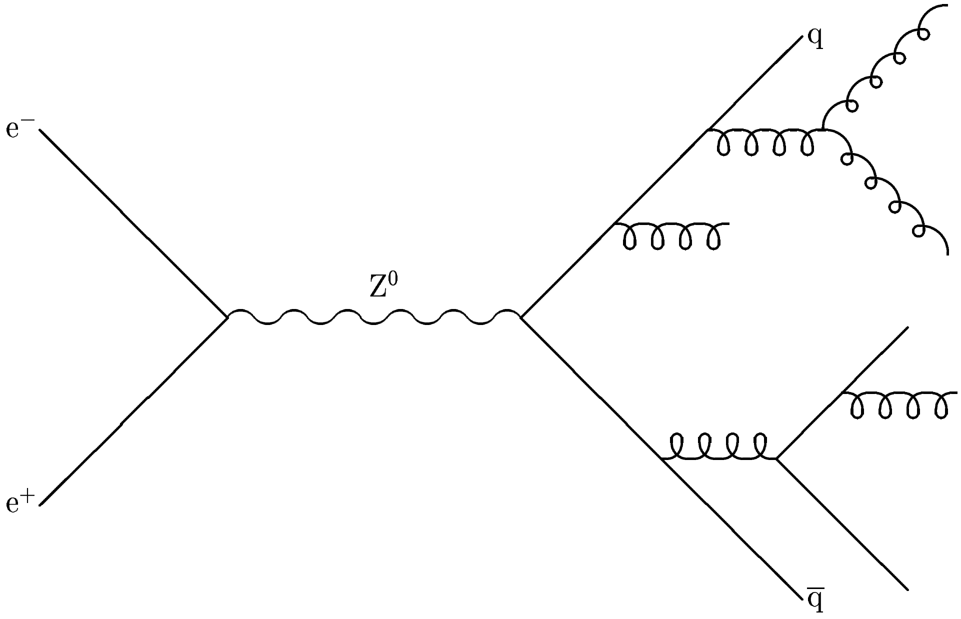

Figure 2.5: Schematic view of a parton shower evolution in a hadronic Z^0 decay. The primary q and $\bar{q}$ may radiate gluons which themselves may split into a $q\bar{q}$ pair or into further gluons.

A schematic view of the parton shower evolution in the final state of an e^+e^- annihilation is given in figure 2.5. For an arbitrary number of branchings $q \rightarrow qg$, $g \rightarrow gg$ or $g \rightarrow q\bar{q}$ as they occur in such a parton shower the exact matrix element ansatz is not suitable. The necessary higher order calculations using the exact matrix element ansatz become very complicated and difficult. Presently, matrix element calculations are in some cases available up to $\mathcal{O}(\alpha_s^3)$, e.g. for the total cross-section. For most purposes, however, they are limited to $\mathcal{O}(\alpha_s^2)$. Therefore, approximations with simplified kinematics, interference and helicity structures are used to calculate branching probabilities in a parton shower. The so-called leading logarithm approximation (LLA) is applied, which is formulated in terms of the kinematic parameters Q^2 and z: Q^2 is the virtuality scale or the square of the energy available for the branching, z generally expresses the fraction of the mother energy and momentum retained by the daughter parton. Only leading terms in Q^2 and z are considered in the perturbative expansions, subleading terms are neglected. Higher orders are taken into account effectively by evolving the shower iteratively with repeated branchings of one parton into two. This ansatz gives a good description of the substructure of jets and has the advantage that the shower picture can be easily implemented in Monte Carlo programs. The probability $\mathcal{P}$ for the branchings as enumerated above is given by the DGLAP equations [45–47]

$$\frac{d\mathcal{P}_{a\to bc}}{dt} = \int dz \frac{\alpha_s(Q^2)}{2\pi} P_{a\to bc}(z), \tag{2.24}$$

where

$$t = \ln(Q^2/\Lambda^2) \tag{2.25}$$

is the 'time' evolution parameter of the parton shower, and $P_{a\to bc}(z)$ are the so-called splitting kernels for the reactions quoted above:

$$\begin{aligned} P_{q\to qg} &= C_F \frac{1+z^2}{1-z}, \\ P_{g\to gg} &= N_C \frac{(1-z(1-z))^2}{z(1-z)}, \\ P_{g\to q\bar{q}} &= T_F n_f (z^2 + (1-z)^2). \end{aligned} \tag{2.26}$$

$C_F = 4/3$, $N_C = 3$, and $T_F = 1/2$ are called colour factors or Casimir factors and are determined by the properties of the symmetry group of QCD, SU(3). The third expression receives a contribution of $T_F = 1/2$ for each accessible $q\bar{q}$ flavour: $n_f = 5$. z is the fraction of the mother energy which is taken by the first partonic daughter (b), $(1-z)$ the fraction which is taken by the second daughter (c). The singularity near $z = 1$, which is associated with the emission of a 'soft' massless gluon, is properly handled with the aid of so-called '+ prescriptions' and $\delta(1-z)$ terms (further interpretation of the splitting functions can be found, for instance, in [48]).

2.3.1.2 Final State Photon Radiation

The implementation of photon radiation off the quarks in the parton shower model works analogously to the gluon radiation. The splitting kernel and branching probability are

$$P_{q\to q\gamma} = e_q^2 \frac{1+z^2}{1-z} \tag{2.27}$$

and

$$\frac{d\mathcal{P}_{q\to q\gamma}}{dt} = \int dz \frac{\alpha}{2\pi} P_{q\to q\gamma}(z). \tag{2.28}$$

Starting from the first equation in 2.26 and equation 2.24, the above equations can be deduced by replacing the colour factor C_F with the squared quark charge e_q^2 and the strong coupling constant α_s with the electromagnetic coupling constant in the Thomson limit ($Q^2 \to 0$): $\alpha = 1/137$. As can be seen, photon radiation, $q \to q\gamma$, and gluon radiation, $q \to qg$, are competing processes sharing the available energy.

2.3.1.3 Technical Aspects of the Shower Evolution and Monte Carlo Implementation

The evolution of a parton shower based on the splitting probabilities is implemented as follows. Starting with a maximum virtuality $t_{max} = \ln(Q^2_{max}/\Lambda^2)$ the 'time' evolution parameter t is reduced iteratively with the progressing parton shower. The probability that no branching occurs during a small interval δt is given by $(1 - \delta t d\mathcal{P}/dt)$. Therefore,

$$\mathcal{P}_{no-branching}(t_{max}, t) = \exp(-\int_t^{t_{max}} dt' \frac{d\mathcal{P}_{a\to bc}}{dt'}) \tag{2.29}$$

is the probability that a parton a has not yet branched at a 'time' $t < t_{max}$. It is derived as the product of the probabitilities that the parton did not branch in any of the small intervals δt between t_{max} and t. With $\delta t \to 0$ the no-branching probability becomes an exponential which yields the expression 2.29.[11] It is customary and convenient for Monte Carlo algorithms to define so-called Sudakov form factors [49], which give the probability that a parton of a defined maximum virtuality t reaches the value t_{min} without any branching:

$$S_a(t) = \exp(-\int_{t_{min}}^{t} dt' \int_{z_{min}(t')}^{z_{max}(t')} dz \frac{\alpha_s(Q^2)}{2\pi} P_{a\to bc}(z)). \tag{2.30}$$

The probability of no branching may by now be expressed in terms of the Sudakov form factors as follows:

$$\mathcal{P}_{no-branching}(t_{max}, t) = \frac{S_a(t_{max})}{S_a(t)}. \tag{2.31}$$

By introducing Sudakov form factors, which only depend on the 'time' evolution parameter t, one gets a structure for the parton shower formalism which can easily be implemented in the algorithms of Monte Carlo generators. Take for example the veto algorithm as implemented in JETSET [50]: The 'time' t at which a branching $a \to bc$ takes place is determined by generating a random number R according to a uniform distribution between 0 and 1, where

$$R = \mathcal{P}_{no-branching}, \tag{2.32}$$

---

[11] In fact, equation 2.29 is of a form which is familiar from radioactive decays.

which means

$$S_a(t) = \frac{S_a(t_{max})}{R} \tag{2.33}$$

The produced partons b, c then may branch further and so on. The branching will be stopped at the 'time' $t < t_{min}$ when $R < S_a(t_{max})$.

2.3.1.4 Parton Showers in JETSET and HERWIG and ARIADNE

The concept of time ordering according to some scale variable t as described above is common to the parton shower models as implemented in the Monte Carlo packages JETSET, HERWIG and ARIADNE, which are widely used to describe hadron production in e^+e^- collisions [50–52]. However, the definition of the variables Q, the virtuality scale of the shower evolution, and z, the fractional energy taken by the partons produced at each branching, as well as the scale of the running coupling α_s are different in each model. Moreover, ARIADNE utilises a colour dipole model (CDM) evolving the parton shower as a cascade of colour dipoles which emit gluons. This naturally leads to a different definition for the evolution variables compared to the parameters in JETSET and HERWIG. The respective differential dipole emission cross-sections deduced in the framework of the CDM are interpreted as modified DGLAP splitting kernels.

For each branching $a \to bc$ in JETSET as well as in HERWIG the energy and momentum splitting variable z in terms of which the DGLAP splitting functions 2.26 are expressed is defined by

$$E_b = zE_a \qquad \text{and} \qquad E_c = (1-z)E_a. \tag{2.34}$$

The evolution variable Q^2 in the JETSET shower is associated with the invariant mass squared of the mother parton of the branching, so that the time evolution parameter t defined by 2.25 can be expressed like $t = \ln(m_a^2/\Lambda^2)$. In JETSET, one thus gets for the evolution variable

$$Q^2 = m_a^2 = (p_a + p_c)^2 \approx E_b E_c (1 - \cos\theta_{bc}), \tag{2.35}$$

where $E_{b,c}$ and $p_{b,c}$ are the energies and four-vectors of the partons b and c, and θ_{bc} is the opening angle between them. The comparable expression in HERWIG is

$$Q^2 = E_a^2 \frac{p_b \cdot p_c}{E_b E_c} \approx E_a^2 (1 - \cos\theta_{bc}). \tag{2.36}$$

Applying the concept of time ordering,

$$t_i > t_{i+1} \qquad \text{or} \qquad Q_i > Q_{i+1}, \tag{2.37}$$

to the branching i and the successive branching $i+1$ it follows from equation 2.36 that the opening angle of a later branching is always smaller than the opening angle of an earlier one. By the angular ordering the HERWIG package approximates QCD coherence effects caused by the quantum mechanical interference between soft gluons. [12] But for the first emission, parts of the kinematically allowed phase space are completely excluded by this treatment. To be able to generate events in this region of the phase space (e.g. events with a photon or a gluon recoiling from a nearly collinear quark-antiquark pair) HERWIG reverts to matrix element calculations determining the emission rate in first order [53]. In the JETSET parton shower the splitting of the primary quark pair is also matched with first order matrix element calculations. With respect to the angular ordering the JETSET treatment of parton showers based on equation 2.35 can be viewed as the inverse of the HERWIG treatment. Here, the phase space is not reduced by angular ordering, which automatically follows from the time ordering, but coherence effects between gluons in jets are considered by rejecting gluon emissions with an openening angle which is greater than the angle of the preceding emission from the same parton [50].

The ARIADNE approach, already mentioned above, is different from the HERWIG and JETSET ones, which are both formulated in terms of perturbative QCD splitting functions. The parton shower in ARIADNE is based on the CDM and two partons (e.g. $q\bar{q}$) are taken as a colour dipole which emits a gluon. By this, one dipole is split up into two, composed of the gluon and each of the partons (e.g. qg and $\bar{q}g$). The produced dipoles are treated independently at the next stage when further gluons may be emitted. This procedure is repeated several times generating a cascade of independent dipoles and neglecting interferences between the individual emissions. There are three kinds of colour dipoles: $q\bar{q}$, qg (or $\bar{q}g$), and gg. The introduction of gluon splitting into $q\bar{q}$ in the framework of the CDM is not straightforward. Gluon splitting in the CDM can only be considered by computing the matrix element of $\mathcal{O}(\alpha_s^2)$ for the process $\mathrm{e}^+\mathrm{e}^- \to q\bar{q}q'\bar{q}'$. The four derived cross-sections are interpreted as modified DGLAP splitting kernels to which the parton shower formalism as described in the previous section can be applied. As evolution variable p_T is used, which is a measure for the transverse momentum of the emitted parton with respect to the colour dipole,

$$Q^2 = p_T^2 = S_{dip}(1 - x_1)(1 - x_3). \tag{2.38}$$

S_{dip} is the invariant mass squared of the emitting dipole, and $x_i = 2E_i/\sqrt{S_{dip}}$ are the final state energy fractions of the emission. The splitting variable z is replaced in ARIADNE with a variable y which is roughly the rapidity of the emitted gluon:

$$y = \frac{1}{2} \ln \frac{1 - x_1}{1 - x_3}. \tag{2.39}$$

The probability for having no emission is then calculated in terms of p_T^2 and y (see ARIADNE manual [52] for further details). By ordering the emission processes according to p_T^2 with $p_{T1}^2 > p_{T2}^2 > p_{T3}^2 > \ldots$ an angular ordering of the emissions is achieved automatically, and coherence effects between gluons are taken into account.

The bremsstrahlung of photons from quarks can be naturally introduced in the CDM picture. A $q\bar{q}$ pair is not only a colour dipole but also an electromagnetic dipole, and the cross-section for photon radiation has the same form as the one for gluon radiation. It is derived by substituting

---

[12] Such coherence effects are of particular importance in QCD, since gluons also carry colour charge. Further explanations may be found in [50].

the strong coupling α_s with the electromagnetic coupling α and the colour factor $C_F = 4/3$ with the squared quark charge.

Further differences exist between the three event generator packages, for instance in the definition of the QCD scale parameter Λ. These are discussed in more detail in the respective references [50–55].

Common to all three parton shower models is the definition of a lower cut-off parameter in the virtuality scale, Q_0, at which the parton emissions are stopped. The values for Q_0 are optimised so that the global event shapes resulting from the particular parton shower model show a good agreement with the event shapes in real data. Similarly, a cut-off parameter Q_0^γ is introduced defining the energy scale down to which photon emission is allowed in the parton shower. By default, Q_0^γ has the same value as Q_0. If for Q_0^γ a much lower value than for Q_0 was chosen, then at the end of a shower evolution, only photon emission would be allowed. Since photon and gluon radiation are competing processes, and the parton shower models are tuned to describe the hadronic event shapes, a measurement of the rate of isolated prompt photons (especially with energies down to a few GeV and emitted at large angles to the thrust axis [56]) provides a good test of the different models. Such measurements have been performed and indeed have revealed significant differences between the various parton shower models. The rate of prompt photons in hadronic final states as generated with JETSET is significantly underestimated, whereas HERWIG and ARIADNE describe the FSR yield well [30, 31, 57–59]. In [60], a large discrepancy between data and all three Monte Carlo models has been reported. They clearly underestimate the rate of final state photons for energies $E_\gamma < 4$ GeV. The reasons for this are not yet understood. In the present analysis, the different shower models are taken into account to estimate uncertainties in the efficiency correction of the measured yield of FSR photons with energies greater than 7 GeV.

2.3.1.5 Comparison of JETSET and the Matrix Element Monte Carlo GNJETS

It has been confirmed that the QCD shower model of JETSET, which will be used in the present analysis to calculate the efficiency corrections of the measurement (c.f. section 5.2.2), does not diverge significantly from the matrix element calculation of GNJETS. Results at the parton level of JETSET and results of GNJETS obtained with a value of $\alpha_s^{(1)} = 0.18$ are compared in figure 2.6, where the normalised distributions of the photon angle with respect to the closest jet and of the photon energy are shown for three different value of y_{cut} in the Jade E0 scheme. The photons are required to have an energy of more than 7 GeV. As pointed out in [44], QCD shower models are expected to correctly evolve a given parton configuration to the hadron level. From figure 2.6, it can be concluded that in general the parton shower model distributions reproduce the distributions resulting from the matrix element calculation well (deviations, in particular for $y_{cut} = 0.02$, are probably due to higher-order corrections as approximately implemented in shower models). The observed tendencies confirm the studies presented in [44]. Note however, that no cut on the photon energy has been applied there.

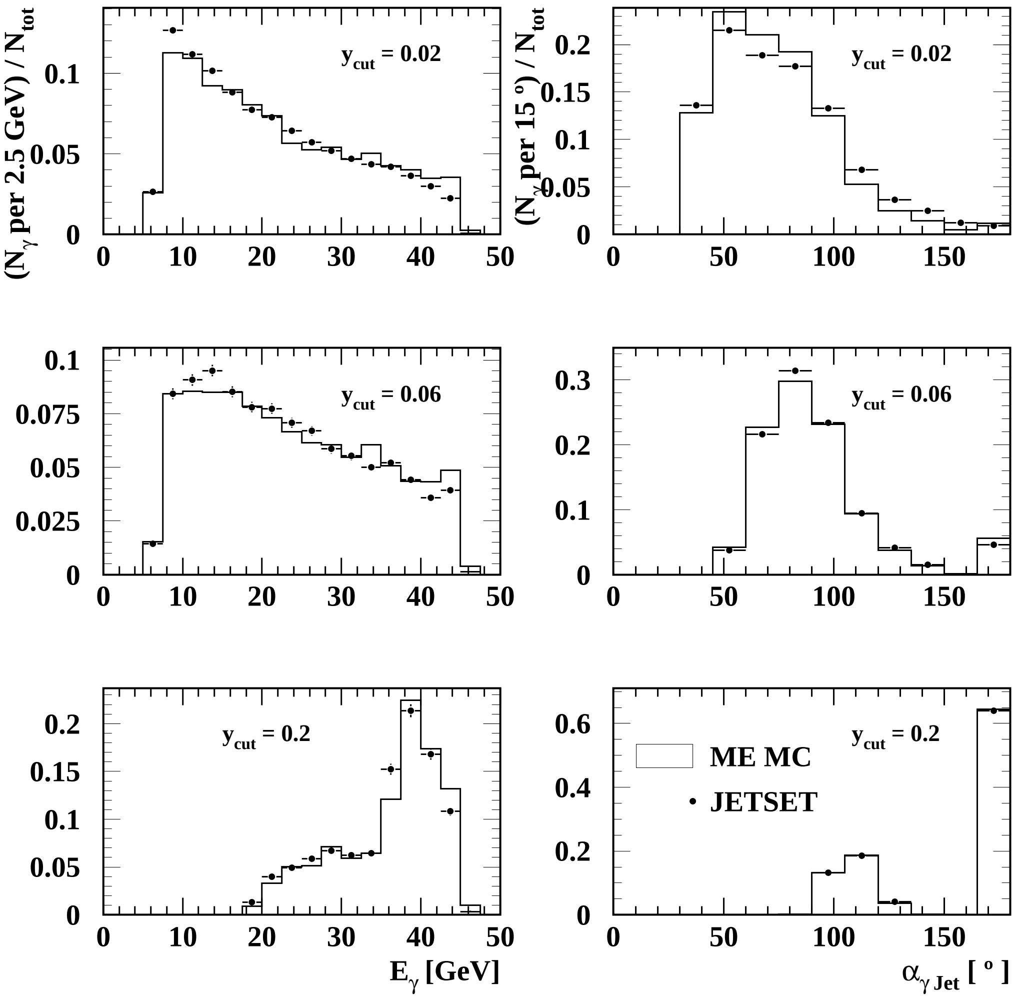

Figure 2.6: Photon energy (left column) and angle with respect to the closest jet are plotted for three different values of y_{cut} used in the jet finding with the JADE E0 scheme. The histogram represents the matrix element Monte Carlo results for $\alpha_s^{(1)} = 0.18$ (GNJETS), the points are derived with hadronic events on parton level generated with JETSET.

2.3.2 Fragmentation Phase

Processes are only calculable in perturbative QCD as long as α_s remains significantly smaller than unity. This is no longer satisfied as soon as the energy scale becomes $\mathcal{O}(1$ GeV). At this scale the partons finally start forming colourless hadrons. For the transition of partons into hadrons no perturbative description exists. To describe the fragmentation stage in a realistic manner phenomenological models based on stochastic, non-perturbative ansatzes are developed. These models can be classified in three different categories: independent, string and cluster fragmentation.

The `independent fragmentation` treats the hadronisation of each individual parton independently of all the other partons. The fragmentation of one parton jet is described within a sequence of iterative $q \rightarrow q' + hadron$ branchings. The energy and momentum sharing at each branching is given by a probability densitity or fragmentation function $f(z)$ with $z = (E + p_L)_{hadron}/(E + p_L)_{parton}$, where the longitudinal direction is defined by the parton. The fragmentation process is stopped when a certain model dependent energy bound is reached (cf. parton shower models).

The concept of `cluster fragmentation` was based on the assumption of 'preconfinement': every parton in coordinate and momentum space and its neighbouring parton build a colourless system which is identified as a cluster. This leads to a rather simple hadronisation model in which clusters are the basic units generated at the end of the parton shower evolution, which is ususally supplemented with forced non-perturbative splitting of the outgoing gluons $g \rightarrow q\bar{q}$. Moreover, large or heavy clusters are forced to fragment into smaller ones. The cluster units produced in such manner may be characterised by their mass and flavour. If they have masses of a few GeV, the cluster mass spectrum may be interpreted as a superposition of broad resonances which subsequently decay into hadrons.

The `string fragmentation` is a widely used model, which is based on the idea that when oppositely coloured partons move apart, the colour field between them can be viewed as a narrow flux tube of uniform energy density, which is stretched like a string between the partons. The transverse dimension of such a string is of the order of 1 fm. As the partons move further apart, the potential energy of the string rises linearly with the distance until the string finally breaks up in a new $q'\bar{q}'$ pair. Thus, two new colourless systems $q\bar{q}'$ and $q'\bar{q}$ are formed. As long as the invariant mass of the produced strings is large enough, further splittings may occur and generate further $q'\bar{q}'$ pairs. The different string breakings are thought of as disconnected events. To describe the energy and momentum distribution within such an event independent fragmentation functions $f(z)$ as mentioned above are used. These are calculated within phenomenological models which are designed such that they are able to describe the features of a particular type of fragmentation processes. A typical example of such a fragmentation function that fits experimental data is the Lund symmetric function for light flavours [61]

$$f(z) \propto \frac{(1-z)^a}{z} e^{-bm_T^2/z}, \tag{2.40}$$

where a and b are free parameters, and $m_T^2 = m^2 + p_T^2$ is the transverse hadron mass squared, which is calculated from the transverse momentum p_T and the mass of the produced $q\bar{q}$ pair. The Peterson function describes the fragmentation into hadrons containing the heavy flavours charm and bottom [62]

$$f(z) \propto \left(z \left(1 - \frac{1}{z} - \frac{\epsilon_q}{1-z} \right)^2 \right)^{-1}, \tag{2.41}$$

where ϵ_q is a free parameter relating different quark masses: $m_{q_1}^2 \epsilon_{q1} = m_{q_2}^2 \epsilon_{q2}$.

The HERWIG Monte Carlo generator utilises the procedure of cluster fragmentation. In the JETSET program package, two options are available, independent and string fragmentation, and for the presented studies the string option is chosen. The third Monte Carlo model, ARIADNE, utilises the JETSET software with the string option for the fragmentation of the partons.

2.3.3 Hadron Decay Phase

The last step in the evolution procedure is the phase of the formation of hadronic final states and the subsequent decay into stable hadrons. This phase is directly accessible by measurements. In Monte Carlo programs, it is usually simulated based on the available decay tables e.g. taken from the Particle Data Book [10].

2.3.4 Jet Finders and their Application in Events with Isolated Final State Photon Candidates

As established in section 2.1 it is desirable to have comparable event topologies in real data and in the partonic and hadronic phases simulated with Monte Carlos. In order to achieve this, and thus, to be able to finally compare the measured photon yields to the results of the exact matrix element computations described in 2.1, jet finder algorithms are applied to the collected data events and on every level of the generated Monte Carlo events. In the present analysis, two algorithms are chosen. Both are based on the jet resolution parameter y which is defined by equation 2.7. Differences between various y-based jet algorithms enter through the definition of the variable M_{ij}^2 in equation 2.7, and through the mode in which they combine the four-vectors of the particles. The two jet finders utilised in this analysis differ in the calculation of M_{ij}^2. In the framework of the Jade algorithm, M_{ij} is defined as an invariant mass [33, 34]:

$$M_{ij}^{2\ \mathrm{Jade}} = 2E_iE_j(1-\cos\alpha_{ij}), \tag{2.42}$$

where E_i and E_j are the energies of the particles or 'clusters' of already combined particles, and α_{ij} is the angle between them. A subsequently developed scheme is the Durham or k_T algorithm, where the invariant mass expression is replaced with the minimum transverse momentum of one particle with respect to the other [35, 36]:

$$\begin{aligned} M_{ij}^{2\ \mathrm{Durham}} &= 2\mathrm{min}(E_i^2, E_j^2)(1-\cos\alpha_{ij}) \\ &= \mathrm{min}(\frac{E_i}{E_j}, \frac{E_j}{E_i}) \quad M_{ij}^{2\ \mathrm{Jade}}. \end{aligned} \tag{2.43}$$

The two jet finder algorithms are chosen, since they yield the best agreement between jet rates and ratios on parton and hadron levels, which has been shown in several studies summarised in [63]. Moreover, the use of two different recombination schemes provides an estimate for the stability of the measurement against hadronisation effects.

The aim of any jet finder is to combine all particles (or 'clusters') into jets. In the present case, the particles may be partons (parton shower phase or parton level), stable hadrons (hadron decay phase or hadron level) or tracks and electromagnetic clusters visible in the detector (measurement or detector level). The jets are reconstructed in a recursive algorithm beginning with the particle pairing which yields the smallest y_{ij}. This pair is replaced by a new object which is the pseudoparticle k. The pseudoparticle k has the momentum $p_k = p_i + p_j$ and is now combined with the remaining particles in the same manner. This procedure is continued until y_{ij} exceeds a certain threshold value y_{cut} for any two of the clustered objects i,j. At the end of this procedure, the remaining clusters or pseudoparticles are called jets.

The specified jet finder algorithms can be applied to the products of hadronic Z^0 decays with isolated final state photons in two ways [44]. The first is the so-called 'democratic' approach where the jet finder is applied to the whole event including the photon. The jet containing the photon in this case is accepted as isolated photon if

$$\epsilon_{had} = \frac{E_{had}}{E_\gamma} < \epsilon_{cut}, \tag{2.44}$$

where E_γ is the energy fraction of the jet contributed by the photon, and E_{had} is the remaining energy. This ansatz considers the photon emission to be part of the shower process.
An alternative approach is a two-step procedure which breaks the 'democracy' between photon and partons (or fragmentation products on hadron/measurement level) [27, 29–32, 58, 64]. In the first step, the jet finder algorithm is applied to the Z^0 event excluding the photon. The hadronic part of the event is then resolved in a recursive procedure as it is described above using the jet resolution parameter

$$y_{ij} = \frac{M_{ij}}{E_{vis}}, \tag{2.45}$$

where E_{vis} is the total energy sum of all particles contributing to the jet reconstruction plus the photon energy. In a second step, the scaled invariant mass (Jade case) or the scaled minimum transverse momentum (Durham case) $y_{i,\gamma}$ between the photon and any reconstructed jet i is calculated. A photon is accepted as isolated if $y_{i,\gamma} > y_{cut}$ for all jets i of the event. Here, y_{cut} has the same value as in the first step of the jet definition. This reflects the correlation to the democratic approach and the previously mentioned interpretation of the photon as an 'electromagnetic' jet. The present analysis will make use of the two-step procedure.

2.4 Conclusion

In this chapter, the interesting possibility of studying final state photon radiation in hadronic decays at the Z^0 resonance has been presented. The relation between the final state photon rate and the electroweak couplings has been derived. It has been shown, that it is possible to treat FSR in the framework of matrix element calculations, but that nevertheless parton shower models are needed to estimate the efficiency corrections allowing to convert the measured FSR yield into the primary FSR yield at the parton level. The latter can be compared finally with the matrix element calculations.

Chapter 3

The Experiment

The analysis presented in this thesis is based on data which was taken during the years 1989-1995 by the OPAL [1] detector situated at the **L**arge **E**lectron **P**ositron storage ring (LEP) of the European Laboratory for Particle Physics CERN in Geneva. This chapter contains a short description of the high energy physics program of LEP and of the OPAL detector. Detailed descriptions of the OPAL Detector and its components can be found elsewhere ([65–81]).

3.1 The LEP Storage Ring and OPAL

OPAL is one among four detectors (ALEPH,DELPHI, and L3) at the LEP collider in Geneva (see figure 3.1) which has been in operation since 1989 colliding electrons and positrons at centre-of-mass energies around the Z^0 resonance (phase 1, called LEP1) and up to 209 GeV (phase 2 since 1995, called LEP2). Both, electron and positron beams were continuously accelerated in opposite direction to an energy of half the centre-of-mass energy. The four detectors were situated at four interaction regions where the electrons and positrons were driven into collision providing each experiment with about 4.5 million multihadronic Z^0 decays during the LEP1 phase. When LEP2 started in 1995 the centre-of-mass energy was increased gradually by installing superconducting cavities. During this phase energies were reached which allowed the production of real W pairs ($\sqrt{s} > 160$ GeV) and real Z^0 pairs ($\sqrt{s} > 183$ GeV). Until the end of the LEP operation a centre-of-mass energy of 209 GeV was reached, allowing shift the lower bound on the Higgs mass to a value of 113.5 GeV (at the 95% confidence level) by direct searches [82].
In the present analysis, data taken during the first phase of the LEP run are studied.

---

[1] **O**mni **P**urpose **A**pparatus for **LEP**

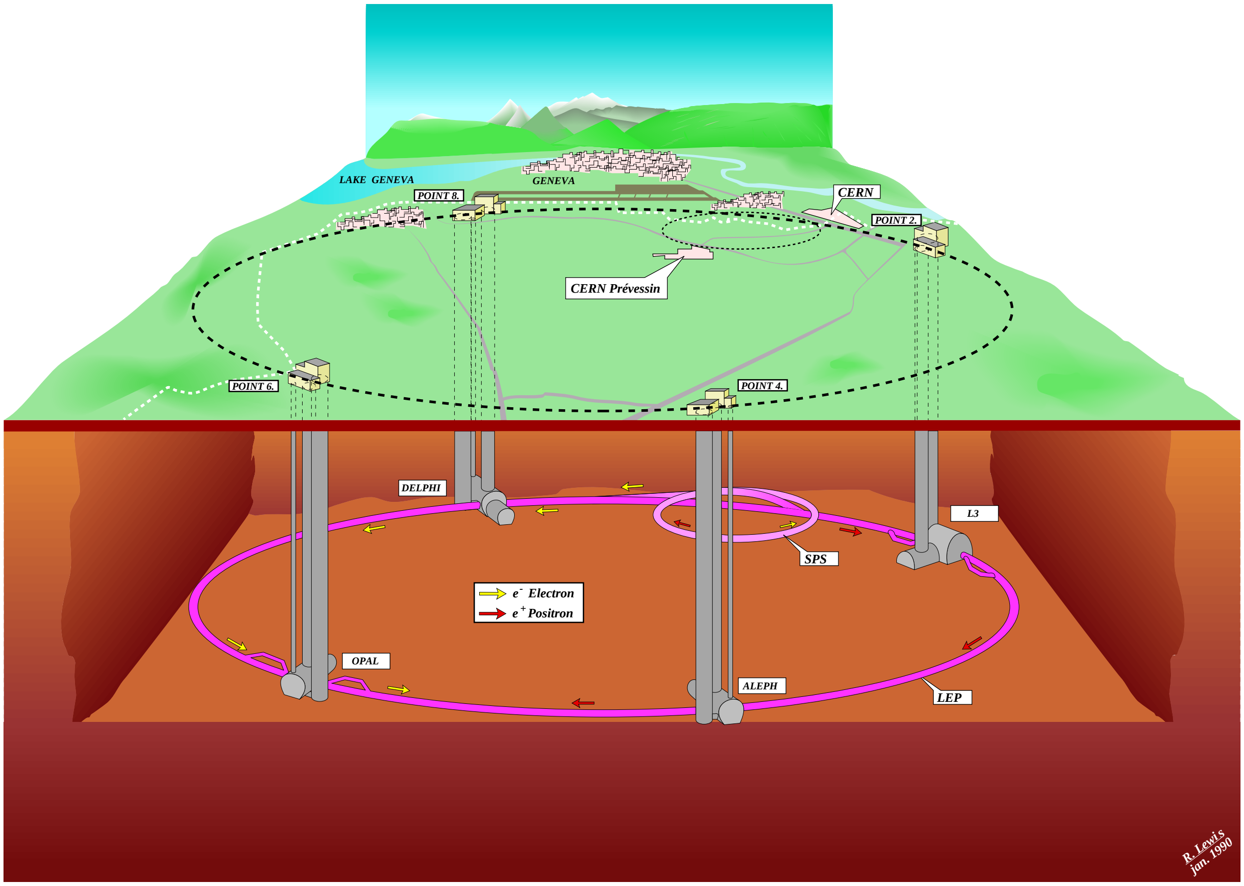

Figure 3.1: The LEP storage ring, situated approximately 100 m beneath the earth's surface, has a circumference of 26.7 km.

3.2 A Brief Description of the Most Important OPAL Detector Components

A perspective view of the OPAL detector can be seen in figure 3.2 along with a small coordinate system. There exist two commonly used reference systems:

The OPAL Master Reference System (MRS) is a 3D Cartesian Coordinate System whose origin is at the nominal interaction point and which has its z-axis along the nominal electron beam direction (this is anticlockwise around LEP when viewed from above). The x-axis is horizontal and directed towards the centre of LEP, leaving the y-axis as normal to the zx-plane. Since the detector and therefore the z-axis is inclined by 1.39 % with respect to the horizontal, it follows that the y-axis will be similarly inclined with respect to the vertical.

The other coordinate system is a polar one. It shares the z-axis with the MRS, the azimuthal angle ϕ is counted with respect to the x-axis, the polar angle θ with respect to the z-axis. As mentioned above the e^+ and e^- beams at LEP have the same energy, so all LEP detectors are symmetric relative to the xy- or $r\phi$-plane perpendicular cutting the beams at the nominal interaction point.

The design of the OPAL detector was chosen to provide an multi-purpose instrument for particle identification, momentum and energy measurement over nearly the full solid angle. As can be seen in figure 3.2 the components of the detector were arranged outside the beam pipe, in a layered structure, like the layers of an onion. In the following, the detector components responsible for track reconstruction, measurement of the hadronic energy, and muon identification are described briefly, beginning with the component nearest to the beam pipe. The components between the time-of-flight detector and the hadronic calorimeter in the barrel region, the presampler and the electromagnetic calorimeter will be treated in a seperate section as they are of special interest for the presented analysis.

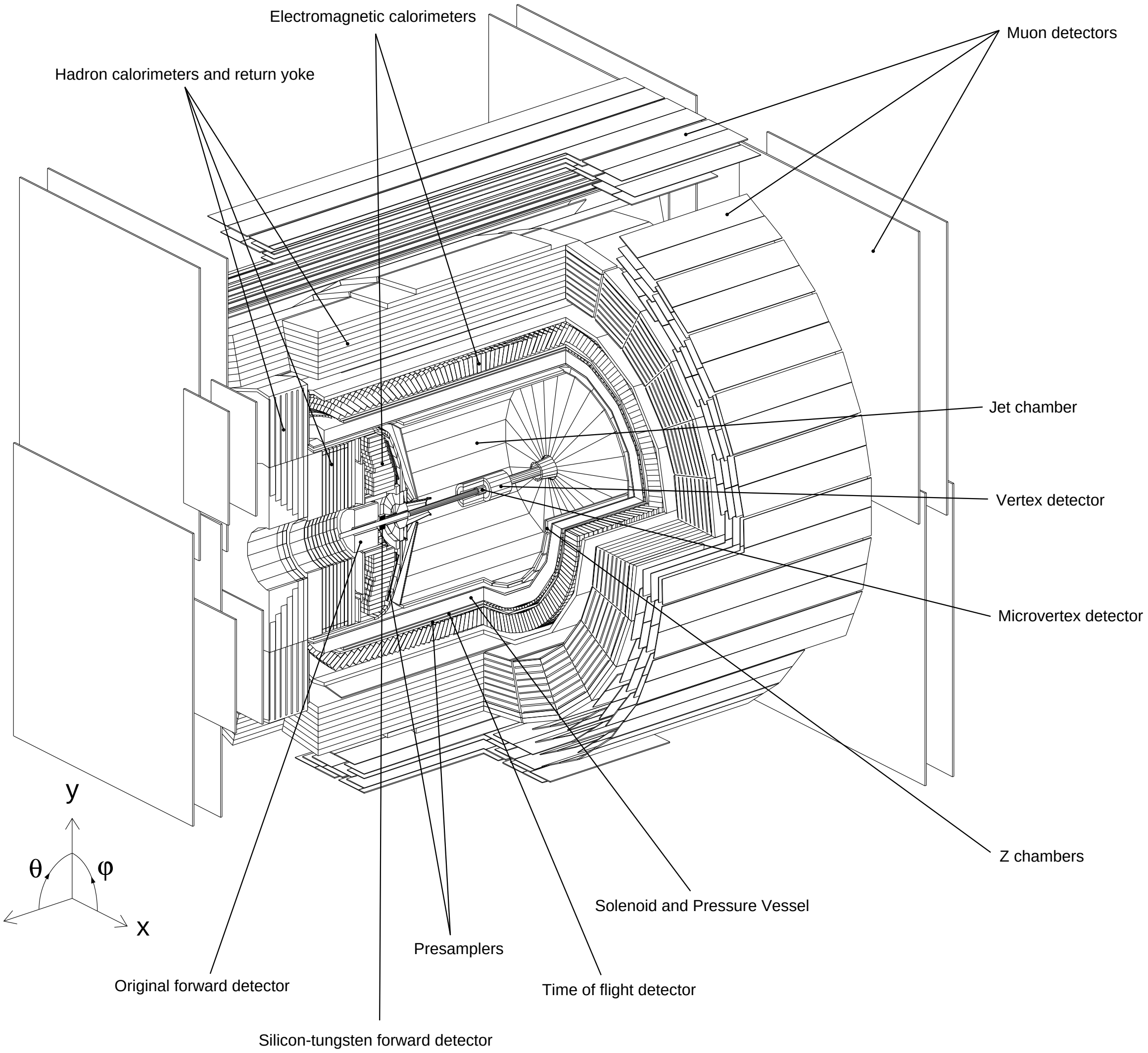

Figure 3.2: The OPAL detector

The Tracking System

The tracking system consisted of four components:

- the silicon microvertex detector

- the vertex detector
- the jet chamber
- the z chambers

`The Silicon Microvertex Detector`

The silicon microvertex detector mounted around the beam axis between the inner and outer beam pipe consisted of two concentric layers of silicon strip detectors with radii of 6.1 and 7.5 cm, respectively. It was installed in 1991 and since then it was upgraded two times. The detector originally consisted of 11 single-sided devices making up the inner layer and 14 single-sided devices making up the outer layer. Each of them is 18.3 cm long divided into 3 wafers providing geometrical acceptances of $|\cos\theta| < 0.83$ for the in inner layer and $|\cos\theta| < 0.77$ for the outer layer. The intrinsic spatial resolution of this detector configuration was about 10 μm in the $r\phi$-plane [66]. No spatial information in z direction was given by the microvertex detector until it was upgraded in 1993. During the winter shutdown 92/93, each single-sided device was replaced by two single-sided devices glued back-to-back delivering readout capabilities not only in the $r\phi$- but also in the z-plane where a spatial resolution of about 15 μm was reached [67]. In 1995 this component was upgraded once again increasing the number of ladders to 12 (inner layer) and 15 (outer layer) and inclining them to close the readout gaps in $r\phi$. Moreover, the outer layer was expanded from 3 to 5 wafers extending the angular coverage.

The main purpose of the microvertex detector was the reconstruction of the primary and secondary vertices[2].

`The Central Tracking System`

Surrounding the microvertex detector, the Central Chamber System consisted of three drift chambers as quoted above. The **vertex**, **jet**, and **z chambers** were installed inside a pressure vessel. The gas mixture in the chamber system consisted of argon (88.2%), methane (9.8%), and isobutane (2.0%). The pressure inside the vessel was chosen to be 4 bar. The value was a compromise in order to achieve a good particle identification through energy loss measurements, at the same time attaining small multiple scattering and therefore good spatial resolution. The three compontents of the central chamber system are briefly described now:

The **vertex chamber** was a drift chamber of 1 m length with an inner radius of 8.8 cm and an outer radius of 23.5 cm. It consisted of two components which were subdivided into 36 cells. In the inner part of the detector (ranging to a radius of 17.5 cm) each cell contained 12 'staggered'[3] signal wires parallel to the beam direction. These so-called axial cells delivered a spatial resolution in $r - \phi$ of 55μ and in z of 4 cm. The outer part of the central vertex chamber improved the z resolution. Its 36 so-called stereo cells each contained 6 signal wires which were oriented such that the angle between them and the axial wires is 4°. The combined information of axial and stereo wires improved the z resolution to 700 μm [68].
Before the intallation of the silicon microvertex detector, this detector had the tasked of reconstructing the primary and secondary vertices.

---

[2] The term secondary or displaced vertex denotes the reconstructed decay vertex of a short-lived particle originating from the interaction point of primary vertex.

[3] An explanation of this term is given when the jet chamber is described.

One of the main components of the OPAL Detector was the cylindrical **jet chamber**, with an inner radius of 25 cm, an outer radius of 185 cm, and a length along the beam direction of 4 m. It was a drift chamber providing a measurement of the momentum, the charge and the flight direction of a charged paricle. It played a substantial role in the geometrical event reconstruction. Moreover, the jet chamber as it was designed helped in identifying particles by their specific energy loss $\mathrm{d}E/\mathrm{d}x$ in the chamber gas exploiting the Bethe-Bloch formula (more detailed explanations concerning this concept can be found in [69]). Perpendicular to the beam axis, the jet chamber was subdivided into 24 sectors, so that every sector spanned an angle of 15°. Two adjacent sectors were divided by a plane of cathode wires, whereas in the centre ϕ position of each sector were 160 potential wires alternating with 159 signal wires, parallel to the beam axis. The signal wires are located 100 μm outside the anode wire plane, in alternating order. This is called 'staggering' and helped in resolving ambiguities in determining from which side of the anode wire plane a track has crossed the chamber. This design led to a maximum drift distance of 25.5 cm. The construction was terminated by conical end plates, so that the length of the wires varied between 3.44 m for the innermost one and 4.12 m for the outermost one. The configuration of the potential, anode, and cathode wires guaranteed a homogeneous electric field and therefore a constant drift velocity for the electrons from gas ionisation as well as a constant Lorentz angle. The electrons near the signal wires were accelerated by the electric field and produced secondary electrons in further collsions with the gas molecules. This resulted in a measurable charge deposition on the signal wires, which were read out on both ends with flash analog-digital converters. The measured drift times determined the $r-\phi$ coordinates of the reading points of a track whereas the z coordinates were measured by comparing the charge collected on either end of the wires. Thus, an average point resolution of 135 μm in the $r-\phi$ plane and 6 cm in z direction was obtained [70]. The sum of the collected and readout charge on both ends of the wires was required to determine the specific energy loss $\mathrm{d}E/\mathrm{d}x$ in the chamber gas. For minimal ionising pions the relative uncertainty of this measurement was 3.8 % if 159 track points could be measured. The whole tracking system was embedded in a solenoid providing a 0.435 T magnetic field. This was sufficient to bend the tracks of high momentum charged particles measurably. The average transversal momentum resolution of this design was found to be [70]

$$\frac{\sigma_{p_t}}{p_t} = \sqrt{0.02^2 + \left(\frac{0.0015 \cdot p_t}{\mathrm{GeV}/c}\right)^2}, \tag{3.1}$$

where the constant term was due to multiple scattering in the chamber medium and the second term took into account the intrinsic resolution and uncertainties of the track reconstruction. The relative uncertainty of the transversal momentum therefore amounted to 2.5 % for a particle of p_t =10 GeV, while for μ pairs with a maximum transversal momentum of p_t =45 GeV a relative error of 6.8 % was obtained.

The precision of the z measurement and thus the precision of the measurement of the polar angle θ of a central track in the barrel region, i.e. $|\cos\theta_{track}| < 0.72$, was enhanced by the outermost subsystem of the central tracking device: the **z chamber**. It was subdivided into 24 drift chambers surrounding the jet chamber. These relatively flat chambers (5.9 cm thick) contained wires stretched perpendicular to the beam direction. Each z chamber consisted of 8 sectors with 6 signal wires each. The track points measurement also resulted from the measurement of the drift times of the produced electrons yielding a spatial resolution of this component of 300 μm in the z direction and about 1.5 cm in the $r\phi$-plane [65].

The Time-of-Flight Counter

The time-of-flight system consisted of 160 scintillation counters forming a barrel of radius 2.36 m which was positioned outside and coaxial to the aluminium coil. Each counter was 6.48 m long so that the barrel part of the time-of-flight system covered the angular region $|\cos\theta| < 0.82$. It measured the time-of-flight for particles from the interaction region, in $e^+e^- \rightarrow \mu^+\mu^-$ at LEP1 with an accuracy of 460 ps. Thus, it generated fast trigger signals and helped in the rejection of cosmic rays.

The time-of-flight counter in the endcap region consisting of scintillating tiles with fibre readout was not installed until the beginning of the LEP2 program. Therefore, it will not be described in this thesis. A description can be found in [71, 72].

The Calorimeter System

The central tracking system was surrounded by a nearly hermetic calorimeter system. It consisted of a presampler, an electromagnetic calorimeter and a hadronic calorimeter. As mentioned above, a full description of the presampler and especially of the electromagnetic calorimeter will follow in a separate section (3.3).

`The Hadron Calorimeter`

The hadron calorimeter was mounted around the electromagnetic calorimeter. It was the return yoke of the magnetic coil equipped with thin streamer tubes. Through the alternation of planes of these tubes and passive iron layers, in which hadronic showers evolve, it formed a so-called sampling calorimeter for hadronically interacting particles which spanned radii from 3.39 meters to 4.39 meters. Hence, it was largely made of iron providing 4 or more interaction lengths of absorber, and it measured the energy of particles which had passed the electromagnetic calorimeter. There was a certain probability of hadronic interactions being initiated in the 2.2 nuclear interaction lenghts of the material in front of the hadron calorimeter. As a result, the overall hadronic energy had to be determined by combining signals from the electromagnetic and hadronic calorimeters. The hadronic calorimeter covered a solid angle of 97% of 4 π being constructed in three different parts: the barrel and the endcap hadron calorimeters as well as the hadron poletip calorimeter. More details about these components can be found in [65, 73].

The Muon Detector

Beyond the hadronic calorimeter, only muons and neutrinos arrived having passed 7 radiation lenghts[4] of material.[5] They reached the outermost detector component of OPAL, the **muon detector**, which was composed of 4 layers of 110 planar drift chambers in the barrel region and 4 layers of streamer tubes in the endcap region (two on each side). Location and direction of incident muons could be measured by these devices. The spatial resolution in the barrel region was 1.5 mm in azimuthal and 2 mm in z direction. In the endcaps, a spatial resolution of 1 mm to 3 mm in the xy-plane was achieved.

---

[4] for pions

[5] This is not the full story. Sometimes hadrons were not completely absorbed in the hadron calorimeter and caused signals in the muon chambers. Therefore the information provided by hadron calorimeter was needed to guarantee a proper muon identification.

The Forward Detectors

The forward detectors were installed at both ends of the OPAL detector around, and close to the beam pipe. Their main purpose was a precise determination of the luminosity, by measuring the rate of low angle electron-positron pairs coming from Bhabba scattering ($e^+e^- \rightarrow e^+e^-$).[6] Two kinds of the forward detectors existed. The older one was a system of drift chambers, scintillators, tube chambers and a lead-scintillator calorimeter which was 24 radiation lengths thick. These components were mounted between 2 and 3 meters away from the interaction region. Further components belonging to this originally installed forward system were the far forward monitor counters, small lead-scintillator calorimeters positioned 7.85 m away from the interaction region on either side of the beam pipe. This design achieved a luminosity measurement with a systematic error of 0.45%. To improve the systematic error on the luminosity measurement up to the level of the expected statistical error, in 1993 two silicon-tungsten calorimeters encircling the LEP beam pipe on opposite sides of the OPAL detector were built in. These again were sampling calorimeters, that measured at very low angles (between $\theta = 25$ mrad and $\theta = 58$ mrad). The systematic error on the luminosity measurement was reduced to 0.034% by this component [74].

3.3 The Electromagnetic Calorimeter and the Presampler

As the electromagnetic calorimeter (ECAL) and the presampler play a vital role in identifying highly isolated photons for the present study both components will be discussed in more detail in this section.

3.3.1 The Electromagnetic Calorimeter of OPAL

Electromagnetic calorimeters are devices to measure the energy, the position and in some cases the flight direction of electromagnetically interacting particles like electrons, positrons and photons in the topology of a single high energy physics event.[7] The OPAL calorimeter was designed to fully absorb such particles if they have energies ranging from some tens of MeV to 100 GeV. Exploiting an optimal ratio of nuclear interaction and radiation length of the material and comparing the energy deposition of a particle passing the electromagnetic calorimeter with its measured momentum in the central detector allowed to seperate electrons from hadrons. Photons from π^0 decays and single photons could be distinguished by the signature they left in electromagnetic calorimeter.

`Design`
Consisting of a barrel and two endcap parts overlapping each other the ECAL covered 98%

---

[6] Bhabba scattering is the ideal process for such a measurement since its cross-section is dominated by the t-channel γ-exchange, which can be theoretically calculated in the framework of QED with a very high precision.

[7] Their flight direction can only be measured if one knows or is able to determine where the particles come from. This information can be provided by assisting detector components or the geometrical design of the calorimeter itself.

of the full solid angle. Altogether, it was made off 11704 lead-glass blocks. The magnetic coil and the pressure vessel of the central tracking chambers positioned inside the calorimeter caused about 2 radiation lengths of material in front of it, so that most electromagnetic showers were already initiated before the particle reached the ECAL. As a result, the point and energy resolution were declined, which could be partly compensated by so-called presamplers installed in front of the ECAL both in the endcap and the barrel region. They measured the position and sampled the energy of the preshowers, thus improving the π^0-single γ and hadron-electron discrimination and providing information to correct the energy deposited by the preshower in the electromagnetic calorimeter. The barrel of the electromagnetic calorimeter was a cylindrical array of 9440 lead-glass blocks situated at a radius of 2455 mm around the beam axis and covered a polar angle of $|\cos\theta| < 0.82$ (see figure 3.3).

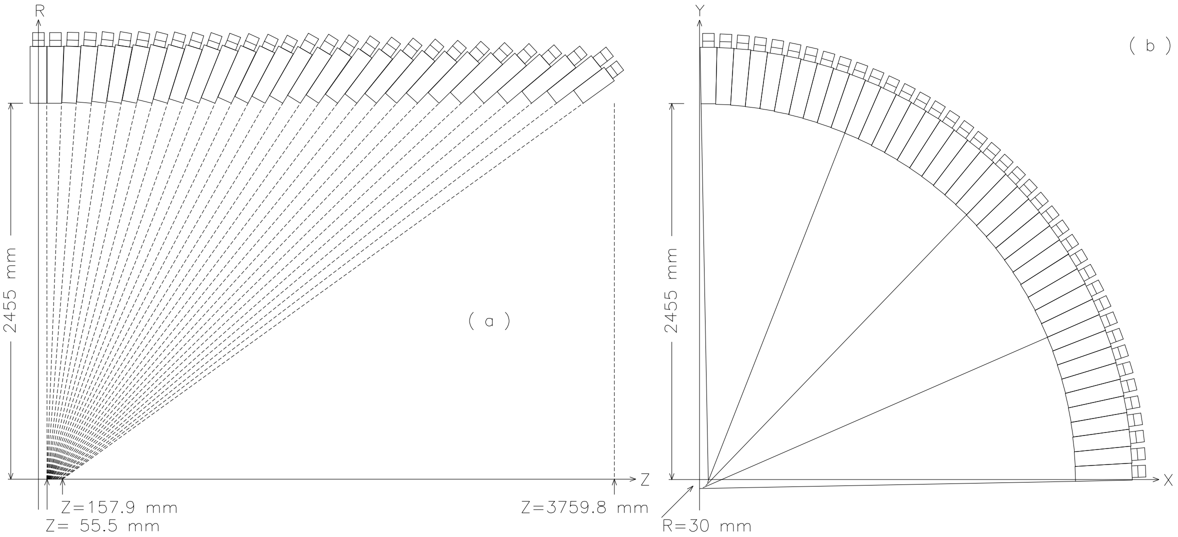

Figure 3.3: The $r - z$ (a) and $r - \phi$ (b) planes of the electromagnetic calorimeter barrel region.

Each lead-glass block had a volume of $10 \times 10 \times 37$ cm^3 with its front area translating into an angular coverage of 40×40 mrad^2 and its depth translating into 24.6 radiation lenghts of material. Its longitudinal axis nearly pointed to the interaction region, thereby minimising the probability of a particle which stemmed from an e^+e^- interaction to traverse more than one lead-glass block. This was the so-called 'pointing geometry' of which is taken advantage in the 'Cluster Shape Fit' being essential for the photon identification in this analysis and described later (see section 4). The blocks were not perfectly aligned to the nominal interaction point to prevent neutral particles from escaping through the gaps between the blocks (sketches in 3.3). The electromagnetic endcaps covered the full azimuthal angle and a polar angle of $0.81 < |\cos\theta| < 0.98$[8] consisting of 1132 lead-glass blocks, respectively. Unlike the barrel blocks, the endcap blocks were not pointing to the interaction region but they were aligned parallel to the beam line vertically covering an area of 9.2×9.2cm^2 each.[9] Particles that entered the endcap block assembly coming from the interaction region had to traverse at least

---

[8] resulting in an overlapping region for the barrel and endcap components on both sides of the detector between $|\cos\theta| = 0.81$ and 0.82.

[9] This was due to the geometrical constraints given by other detector components.

20.5 radiation lengths of material and typically 22.

`Material`

The ECAL blocks in the barrel were made of heavy lead-glass of type SF57. This glass consisted of 75% by weight PbO. In the endcaps the blocks were made of CEREN-25 consisting of 55% by weight PbO. Further specifications for both materials can be found in [65] and in chapter 4.

`Readout`

The lead-glass blocks were instrumented with magnetic field tolerant phototubes in the barrel or vacuum photo triodes in the endcap region. They read out the Čerenkov light which was caused by charged particles in an electromagnetic shower emerging in the calorimeter blocks. The readout was controlled by different optical monitoring systems in the barrel and the endcaps. Moreover, the calorimeter was readout for randomly triggered events, in which no e^+e^- collision occured. Blocks showing signals in these events were removed for the actual data analysis. The layout of one barrel lead-glass block with its readout device is shown in figure 3.4

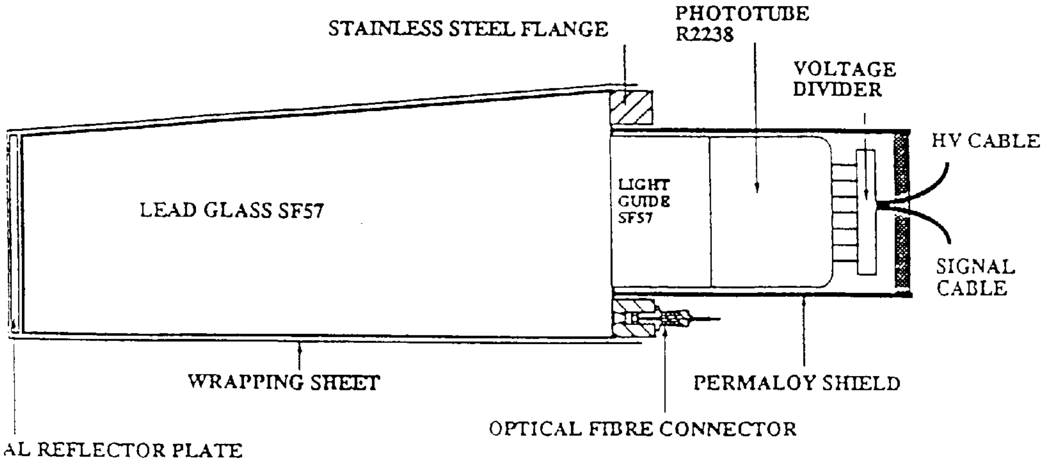

Figure 3.4: A lead-glass block as implemented in the electromagnetic calorimeter barrel of the OPAL detector. Each block was wrapped with a black sheet of vinyl fluoride for optical isolation and its inner surface was coated with aluminium for efficient reflection of light.

`Resolutions`

The intrinsic energy resolution of the electromagnetic calorimeter in the barrel region was [65]

$$\frac{\sigma_E}{E} \simeq 0.002 + \frac{0.063}{\sqrt{E/(1\mathrm{GeV})}}. \tag{3.2}$$

In the endcap region the resolution was found to be

$$\frac{\sigma_E}{E} \simeq \frac{0.05}{\sqrt{E/(1\mathrm{GeV})}}. \tag{3.3}$$

The intrinsic spatial resolution for electromagnetic showers in both the endcap and barrel part of the calorimeter was 11 mm. These resolutions were worsened by the material in front of the ECAL causing a variation of the energy resolution that depended on the polar angle of the measured particle. In the regions $0.72 < |\cos\theta| < 0.81$ and $0.92 < |\cos\theta| < 0.98$, 8 and 6 radiation lengths were seen by a traversing particle (compared to the 2 radiation lengths for particles in the barrel region moving vertically to the beam line). Energy correction algorithms are utilised in the analysis to take this into account. A picture of one half of the dismantled ECAL barrel of OPAL can be seen in figure 3.5.

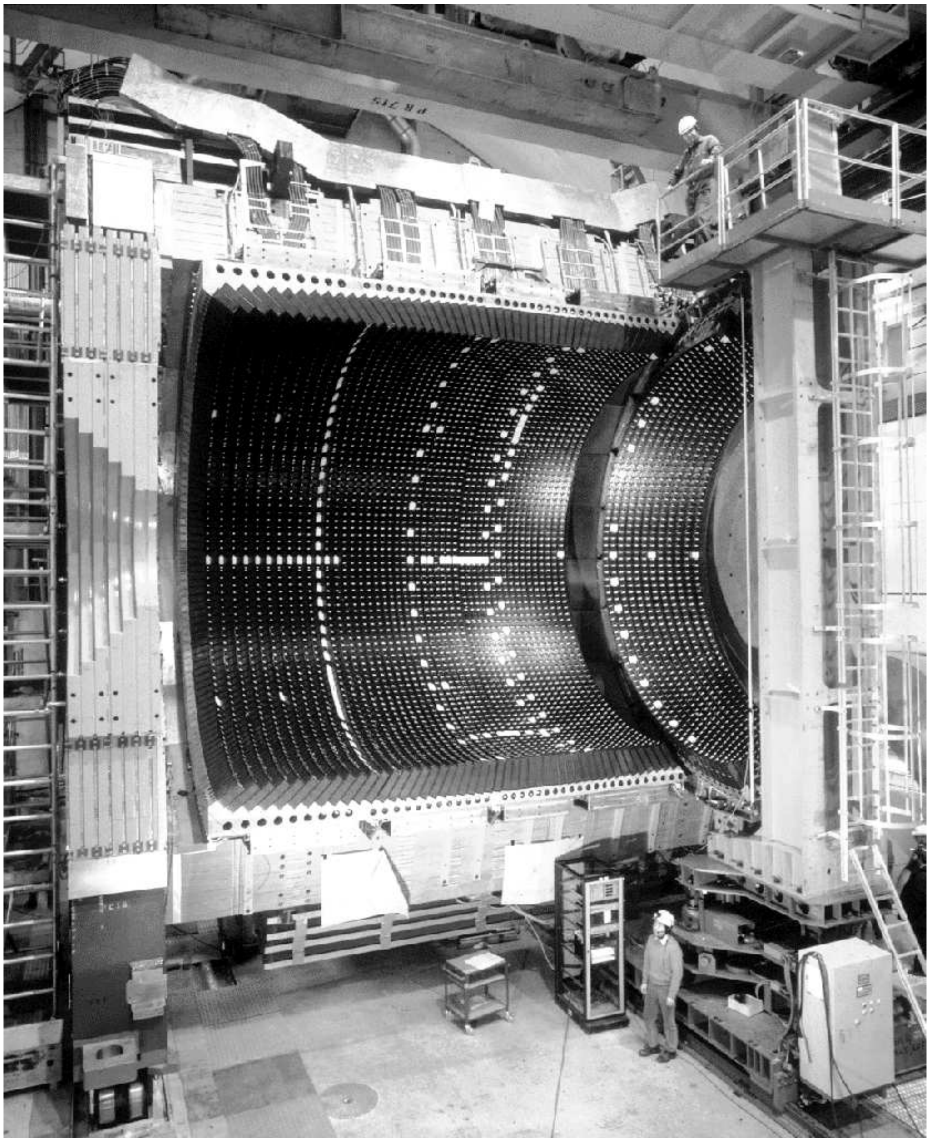

Figure 3.5: The Electromagnetic Calorimeter of OPAL

3.3.2 The Presampler for the Electromagnetic Calorimeter

The electromagnetic presampler in the barrel region consisted of 16 chambers located in a cylindrical fashion around the beam line between the time-of-flight counters and the electromagnetic calorimeter. The radius of this cylindrical construction was 2388 mm, its lengths was 6623 mm resulting in a polar angle coverage of $|\cos\theta| < 0.81$. Each presampler chamber was 3 cm thick and made of two layers of limited streamer mode tubes with the wires stretched axially. Each layer contained 24 cells. On either side of the layers were cathode strips, oriented at 45° to the wire direction and orthogonal on opposite sides. The charge generated on a wire was readout on both ends and the position along the wire was measured by charge division. By using the correlation between the charge collected on a wire and the signals measured by the cathode strips and applying a fit procedure hits were defined in each sector. The spatial resolution of the presampler varied between 4 and 6 mm in the plane perpendicular to the electromagnetic shower for a shower energy between 6 GeV and 50 GeV.

The endcap electromagnetic presampler was an umbrella shaped arrangement of 32 multiwire chambers located between the pressure bell of the central tracking system and the endcap calorimeter. They covered the full azimuthal angle and $0.83 < |\cos(\theta)| < 0.95$. The spatial resolution for an electromagnetic shower depended on its energy and varied between 2 and 4 mm.

3.4 The Simulations

In high energy physics experiments, it is common to use simulation packages, so-called Monte Carlo programs, to predict or check physics processes on a theoretical basis. These are both, the processes which are to be analysed as well as any process which might affect the investigated one. Roughly speaking two types of programs may be distinguished:

- programs generating processes on a pure high energy physics ('HEP') level where the four-momenta of all particles produced in a particle collision are simulated as predicted by theoretical models, and
- programs simulating the response of the detector to these 'HEP' momenta given that the corresponding particles live long enough to reach the detector components and to interact with their material.

Such a simulation package also exists for the OPAL detector and is called GOPAL [83], which is based on the widely used detector simulation package GEANT [84]. One purpose of the GEANT package is simulating large detector designs and thereby, evaluating their performance in the lead time of an experiment. Regarding data analysis, it is additionally used as a tool for understanding the recorded data and the data taking quality of an existing experiment.

The GOPAL package describes the components of the OPAL detector in terms of material, geometry, response and resolution as well as the magnetic field insight the detector. Four-momenta of particles generated with HEP-packages like JETSET/PYTHIA [50] and HERWIG [51] serve as input to GOPAL. These are widely used to describe processes in e^+e^- collisions, and in particular processes studied in the present analysis (see section 2.3.1). The particles generated by the HEP-packages are tracked through the geometry, simulating interactions with the particles of the detector material. As output GOPAL gives 'raw data', which is given in the same format as delivered by the real detector and which can be processed by the OPAL event reconstruction progam ROPE [85].

The information supplied by the event reconstruction is analysed for either data and simulated events in the same manner and the results in both cases can be compared. Thus, efficiencies of particle detection and resolutions of the various detector components and their interplay can be determined. Besides, distortions of results and systematic errors of the measurement can be found, investigated and possibly corrected for in the final outcome. In the present thesis, such studies are important for efficiency and background corrections to extract the true photon rate on parton level (which as pointed out in chapter 2 we want to measure) starting from the photon rate measurement on detector level. Further explanations in this regard will follow in section 5.2.

Chapter 4

Identifying Photons with the Electromagnetic Calorimeter of OPAL

In section 3.3, the electromagnetic calorimeter system of OPAL was introduced as the main tool for identifying photons, electrons and positrons. For this analysis it provides the necessary information to identify hadronic Z^0 decays with an isolated photon radiated off the quarks. The largest background contribution - apart from photons which stem from initial state radiation off the incoming leptons, and therefore, cannot be distinguished from the final state photons by the signature they leave in the calorimeter system - is due to neutral hadrons produced in the fragmentation of the partons. They either produce hadronic showers in the presampler and the electromagnetic calorimeter (ECAL) or they decay into photons which cause electromagnetic showers. These 'neutral hadron' showers have profiles of energy depositions in the lead glass blocks of the ECAL which are different from the shower profiles generated by single photons. As discussed in detail in chapter 5, overlapping double-photon showers in consequence of $\pi^0 \to \gamma\gamma$ decays are the largest hadronic background contribution and can be distinguished by their profile from single-photon showers, since, on average, they are broader than the latter.

In the present chapter, an algorithm to identify highly energetic single photons will be described. It makes use of the pointing geometry and the known material specifications in the barrel region of the ECAL. This so-called cluster shape fit presented in [86] is based on a program which was originally designed for the electromagnetic calorimeter of the JADE detector [14,87]. Some general remarks on electromagnetic showers in materials are made beforehand.

4.1 Showers in the Electromagnetic Calorimeter of OPAL

4.1.1 General Introduction

If a highly energetic photon or electron enters the material of a thick absorber material it generates an electromagnetic shower consisting of electrons, positrons and photons. Two processes contribute to the shower evolution: pair production and bremsstrahlung. High-energy photons traversing matter convert into e^+e^- pairs, which then emit bremsstrahlung. The

	$\rho(\mathrm{gcm}^{-3})$	$X_0(\mathrm{cm})$	$E_c(\mathrm{MeV})$
SF57	5.54	1.5108	13.0

Table 4.1: The material specifications of the electromagnetic calorimeter in the barrel region of the OPAL detector. The radiation length is given in cm compared to equation 4.1 where X_0 is scaled to the density of the material [65].

bremsstrahlung photons in turn convert into further e^+e^- pairs, and so on. The resulting particle cascade is called electromagnetic shower, and looks similar independently of whether it was initiated by a photon or an electron. The shower evolution stops as soon as the energy of the produced electrons and positrons falls below a certain value, the so-called critical energy E_c. The critical energy is sometimes defined as the value at which the electrons in the shower lose their energy by bremsstrahlung at a rate which is equal to the loss rate due to ionisation.[1] As a consequence, no further photons are produced, and particle multiplication in the shower is stopped. The critical energy E_c is material dependent and can be estimated with the empirical relation $E_c \simeq 800\mathrm{MeV}/(Z+1.2)$ with Z as the atomic number [10]. The shower development is usually expressed in terms of the radiation length X_0, defined as the mean distance over which an electron loses all but $1/e$ of its energy by bremsstrahlung. For most materials, it can approximately be expressed by

$$X_0 = \frac{716.4\mathrm{g\ cm}^{-2} A}{Z(Z+1)\ln(287/\sqrt{Z})}, \tag{4.1}$$

where Z is the atomic number and A is the atomic weight (in g mol^{-1}) of the medium [10]. The mean free path λ_{pair} which a high-energy photon travels through such a medium before it converts into an e^+e^- pair is related to the radiation length via

$$\lambda_{pair} \simeq \frac{9}{7} X_0. \tag{4.2}$$

The numbers for the lead glass calorimeter in the barrel region of OPAL are summarised in table 4.1.[2]

The evolution of an electromagnetic shower is a statistical process, which is conveniently expressed in terms of the number of radiation lengths over which the shower has evolved longitudinally:

$$t = x/X_0, \tag{4.3}$$

where x is the longitudinal distance of a shower point from the shower origin in cm and X_0 is the radiation length in cm. The total number of particles produced in the shower grows

---

[1] In [88] an alternative definition based on [89] is given: The critical energy E_c is reached if the energy loss per radiation length equals the energy of the particle: $E_c = (-dE/dt)_{E_c}$ with t as the longitudinal distance from the shower origin.

[2] In connection with electromagnetic shower descriptions, the Molière radius is often mentioned. It is defined by $R_M \simeq X_0 \cdot 21\mathrm{MeV}/E_c$ [10] where E_c is the critical energy as given in [89]. It is a measure of the lateral electromagnetic shower dimension but it will not be used in the shower parametrisation of the present fit.

exponentially as a function of t, and, at the end of t radiation lengths, it is given by

$$N(t) \simeq 2^t \tag{4.4}$$

assuming $\lambda_{pair} = X_0$. Each of these shower particles has an average energy of

$$E(t) \simeq \frac{E_0}{N(t)} \simeq \frac{E_0}{2^t} \tag{4.5}$$

with E_0 as energy of the incident photon or electron. As soon as $E(t)$ is equal to the critical energy E_c,

$$E(t_{max}) = \frac{E_0}{2^{t_{max}}} = E_c \tag{4.6}$$

the maximum penetration depth of the particle cascade,

$$t_{max} = \frac{\ln(E_0/E_c)}{\ln 2}, \tag{4.7}$$

is reached, at which the maximum number of particles is produced. Beyond this depth, the number of generated shower particles falls off exponentially.

The described model is very simple and only gives a qualitative picture of an electromagnetic shower neglecting energy losses due to ionisation when the shower is still progressing or energy dependencies of the cross-setions for bremsstrahlung and pair production. More precise calculations are possible by utilising Monte Carlo techniques.

4.1.2 Shower Parametrisation

The electromagnetic shower profile is well described by a three dimensional function $\Pi(E_0, r, t)$ which according to [88] can be split up into a longitudinal and lateral part:

$$\pi(E_0, t) \qquad \text{and} \qquad f(E_0, r), \tag{4.8}$$

where t is defined by 4.3, and r is the radial distance from the shower origin in radiation length.[3] $\pi(E_0, t)$ represents, on average, the total number of charged shower particles crossing a plane perpendicular to the trajectory of the initial photon or electron at distance t from the shower origin. $f(E_0, r)$ is the corresponding total number of charged shower particles crossing a cylindrical shell parallel to the trajectory of the initial particle around the shower origin at a radial distance r. The longitudinal profile is fitted reasonably well with the function

$$\pi(E_0, t) = A \cdot t^{\alpha} \cdot \exp(-\beta t), \tag{4.9}$$

---

[3] A more general expression for the lateral shower profile additionally depending on the longitudinal distance t is also given in [88]: $f(E_0, r, t)$. But the absence of longitudinal segmentation and the pointing geometry of the ECAL of OPAL results in a simplification of this general expression, so that in the present fit the lateral spread can be expressed by $f(E_0, r)$.

where A is a scaling factor, and α, β are parameters which are obtained by comparing the results of the profile function with the results of a simulation using GEANT [84].
The lateral profile of an electromagnetic shower in lead glass has been measured, for instance, in [90] and can be represented as a sum of two exponentials. A narrow exponential describes the core of the shower, which evolves at the beginning of the particle cascade where bremsstrahlung by the highly energetic shower electrons and positrons dominates. A broader exponential describes the halo of the shower, which develops at a later stage of the particle cascade where the influence of multiple coulomb scattering becomes more important. Thus, the lateral profile can be expressed by

$$f(E_0, r) = a \cdot \exp(-br) + c \cdot \exp(-dr) \tag{4.10}$$

where a, b, c, and d are material dependent parameters which, like α and β above, are again obtained through fitting the lateral profile function to the Monte Carlo yields of GEANT. Both, the longitudinal and the lateral profile function are normalised,

$$\int_0^\infty f(E_0, r)dr = 1 \qquad \text{and} \qquad \int_0^\infty \pi(E_0, t)dt = 1 \tag{4.11}$$

from which follows

$$\frac{a}{b} + \frac{c}{d} = 1 \qquad \text{and} \qquad A = \frac{\beta^{\alpha+1}}{\Gamma(\alpha+1)}. \tag{4.12}$$

The determination of the parameters α, β, a, b, c, and d is performed for photons and electrons of various incident energies as described in [86]. A cylinder of lead glass of type SF57 with a radius of 10 and a length (depth) of 40 radiation length is defined in a GEANT environment. To study the lateral shower profile, this cylinder is subdivided into tubes of 0.25 X_0 thickness. For each tube, the number of electrons and positrons, which is proportional to the Čerenkov light emission, are counted taking into consideration that the threshold energy for electrons emitting Čerenkov light in the lead glass material SF57 is 0.61 MeV, and that the number of generated Čerenkov photons depends on the velocity of the electrons. Other effects like the position and wavelength dependence of the light collection efficiency are neglected in this study. The optimised values for the lateral shower shape function parameters, a, b, c, and d are not found to depend significantly on the particle energy. However, they are corrected according to the angle of the incident particle, i.e. of the cluster in the ECAL. By this, the different amount of material which is seen by particles traversing the detector with different angles θ relative to the beam line is taken into account. In table 4.2, the parameters are listed for a photon and an electron coming from the interaction point and moving vertically with respect to the beam axis. Due to the angular dependent corrections the variables c and d are up to 11% (photons) and 20% (electrons) smaller than the numbers given in table 4.2, whereas the variations of a and b are in the range of 2 to 3%. This behaviour reflects that showers or clusters with a smaller angle θ relative to the beam line tend to be slightly broader, which can be seen for the photon case in figure 4.1. The corrections are larger for the shower core (determined by the parameters c and d) compared to its halo (determined by a and b), and they are larger for electrons compared to photons. Both trends are consistent with the expected effects of additional material in front of

Particle	a	b	c	d
γ	0.182	0.586	1.844	2.677
e^-	0.173	0.570	1.649	2.367

Table 4.2: The values of the fixed parameters in the lateral shower shape function 4.10 for photons and electrons moving perpendicularly to the beam axis.

the ECAL. Both electrons and photons may preshower in the coil, the time-of-flight detector or the presampler. The propability for initiating such a preshower causing in turn a broader cluster in the ECAL rises with the path length which is covered by both particle types in the coil or presampler medium. This path length is larger for smaller angles θ. Moreover, the mean free path λ_{pair} of a photon is approximately related to the radiation length of an electron by equation 4.2, so that the propability to cause a preshower for photons is smaller than for electrons. As a result, the parameters and their angular correction in the photon case is smaller than in the electron case.

In principle, to fix the parameter values of the longitudinal profile function the same procedure as above is applied defining a block made of SF57 in GEANT and subdividing it into slabs of equal thickness. However, the energy dependence of α and β is considerable and mathematical terms have to be specified which properly describe this dependence for shower energies up to 50 GeV. How these terms are determined will not be depicted in detail here (for further information see reference [86]), since in the present analysis only the two-dimensional option of the shower shape fit is used. Performing the three-dimensional shower shape fit is not expected to result in a significant improvement in the photon identification, since there is hardly any depth information available in the ECAL of OPAL. It has no longitudinal segmentation and the lead glass blocks in the barrel region are almost exactly pointing to the nominal interaction point (c.f. figure 3.3 and the corresponding description of the calorimeter system in chapter 3).

4.2 Photon Reconstruction with the Cluster Shape Fit

In the previous section, it has been described how a shower caused by a single photon or electron in the electromagnetic calorimeter of OPAL may be parametrised. Moreover, the method for fixing the free parameters a, b, c, and d in the lateral profile function has been outlined. This shower profile function 4.10 is used to predict the energy fraction deposited in each lead glass block belonging to an ECAL cluster of a particular, measured energy E_0. To be more precise, it is assumed that a measured ECAL cluster is caused by a single photon ('photon hypothesis'), and based on this the expected energies $E_{exp,i}$ in the lead glass blocks are calculated. These expected energies $E_{exp,i}$ are compared to the measured block energies $E_{meas,i}$. A χ^2 minimisation is performed varying the angle of incidence θ and ϕ of a hypothetical photon, thus trying to find the best agreement between expectation and measurement. For the best agreement which can be obtained a so-called cluster shape variable is defined as a measure of the photon likeness of a cluster.
In the following, the integration method which is used to calculate the expected block energies

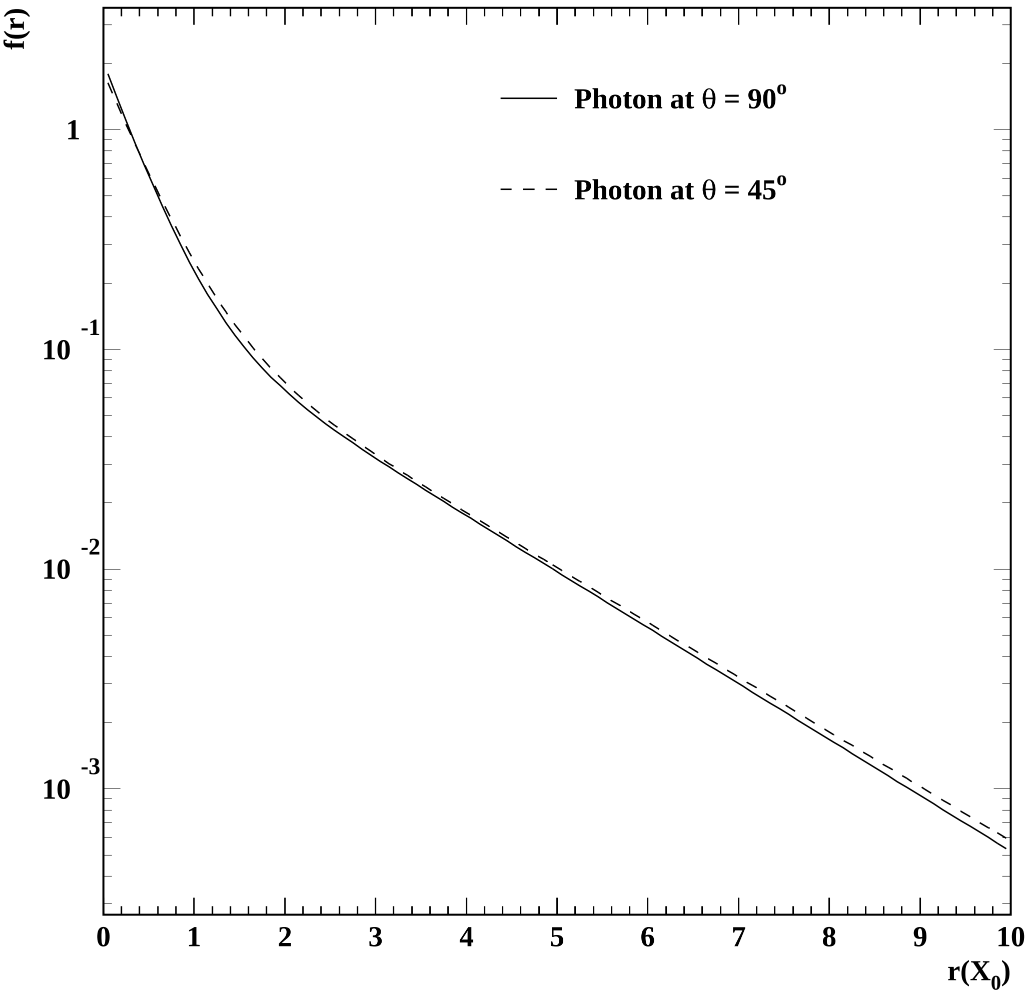

Figure 4.1: The lateral shower shape functions for a photon moving with an angle of $\theta = 45^o$ and perpendicularly to the beam line.

is described briefly. Subsequently, some remarks are made on the χ^2 minimisation and finally, the photon likeness or cluster shape variable C is defined.

4.2.1 The Calculation of the Expected Block Energies

To calculate the expected energy in each ECAL block affected by a photon shower the continuous shower profile described by expression 4.10 has to be translated into a discrete grid pattern of energy depositions in the lead glass blocks of a cluster. The method which is chosen for the integration of 4.10 is the so-called VEGAS algorithm [91]. The VEGAS algorithm, as an iterative and adaptive Monte Carlo scheme and as a widely used tool for multidimensional integration, shows all the characteristics which are needed to integrate the lateral shower function over the (x, y) cross-sections of each lead glass block in a defined cluster. The integrand does not have to be continuous which facilitates the integration over hypervolumes of irregular shape, and the convergence rate is independent of the dimensions of the integral. The most important feature of the VEGAS method is, indeed, that it is adaptive. It automatically concentrates the evaluations of the integrand in those regions where it is largest in magnitude. The expected energy deposition in block i contributing to a cluster is calculated as

$$E_{exp,i} = E_0 \cdot \int_S \frac{f(r)}{2\pi r} \frac{1}{X_0^2} dx dy, \tag{4.13}$$

where E_0 is the cluster energy, S is the cross-section of the lead glass block and r is transformed from the local coordinates (x, y) in the block. The factor $1/X_0^2$ is necessary as Jacobian. For the block in the cluster where the initial photon has impinged a special treatment is necessary. This block includes the pole of the integrand at $r = 0$. In order to avoid the pole, the integration in this block is performed over the (r, ϕ) space and the expected block energy is computed as

$$E_{exp,i} = E_0 \cdot \int_0^{2\pi} \int_0^{r_{max}} \frac{f(r)}{2\pi} dr d\phi. \tag{4.14}$$

The integrand of 4.14 is set to zero, if the local position (x, y) transformed from (r, ϕ) is beyond the limits of this lead glass block. In the above integration, 1.6 cm instead of 1.5108 cm (for SF57 only) is used as value for X_0 to compensate the effect of extra material in front of the ECAL (namely the coil, the time-of-flight detector, and the presampler barrel).

4.2.2 The χ^2 Minimisation

The energy spreading of a hypothetical photon shower over the lead glass blocks in the corresponding measured cluster is calculated with the VEGAS algorithm varying the angles θ and ϕ of the impinging photon. The measured cluster energy E_0, however, is fixed. By this, one obtains an expected energy deposition in each block belonging to the cluster, which depends on the fixed cluster energy and on the variable photon angles θ and ϕ: $E_{exp,i}(\theta, \phi)$. The best fit between photon expectation and measurement is obtained by minimising the value of

$$\chi^2(\theta, \phi) = \sum_{i=0}^{N_{blocks}} \frac{(E_{meas,i} - E_{exp,i}(\theta, \phi))^2}{\sigma_i^2}, \tag{4.15}$$

using the SIMPLEX method [92]. Here $E_{meas,i}$ is the measured energy deposition in the ith block of the cluster corresponding to the expectation

$$E_{exp,i}(\theta, \phi) = E_0 \cdot F_i(\theta, \phi), \tag{4.16}$$

where $F_i(\theta, \phi)$ is calculated with the integrals in 4.13 and 4.14 for various angles of incidence θ and ϕ of the photon. It represents the result of the shape function integration over one block unit, which is identical to the fraction of the cluster energy E_0 deposited in the ith block. The error σ_i comprises the intrinsic error of the energy measurement in the barrel region of the ECAL and the accuracy of the VEGAS integration:

$$\sigma_i^2 = \sigma_{meas,i}^2 + \sigma_{exp,i}^2, \tag{4.17}$$

where $\sigma_{meas,i}$ can be deduced from 3.2 as

$$\sigma_{meas,i} = 0.002 \cdot E_{meas,i} + 0.063 \cdot \sqrt{E_{meas,i}}, \tag{4.18}$$

and $\sigma_{exp,i}$ is given by

$$\sigma_{exp,i} = 0.05 \cdot E_{exp,i}. \tag{4.19}$$

0.05 is the chosen accuracy of the VEGAS integration in the present analysis.

4.2.3 The Cluster Shape Variable C

The cluster shape variable C, i.e. the measure for the photon likeness of an electromagnetic shower in the barrel region of the ECAL is now defined as the smallest χ^2 which is obtained after the minimisation of equation 4.15 divided by the total number of blocks belonging to the cluster:

$$C := \frac{1}{N_{blocks}} \cdot \min(\chi^2(\theta, \phi)). \tag{4.20}$$

C is plotted in figure 4.2 for neutral clusters which are selected in the barrel part of the electromagnetic calorimeter ($|\cos\theta_{cl}| < 0.72$) from a sample of multihadronic Z^0 decays simulated with JETSET. The discrimination power of C concerning single-photon clusters against clusters generated by neutral hadrons or their decay products is evident.

4.3 Comparison of the C distribution in Data and Monte Carlo

Because in the present analysis C is the most important variable to identify photons, and since the characteristic shape of its distribution will be utilised to estimate the amount of background in the selected candidates sample (see section 5.2.1.2), it is crucial to check whether the shapes of the C distributions agree well in data and Monte Carlo. In order to draw a fair comparison between simulated and real electromagnetic showers in the ECAL, one has to be able to rely on a very clean reference sample of single-photon clusters. Such a sample can be extracted from well defined $\mathrm{Z}^0 \rightarrow \mu^+\mu^-$ decays, which are preselected as described in [93, 94]. [4] The selection criteria in [93, 94] are tightened to get a sample which only consists of $\mathrm{Z}^0 \rightarrow \mu^+\mu^-\gamma$ events:

- Exactly two well measured tracks in the central detector are required, both associated with a cluster in the electromagnetic calorimeter.

---

[4] In detail the μ pair selection is described in two Technical OPAL Notes [95, 96].

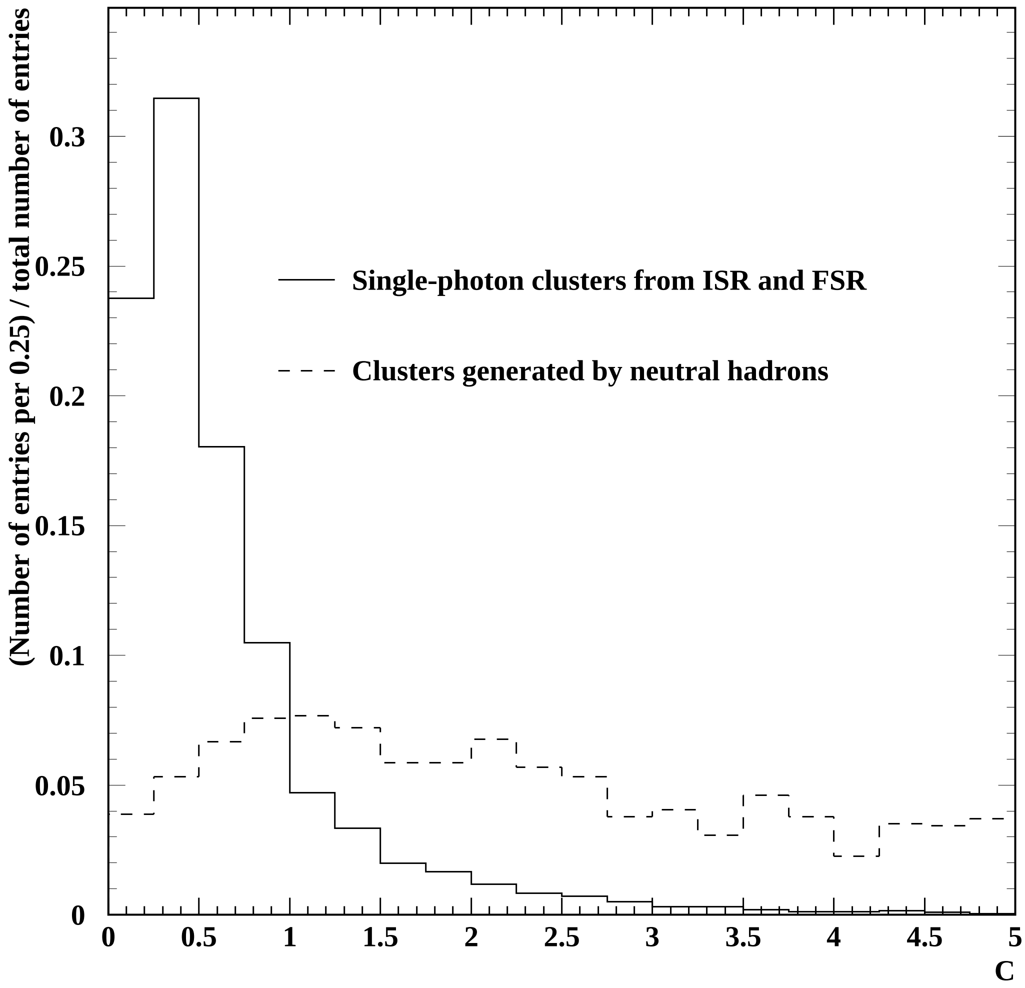

Figure 4.2: Distributions of C for neutral clusters in the ECAL with energies between 10 GeV and 15 GeV. Depicted is the distribution for single-photon clusters generated by initial and final state radiation as well as the distribution for clusters which are generated by neutral hadrons or their decay products. The neutral hadron sample mainly consists of π^0 and η decays and K_L^0 mesons. Each of the two histograms is normalised to its total number of entries.

- Exactly one additional cluster of at least 7 GeV energy which is not associated to any charged track is allowed in the ECAL. This cluster is most likely generated by an isolated photon from initial or final state radiation.
- The cluster must be situated in the barrel region of the ECAL ($|\cos\theta_{cl}| < 0.72$) and its angular distance to the closest track has to be larger than 10^o.
- The invariant mass of the isolated cluster with each track in the event must be greater than 2 GeV, which is larger than the τ mass.

Cluster Energy (GeV)	Efficiency, Data	Efficiency, MC
$7 \leq E_{cl} < 10$	0.986 ± 0.005	0.983 ± 0.003
$10 \leq E_{cl} < 15$	0.991 ± 0.004	0.986 ± 0.002
$15 \leq E_{cl} < 20$	0.990 ± 0.005	0.988 ± 0.003
$20 \leq E_{cl} < 25$	0.983 ± 0.008	0.983 ± 0.004
$25 \leq E_{cl} < 30$	0.987 ± 0.008	0.986 ± 0.004
$30 \leq E_{cl} < 35$	1	0.988 ± 0.004
$35 \leq E_{cl} < 40$	0.993 ± 0.007	0.992 ± 0.004
$40 \leq E_{cl} < 46$	1	0.994 ± 0.006

Table 4.3: The efficiencies for photonic clusters selected in radiative $Z^0 \to \mu^+\mu-$ decays if the cluster shape variable is required to be smaller than 5. The efficiencies are given separately for eight bins of measured cluster energies.

- The sum of the angles between the two tracks and between each track and the cluster is required to be larger than 359°.
- The visible energy of the event estimated from the track momenta and the photon energy fulfills the condition: $71 < E_{vis} < 111$ GeV.

The selection criteria in [93, 94] and the above listed selection criteria, which are inspired by [97] and by energy resolution studies for photon clusters in the ECAL [98], reject backgrounds due to multihadronic, $\tau^+\tau^-$, two-photon, and cosmic ray events. The remaining background from $\tau^+\tau^-$ events with clusters potentially produced by π^0 decay products is estimated using the Monte Carlo KORALZ [99] to be smaller than 0.1%.

2528 events collected at $\sqrt{s} \approx m_{Z^0}$ between 1990 and 1995 have met the selection criteria. The same cuts are applied to Z^0 decays into $\mu^+\mu^-$ which are generated with KORALZ [99]. Here, 9378 events are retained. The distributions of the cluster shape variable C in eight bins of the measured cluster energy are plotted in figure 4.3. The energy bins are chosen such, that the C distributions only depend weakly on the energy distribution of the photon clusters. Moreover, they are equal to those defined for the actual analysis (cf. section 5.2.1.2). As can be seen, a good agreement between data and Monte Carlo is achieved . In table 4.3 the photon efficiencies of the requirement $C < 5$ in the appropriate energy bins are listed. Again the agreement between data and Monte Carlo is good.

Clusters with an energy between 3 GeV and 7 GeV have also been studied. Their C distributions in data and Monte Carlo are shown in figure 4.4(a). In the first bin of the C distributions, which is the bin with the largest statistics, a significant discrepancy between data and Monte Carlo is visible. Several checks have been performed to identify the reason for this. These include the investigation of possible background sources in the sample (like single photons from π^0 decays in $\tau^+\tau^-$ events), and the search for general failures in the simulation of isolated photon clusters which might have an impact on the C distribution. In figure 4.4(b) and (c), two cluster variables are plotted for data and Monte Carlo: N_{blocks}, the number of blocks contributing to the cluster, and W, the energy weighted first moment of the angular

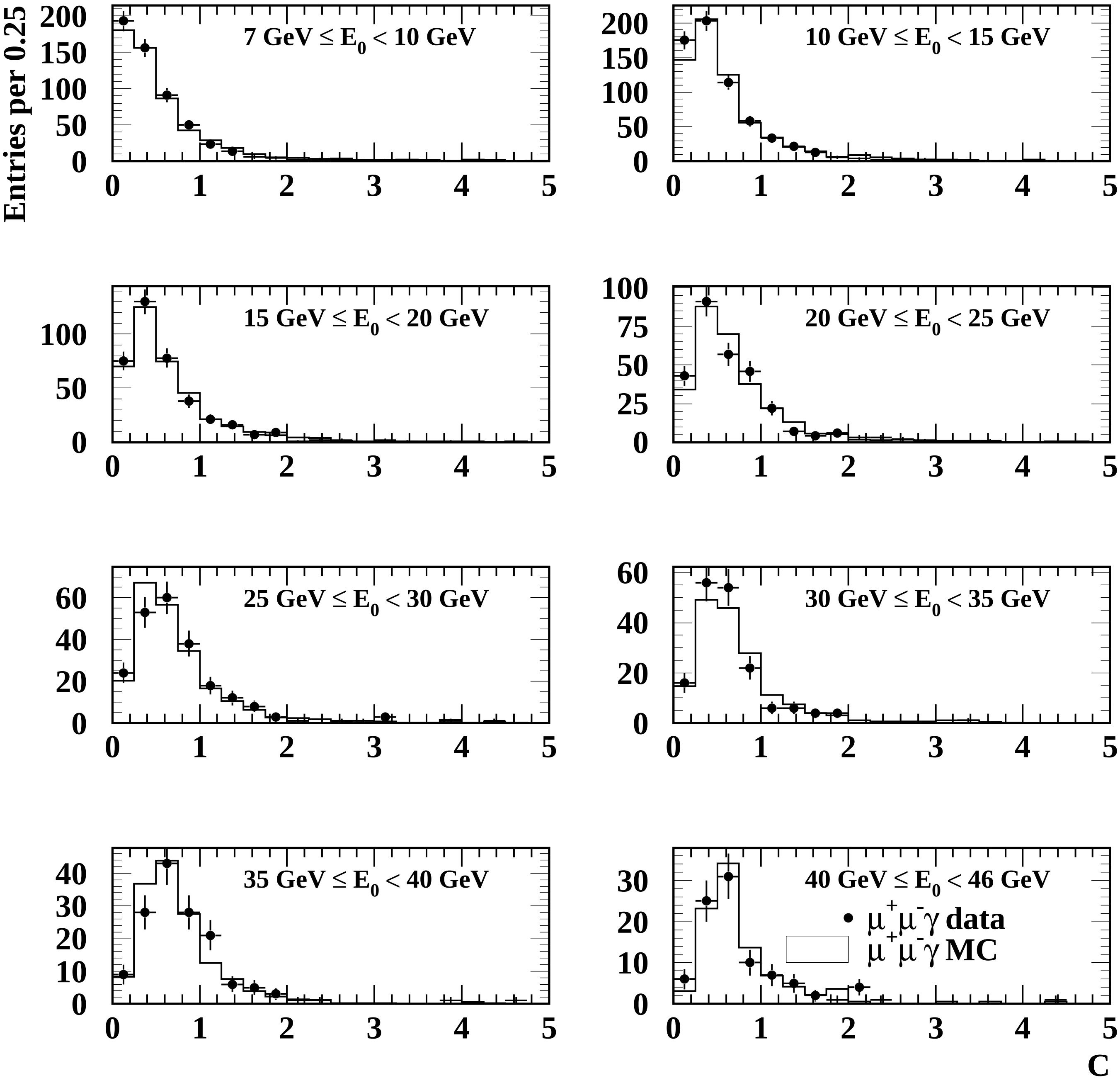

Figure 4.3: The distributions of the shape variable C for photon clusters in $\mu^+\mu^-$ events for data and Monte Carlo classified in eight bins according to their measured energy. The distributions are normalised to the data statistics.

block distribution in the cluster which is defined as

$$W = \sqrt{\frac{\sum_{i=1}^{N_{blocks}} E_{meas,i}((\phi_i - \overline{\phi_i})^2 + (\theta_i - \overline{\theta_i})^2)}{\sum_{i=1}^{n} E_{meas,i}}}, \tag{4.21}$$

where E_i, ϕ_i, and θ_i are the energy deposited in block i, its azimuthal, and its polar angle. The π^0 background has been found to be negligible, the variables N_{blocks}, W, and other investigated variables have not revealed a non-ambiguous correlation to the C discrepancy (although the distributions of W show small deviations for data and simulation). A satisfactory explanation for the deviation of C in data and Monte Carlo has not been found. To be safe from biases, clusters with energies below 7 GeV are therefore excluded from the analysis. They would not contribute significantly anyway. This is due to the fact that the photon rates as explained in chapter 2 are measured y_{cut}-dependently, and the y-cut also narrows the phase space for the photon candidates in terms of their energy.

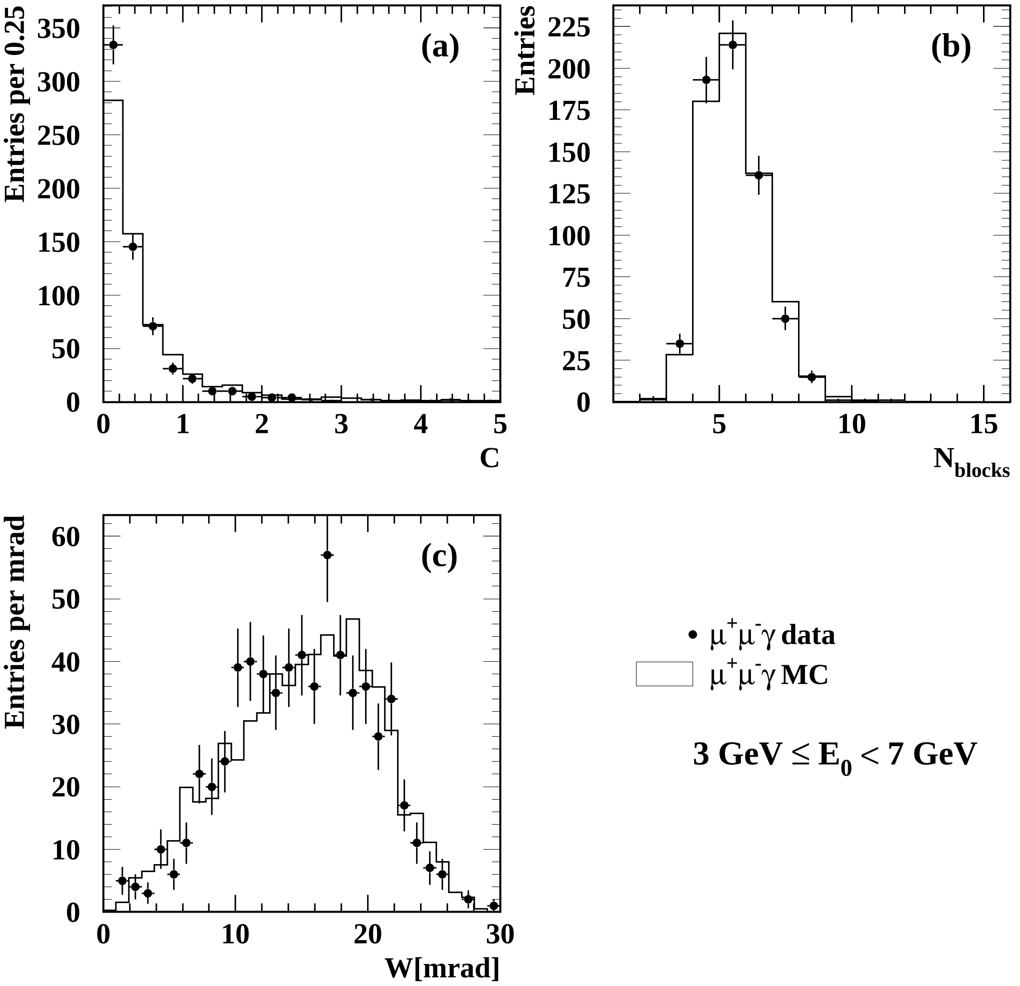

Figure 4.4: The distributions of the shape variable C, the number of blocks, and the first moment W, defined by equation 4.21, for photon clusters with energies below 7 GeV in $\mu^+\mu^-$ events in data and Monte Carlo. The distributions are normalised to the data statistics.

From the studies carried out, it can be concluded that the shape of photonic clusters in the barrel region of the electromagnetic calorimeter of OPAL is understood well and simulated correctly by the detector Monte Carlo for cluster energies larger than 7 GeV. Especially, the cluster shape variable C, as most important parameter of the photon identification, and its simulated distribution can be used to reject and estimate the backgrounds in the selected candidates sample of isolated clusters. How the candidate selection and background estimation works is described in the following chapter.

A summary of further tests using other algorithms for the photon identification in the electromagnetic calorimeter of OPAL may be found in the appendix.

Chapter 5

The Analysis

The analysis consists of three parts: the first part deals with the extraction of the candidates sample out of the whole data measured by the detector; the second part contains the identification and estimation of possible background sources in this sample as well as the estimation of efficiencies of the measurement; finally, the third part treats the identification, estimation, and calculation of measurement errors. These three steps are described in more detail in the following sections. The chapter is completed by the calculation and discussion of the couplings which are determined by the photon rate measurement.

5.1 Event Selection

As described in chapter 2 the aim of the analysis is to determine the rate of final state photons out of bremsstrahlung off quarks relative to the total number of multihadronic Z^0 decays. So firstly, such decays have to be defined.

5.1.1 Selection of Multihadronic Z^0 Decays

Standard selection criteria of multihadronic Z^0 decays are specified for the OPAL detector [100] using multihadronic Z^0 events simulated with the JETSET Monte Carlo, which is tuned according to studies of global event shape variables [93,101] and fed into the OPAL detector simulation GOPAL [83] (c.f. section 3.4). The resulting hadronic event selection in general exploits information delivered by the central detector and the electromagnetic calorimeter, namely track and cluster multiplicities as well as information on the energy flow in the electromagnetic calorimeter. First of all, 'good' tracks and 'good' electromagnetic clusters have to be defined. Good tracks are selected with at least 20 measured space points in the tracking system, a distance of closest approach from the nominal interaction point of less then 2 cm in (r, ϕ) and of less than 40 cm along the z (beam) axis. Moreover, a minimum momentum of the track in the direction transverse to the beam axis of 0.05 GeV is required. By these requirements it is ensured that only well measured tracks originating from the true interaction point are selected. The cut on the minimum transverse momentum rejects tracks of low energetic charged particles that curl inside the tracking system because of its magnetic field. Good clusters in the barrel region of the electromagnetic calorimeter are required to have an energy of at least 0.1 GeV. In the electromagnetic endcap region, only clusters with an energy of more than 0.2 GeV shared by at least two adjacent blocks are accepted as good. The purpose of these selection cuts is mainly to reject electronic noise in the calorimeter.

An event measured by the OPAL detector is classified as a multihadronic Z^0 decay if it fulfills the following requirements based on the above defined good tracks and clusters:

- There must be at least five good tracks and seven good clusters in the electromagnetic calorimeter. By this, events with relatively high particle multiplicities are selected and Z^0 decays into two charged leptons are rejected. Besides, events triggered by cosmic rays are removed from the sample since all good tracks are defined such that they originate from the true interaction point.
- The sum of the energies of all good clusters in the electromagnetic calorimeter is required to amount to at least 10 % of the centre-of-mass energy:
  $$\sum E_{cluster}/\sqrt{s} \geq 0.1. \tag{5.1}$$
  This requirement serves the purpose of rejecting two-photon events, where a large fraction of the centre-of-mass energy is carried away by the outgoing electron and positron which move with a very small angle along the beam direction, and which are therefore invisible for the detector. In addition, fake events caused by interaction of beam particles with gas molecules remaining within the beam-pipe and other machine-related backgrounds are discarded.
- The imbalance of the energy flow in the lead glass calorimeter with respect to the beam axis should not be too large. This is ensured by
  $$\frac{\sum(E_{cluster} \cdot \cos\theta_{cluster})}{\sum E_{cluster}} < 0.65 \tag{5.2}$$
  where $E_{cluster}$ and $\theta_{cluster}$ are the energy and polar angle of one good cluster. The sums in the numerator and the denominator take into account all clusters accepted as good in the electromagnetic calorimeter. The above cut rejects events generated in beam-related background interactions, among them collisions with gas molecules (see preceding item), interactions of beam-particles with the material of the beam-pipe, or so-called beam-halo events where muons are produced in beam-related reactions outside the detector.

The overall efficiency of this hadronic event selection is determined to be 98.6 % ± 0.4 % [100]. In addition to these global event shape requirements, demands on the detector performance are made. At least, the central jet chamber and the electromagnetic calorimeter have to be fully functioning.

The present analysis is based on data which were collected by the OPAL detector during the years 1990 to 1995 at a centre-of-mass energy approximately equal to the Z^0 mass. From the full data sample 3022897 multihadronic Z^0 decay candidates are selected by the given criteria.[1]

---

[1] So-called off-peak data taken at centre-of-mass energies around the Z^0 mass between $\sqrt{s} \approx m_{Z^0} - 2$ GeV and $\sqrt{s} \approx m_{Z^0} + 2$ GeV are not analysed.

5.1.2 Selection of Isolated Photon Clusters

Within the selected sample of hadronic Z^0 events electromagnetic clusters generated by photons radiated off the final state quarks are searched for. As discussed in detail in section 2.1.1 only isolated photon candidates are considered. In this section, it will be described how photon clusters are identified and how their isolation from the hadronic rest of the event is defined.

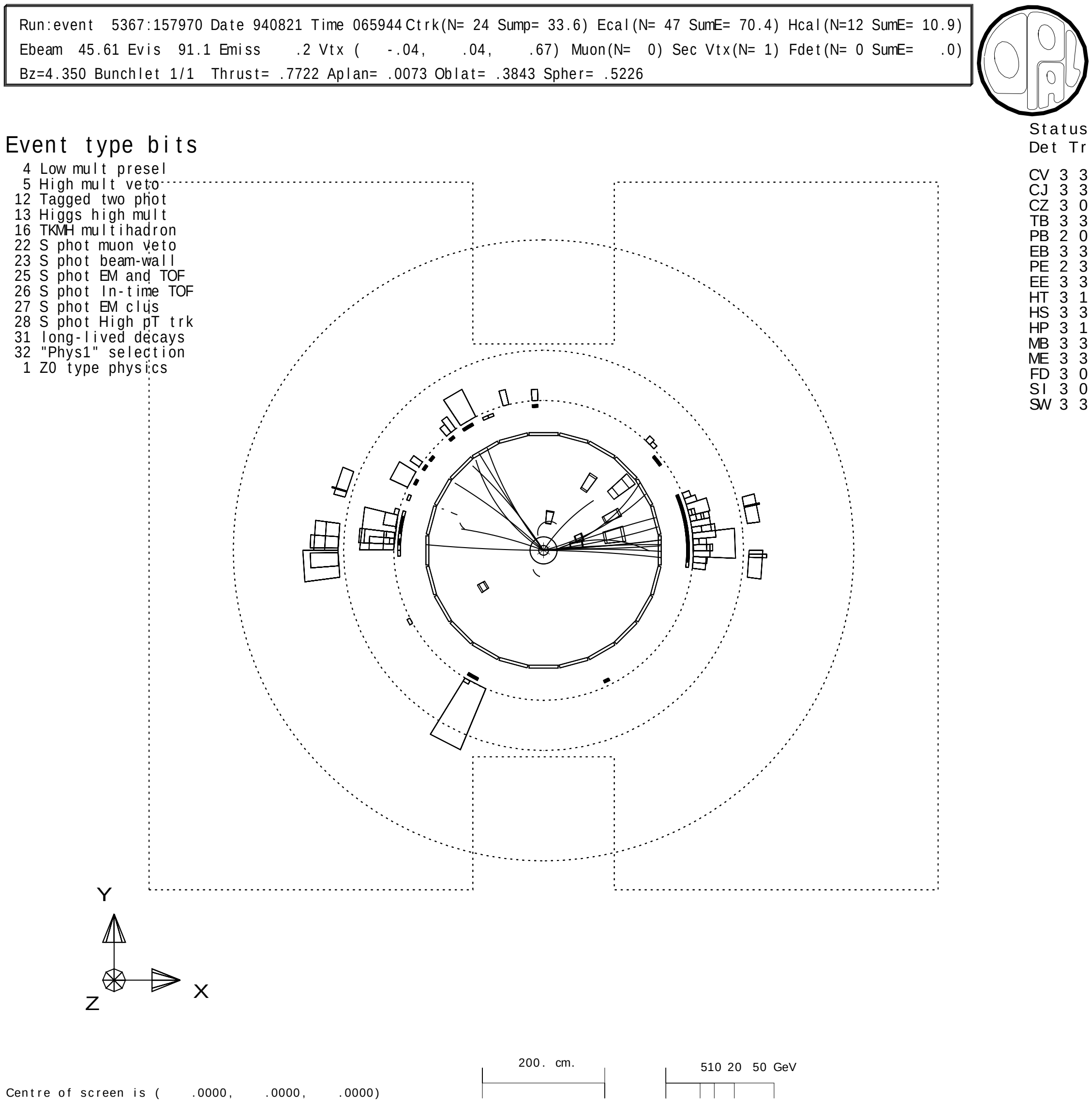

```
Run:event  5367:157970 Date 940821 Time 065944 Ctrk(N= 24 Sump= 33.6) Ecal(N= 47 SumE= 70.4) Hcal(N=12 SumE= 10.9)
Ebeam  45.61 Evis  91.1 Emiss    .2 Vtx (   -.04,    .04,    .67) Muon(N=  0) Sec Vtx(N= 1) Fdet(N= 0 SumE=   .0)
Bz=4.350 Bunchlet 1/1  Thrust= .7722 Aplan= .0073 Oblat= .3843 Spher= .5226
```

```
Event type bits
  4 Low mult presel
  5 High mult veto
 12 Tagged two phot
 13 Higgs high mult
 16 TKMH multihadron
 22 S phot muon veto
 23 S phot beam-wall
 25 S phot EM and TOF
 26 S phot In-time TOF
 27 S phot EM clus
 28 S phot High pT trk
 31 long-lived decays
 32 "Phys1" selection
  1 Z0 type physics
```

```
Status
Det Tr

CV 3 3
CJ 3 3
CZ 3 0
TB 3 3
PB 2 0
EB 3 3
PE 2 3
EE 3 3
HT 3 1
HS 3 3
HP 3 1
MB 3 3
ME 3 3
FD 3 0
SI 3 0
SW 3 3
```

```
Centre of screen is (     .0000,      .0000,      .0000)
```

Figure 5.1: A candidate for a hadronic Z^0 decay with a final state photon: $Z^0 \rightarrow q\bar{q}\gamma$. Two jets are clearly distinguishable in the detector. The jets are not aligned back-to-back due to the recoil of the radiated photon which generates a highly isolated cluster visible in the electromagnetic calorimeter. The measured photon energy is 18.6 GeV.

In figure 5.1 a candidate for a Z^0 decay with an isolated photon produced in bremsstrahlung off the final state quarks is depicted. Candidates for events with isolated photons have to meet the selection criteria, which first of all are outlined briefly and subsequently are described in more detail:

- Only neutral clusters are considered.
- The candidate cluster is found in the non-overlapping region of the electromagnetic calorimeter barrel. Its polar angle $\theta_{cluster}$ has to fulfill the condition $|\cos\theta_{cluster}| \leq 0.72$.
- The corrected energy of the cluster is larger than 7 GeV.
- The cluster is shaped as expected for a single photon. This affects the number of lead glass blocks which contribute to the cluster, as well as the energy weighted first moment of the cluster W, and the cluster shape variable C.
- The cluster is isolated and has survived two isolation requirements:
  The first requirement demands that there is no cluster or track with an energy of more than 0.25 GeV within a cone of half opening angle 0.255 rad (14.61°) around the candidate cluster.
  The second requirement ensures that the cluster is well separated from each jet in the event. The reason for the second isolation criterion is discussed in the theory chapter section 2.1, some general remarks on jet finder schemes and their usage in the present analysis can be found in 2.3.4.

The selection criteria are designed such that they reject clusters generated by two classes of background sources. The first class includes all backgrounds due to neutral hadrons, which may directly produce a highly energetic cluster in the electromagnetic calorimeter, or which decay into photons which then produce a highly energetic cluster. Such clusters tend to be wider than clusters generated by single photons. The second background source is initial state radiation off the incoming leptons which also produces highly energetic single photon clusters but is expected to show an energy and angular spectrum which is different from that of photons radiated off the outgoing quarks.

For the first requirement in the above list of selection cuts, neutral or unassociated ECAL clusters have to be defined beforehand. This is done in the framework of an algorithm called MT ('Matching Tracks'). It is described briefly in [102] and detailed in [103,104]. The principle idea is given here. Charged particles may produce signals in both the central tracking system and the calorimeter system, resulting in a potential double counting of contributions to the total visible energy in the detector. The MT algorithm aims for the definition of four-momenta, which are corrected for this effect. In the end, only four-momenta of tracks and of clusters which are not associated with any track are retained. In this context, on the one hand an ECAL cluster is called neutral if no track extrapolation points to it. On the other hand, an ECAL cluster associated with a track may also be called neutral after the expected calorimeter energy for the corresponding track momentum is subtracted from the cluster energy. However, neutral clusters belonging to this second category are usually rejected by the first isolation criterion.

The second requirement of the above list affecting the polar angle of a cluster in the lead glass calorimeter is explained by the fact that the identification of photons in the barrel region for polar angles with $|\cos\theta| > 0.72$ and in the endcap region of the calorimeter is more difficult than in the barrel region for polar angles with $|\cos\theta| \leq 0.72$. This is a consequence of the amount of material in front of the calorimeter[2], which significantly degrades its spatial and energy resolution and introduces additional difficulties in the evaluation of the systematic errors of the photon rate measurement. Moreover, the cluster shape fit algorithm, which was described in chapter 4, and which is the most powerful tool to estimate the hadronic background contribution can only be applied in the barrel region because it makes use of the pointing geometry of the lead glass blocks. Moreover, it yields the most reliable results within an angular acceptance for clusters of $0.72 \leq |\cos\theta|$, which is also due to the larger amount of material in front of the calorimeter for polar angles θ with $0.72 < |\cos\theta| < 0.82$. Finally, the statistics which would be gained by taking into account the endcap region between $0.82 < |\cos\theta| < 0.92$ (at the same time collecting more background due to initial state radiation, see figure 5.2) has been estimated not to result in a significant improvement of the error on the measured photon rate.

The distributions of $\cos\theta$ for the candidate samples selected in data and Monte Carlo is plotted in figure 5.3. A good agreement is observed.

The third requirement, that the corrected cluster energy has to be larger than 7 GeV is introduced for two reasons. One reason is given by the expected energy spectra of the different sources which might generate electromagnetic clusters. Going to lower cluster energies the background contribution by photons from decaying neutral hadrons and from initial state radiation is rising faster than the signal contribution by final state radiation. This can be seen in figure 5.4, where the energy distributions of photons from initial state radiation and final state radiation are compared. The other reason is, that the agreement between data and Monte Carlo for the cluster shape variable C is not good enough at cluster energies below 7 GeV, as discussed in section 4.3.
The corrected cluster energy, which is used in the analysis, is deduced from the raw cluster energy E_0 which is the sum of the energies deposited in each lead glass block belonging to the cluster as follows. Firstly, the raw cluster energy is corrected applying a θ-dependent algorithm which is derived by Monte Carlo studies with the OPAL detector simulation GOPAL. Then this energy is additionally corrected according to the equation [98]

$$E_{cl} = E_{corr} - 0.400\mathrm{GeV} + 0.02 \cdot M_{PB}, \tag{5.3}$$

using signals from the electromagnetic presampler chambers (see section 3.3). M_{PB} is the measured multiplicity in the presampler barrel region which is assigned to the cluster in the electromagnetic calorimeter and E_{corr} is the angular corrected cluster energy. The total resolution of the corrected energy is found to be [98]

$$\frac{\sigma(E_{cl})}{E_{cl}} = \frac{0.129 \pm 0.010}{\sqrt{E_{cl}/(1\mathrm{GeV})}} \oplus (0.022 \pm 0.003) \tag{5.4}$$

for cluster energies larger than 5 GeV. The resolution is determined using radiative lepton pair events (c.f. section 4.3) and employing massless particle kinematics to obtain a reference value of the photon energy.

---

[2] c.f. section 3.3: eight and six radiation lengths for $0.72 < |\cos\theta| < 0.81$ and $0.92 < |\cos\theta| < 0.98$ compared to two in the 'good' part of the barrel region.

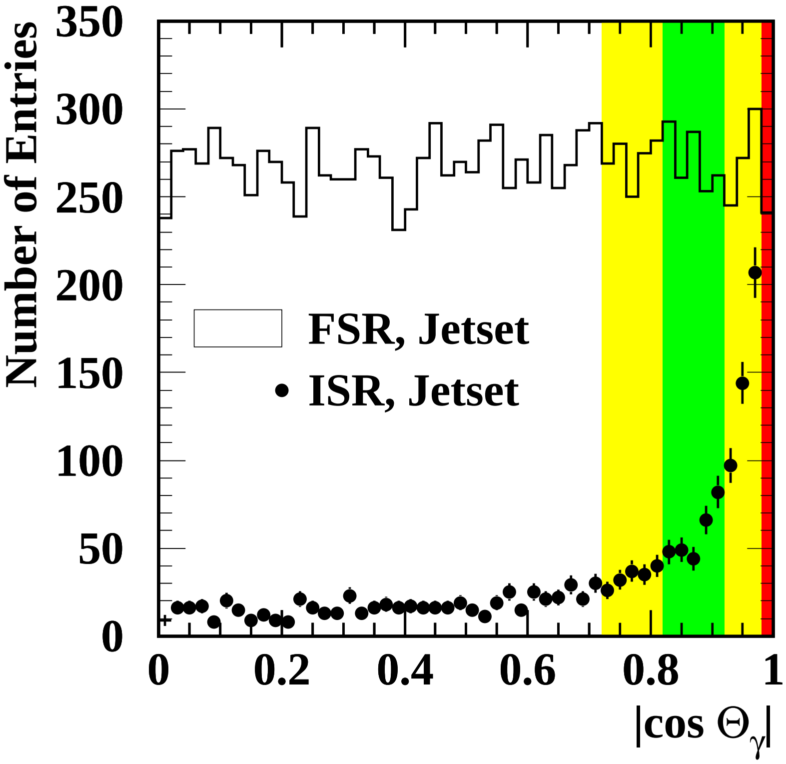

Figure 5.2: The distribution of the absolute value of $\cos\theta$ for prompt photons generated by initial and final state radiation in the Monte Carlo generator JETSET. The contributing photons have an energy of at least 5 GeV and have passed a y_{cut} for the jet-photon separation (here, $y_{cut} = 0.06$ in the Jade scheme). The contribution from initial state radiation rises exponentially for $\cos\theta_\gamma$ approaching one. By comparison, the run of the curve for photons from final state radiation is flat. Both behaviours are a consequence of the fact that the cross-section for bremsstrahlung rises exponentially for low angles with respect to the radiating particle, which is the incoming $e^{-(+)}$ for the initial state and the outgoing (anti) quark for the final state radiation. The differently shaded areas denote the different regions in the lead glass calorimeter which are discussed in the text.

The fourth requirement concerns the shape of an electromagnetic cluster. A Cluster is accepted if it consists of less than 16 lead glass blocks, each block with an energy deposition of more than 0.02 GeV. Moreover, for each candidate cluster, it is required that the energy weighted angular width W defined by equation 4.21 is smaller than 30 mrad. The third attribute in the photon likeness of a cluster candidate is the shape variable C. C is required to be smaller than 5 for each cluster candidate. The requirements on the shape variables are illustrated by three histograms in figure 5.5, showing the simulated background (neutral hadrons) and signal (ISR+FSR) distributions of N_{blocks}, W, and C for isolated clusters in the barrel region of the ECAL ($|\cos\theta_{cluster}| \leq 0.72$) with a corrected energy of more than 7 GeV. The W distribution is plotted for clusters fulfilling the requirement $N_{blocks} < 16$, the C distribution is plotted for clusters with $N_{blocks} < 16$ and $W < 30$ mrad, indicating that C has the greatest discrimination power for background clusters produced by neutral hadrons. In figure 5.6 the N_{blocks} and W distributions for the reference sample of photon clusters selected from measured and simulated μ-pair events as described in section 4.3 are shown. The corresponding C distributions have

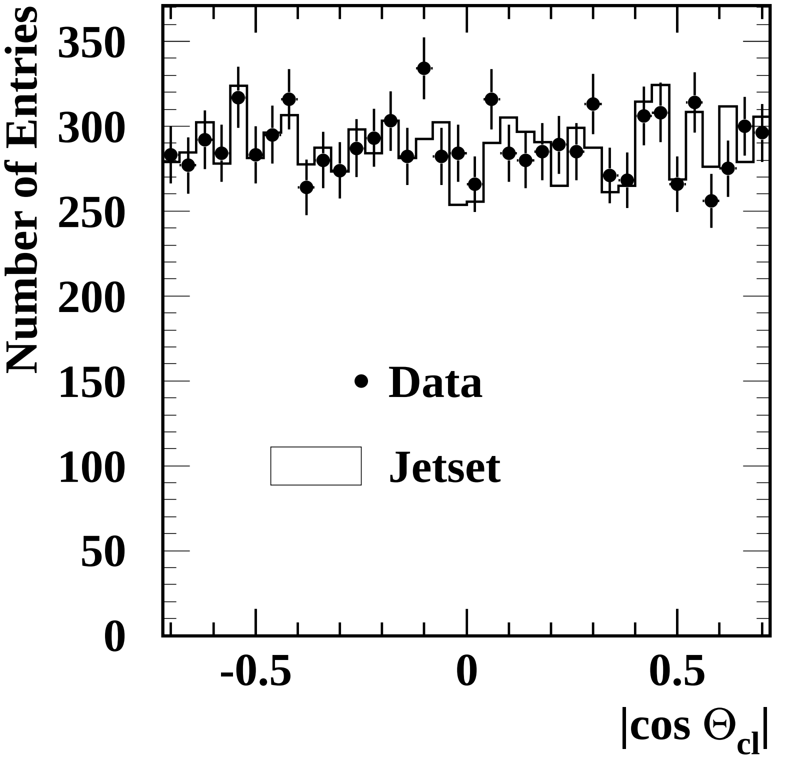

Figure 5.3: The distribution of $\cos\theta$ in data and JETSET for the selected photon candidates. The histograms are normalised to the data statistics.

been displayed in figure 4.3. The agreement between data and Monte Carlo is good in the case of W and C, whereas the simulated distribution of N_{blocks} is shifted to larger values compared to the measured one. The reason for this could not be identified, but the efficiency of the requirement $N_{blocks} < 16$ has been checked in the $\mu^+\mu^-\gamma$ reference sample and in both, data and Monte Carlo amounts to 100% for photon clusters. Thus, it is not expected that the cut on the number of blocks introduces a bias in the candidate selection.

The last item of the requirement list contains two isolation criteria. The first one is motivated by the needs of background reduction, the second by the needs of the theoretical final state photon rate calculation.

The first isolation criterion requiring an isolation cone around the candidate cluster with little energy deposition rejects background mainly due to the neutral hadrons which are produced in the fragmentation of the partons. In this analysis, cone isolation means that the scalar sum of additional track and cluster energy in a cone of half angle $\alpha_{cone} = 0.255$ rad is less than 0.25 GeV. In figure 5.7 two plots are displayed illustrating the cone isolation. The left plot shows the energy inside a cone of $\alpha_{cone} = 0.255$ rad for data and Monte Carlo, the right plot shows the number of events with an energy of less than 0.25 GeV inside cones of various half opening angles. The bins which are of interest in the present study are denoted with an arrow. As can be seen in the left plot of figure 5.7, raising the energy cut in the case of $\alpha_{cone} = 0.255$ rad would not result in a significant gain of efficiency. This plot looks similar for different opening angles. The right plot of figure 5.7 shows that there is a range of cone angles α_{cone} which are possible to choose. Indeed, one of the important systematic checks deals with

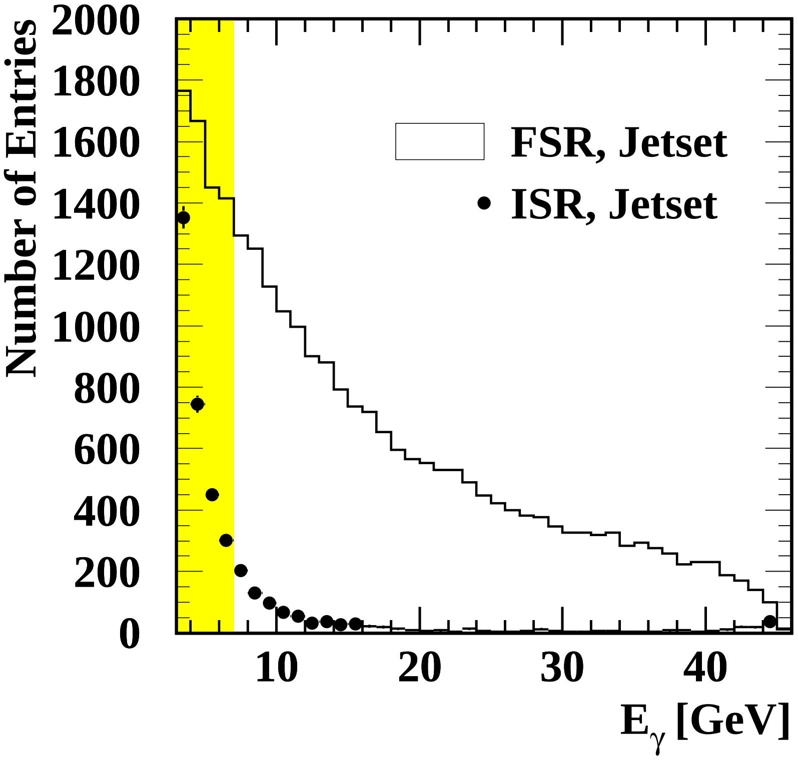

Figure 5.4: The energy distribution of prompt photons generated by initial and final state radiation in the Monte Carlo generator JETSET. The polar angle of the contributing photons fulfill the requirement $|\cos\theta_{cluster}| \leq 0.72$ and have passed a y_{cut} for the jet-photon separation (here, $y_{cut} = 0.06$ in the Jade scheme). The shaded area denotes the region of photon energies which are excluded from the analysis.

varying the isolation cut (see section 5.4.2.2). The agreement between data and Monte Carlo is not as good as in the case of the shape of photon clusters. This might be due to the fact, that the signal-to-background ratio in the selected sample is simulated incorrectly by JETSET. In any case, the energy flow around the photon candidate is subject of extensive systematic studies.

The second isolation criterion ensures that the underlying premises of the matrix element calculations, which are used to extract the coupling constants from the measurement, are still valid. As discussed in section 2.1.2, the perturbative calculations, based on first principles of QED and QCD only yields reliable predictions for the photon rate in a restricted region of the phase space. The restriction is implemented by imposing y parameters which are defined as in equation 2.11. In order to be able to compare measured and theoretically predicted FSR event shapes and rates, in addition jet recombination schemes are used to put the measured hadronic decays in a structure which is comparable to the theoretical prediction only existing on the level of partons. Two jet finder schemes are used according to those applied to the matrix element based Monte Carlo: the Jade E0 and the Durham scheme, which are both explained in section 2.3.4. As denoted there, the isolated photon selection follows a two-stage procedure. At the first stage, the jet finder algorithms are applied to the hadronic part of the Z^0 decay excluding the photon candidate thus ordering the central tracks and ECAL clusters of the event in jets. At the second stage, the value of the resolution parameter $y_{\gamma,i}$ between each jet i in the event

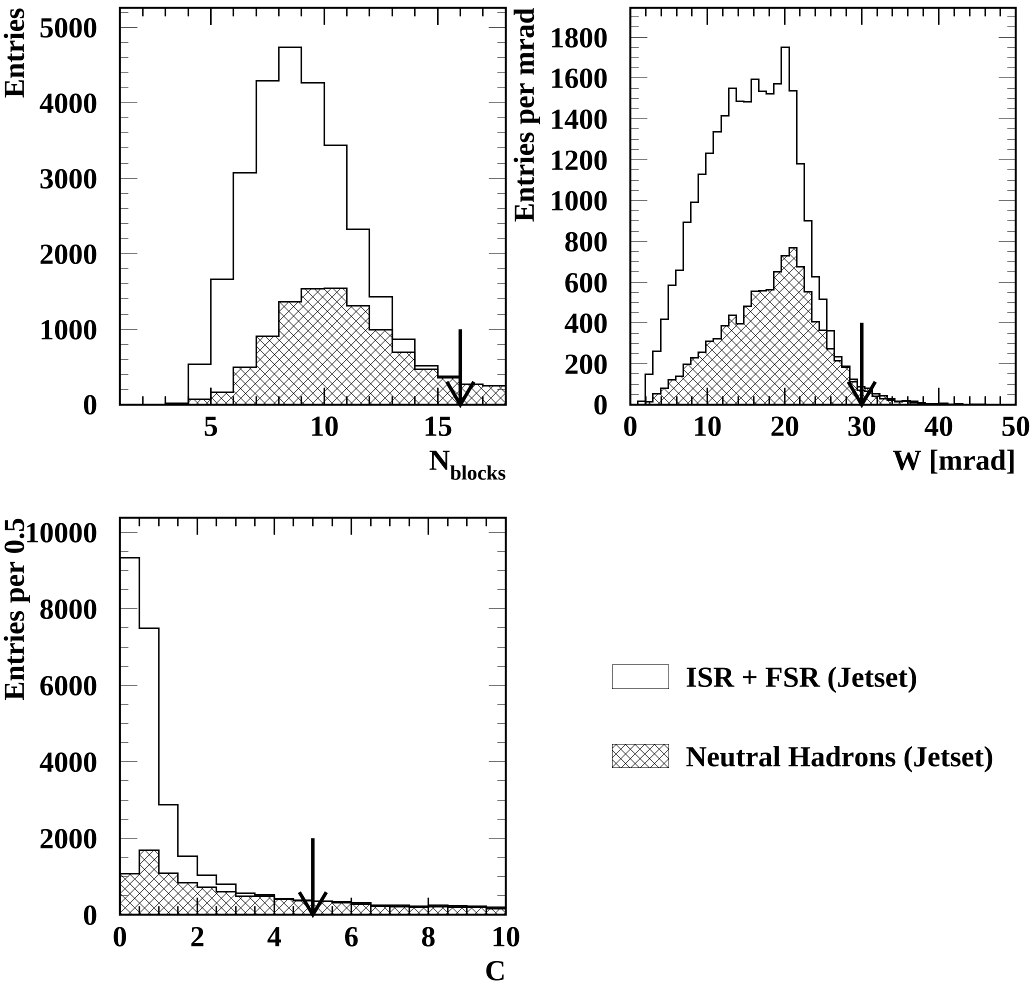

Figure 5.5: Three Monte Carlo distributions describing the shape of a neutral cluster candidate in the barrel region of the electromagnetic calorimeter with an energy of more than 7 GeV: The number of lead glass blocks N_{blocks} assigned to the cluster, its energy weighted angular width W (first moment of cluster), and the respective cluster shape variable C, which both are defined in the previous chapter. The overall contribution from all possible hadronic background sources - mainly π_0 decays to two photons - is also shown (hatched histogram) and motivates the cut values which are indicated as arrows. The distributions are normalised to the available Monte Carlo statistics.

and the photon candidate is required to be greater than the same minimum value y_{cut} as used for the jet definition. For each jet finder twelve values of y_{cut} are considered. The range of y_{cut} values covers the phase space region where the matrix element calculations are available (cf. table 2.2). The input four-momenta for the jet finder schemes are provided by the MT algorithm mentioned above only taking into account the information from the central tracking system and the electromagnetic calorimeter.

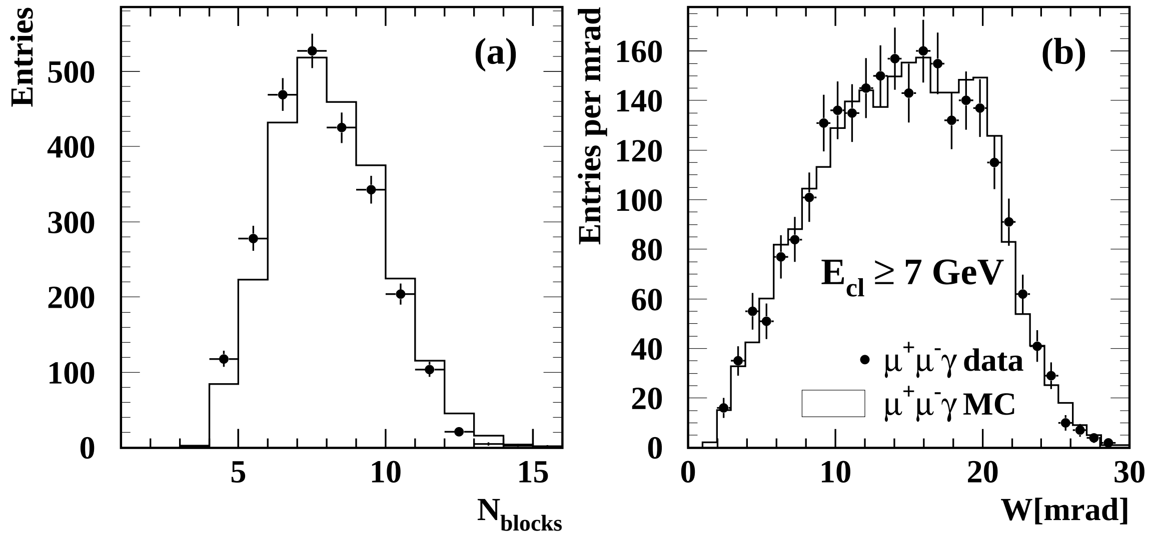

Figure 5.6: The distributions of N_{blocks} and W in the photon reference samples selected from measured and simulated $\mu^+\mu^-$ events as described in section 4.3. The distributions are normalised to the data statistics.

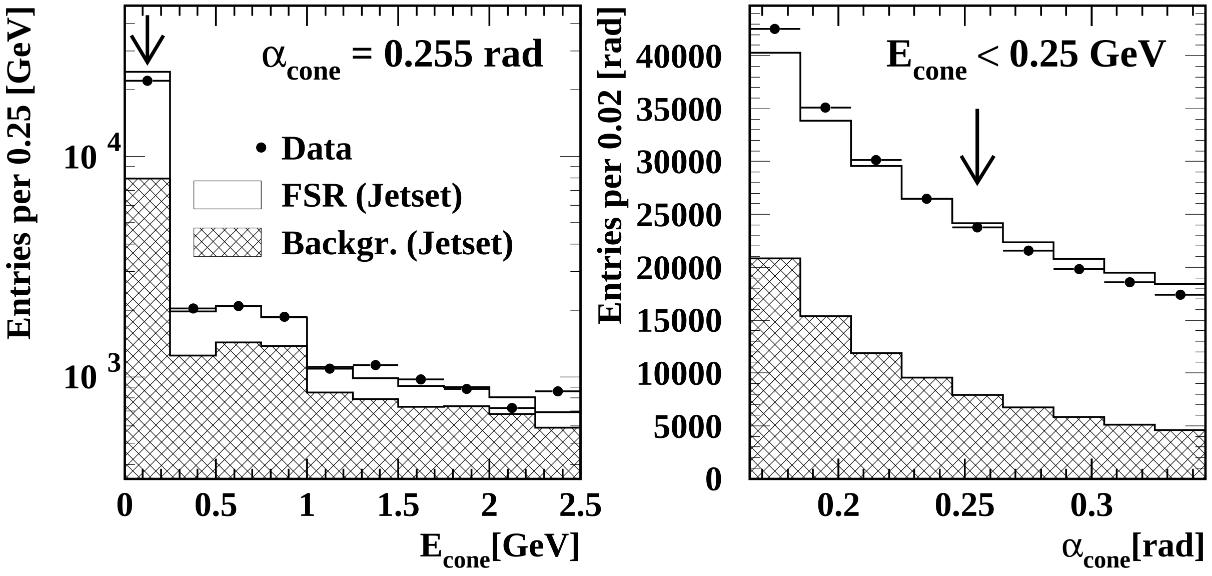

Figure 5.7:
Left plot: the energy inside a cone of half opening angle $\alpha_{cone} = 0.255$ rad for data and Monte Carlo.
Right plot: the number of events with an energy of less than 0.25 GeV inside cones of various half opening angles α_{cone} for data and Monte Carlo.
Both plots are normalised to the Monte Carlo statistics.

A total of 10400 events are retained as candidates for hadronic Z^0 decays with photon bremsstrahlung off the final state (anti)quark after all cuts except for the y cut. The number of events retained after additionally imposing the various y cuts in the applied jet finder algorithms are summarised in table 5.1.

Jade E0		Durham (k_t)	
y_{cut}	Candidates	y_{cut}	Candidates
0.005	7708	0.002	8022
0.01	6896	0.004	7326
0.02	5931	0.006	6753
0.04	4751	0.008	6358
0.06	3913	0.01	5908
0.08	3299	0.012	5573
0.1	2741	0.014	5229
0.12	2358	0.016	4964
0.14	2114	0.02	4546
0.16	1938	0.04	3422
0.18	1830	0.06	2962
0.2	1754	0.1	2566

Table 5.1: Number of candidate events selected with the Jade and Durham algorithm applying twelve different values of y_{cut}.

5.2 Backgrounds and Efficiencies

To obtain the true final state photon rate in multihadronic Z^0 decays the selected sample has to be corrected for both background contamination and measurement efficiencies.

In the first part of this section, it is described in more detail which kind of backgrounds to the measurement are expected, how these are identified, and how their contribution to the selected candidate sample is estimated. The y_{cut}-dependently measured numbers of hadronic Z^0 decays with FSR which are listed in table 5.1 are then corrected for the estimated background fractions. In the second part of this section, limiting factors of the measurement, like background rejection requirements as well as detector deficiencies are discussed. Based on this, the efficiencies of the measurement are determined and all y_{cut}-dependently measured numbers of candidate events are corrected accordingly in both jet finder schemes.

5.2.1 Background Sources and their Estimation

As mentioned earlier, two categories of background sources exist which dilute the measured rate of hadronic Z^0 events with an additional isolated photon emitted by a quark in the final state. Such background events leave two kinds of signatures in the OPAL electromagnetic calorimeter:

1. The first category contains events in which isolated neutral clusters are generated by neutral hadrons or their decay products. Such ECAL clusters can be distinguished from real single-photon clusters by their shape.

2. The second category contains events where photons are emitted by the initial leptons. In such events, the selected isolated ECAL clusters may be generated by single photons from ISR, and thus cannot be separated from the FSR signal clusters by their shape.

5.2.1.1 Background due to Neutral Hadrons and their Decay Products

The composition of the hadronic background in the selected candidate sample as simulated by JETSET 7.4 is shown in figure 5.8. The largest background contribution comes from π^0 mesons decaying into two photons which are not resolved in the electromagnetic calorimeter. These π^0 mesons are either direct fragmentation products (indicated as primary) or decay products of other hadrons (indicated as secondary). The second largest contribution comes from K_L^0 mesons which may deposit enough energy in the ECAL and thus directly generate clusters. The third largest contribution is due to η particles which like the π^0 mesons decay into two photons generating one cluster. Neutrons, ω and ρ decays, and other sources[3] contribute at or below the percent level.

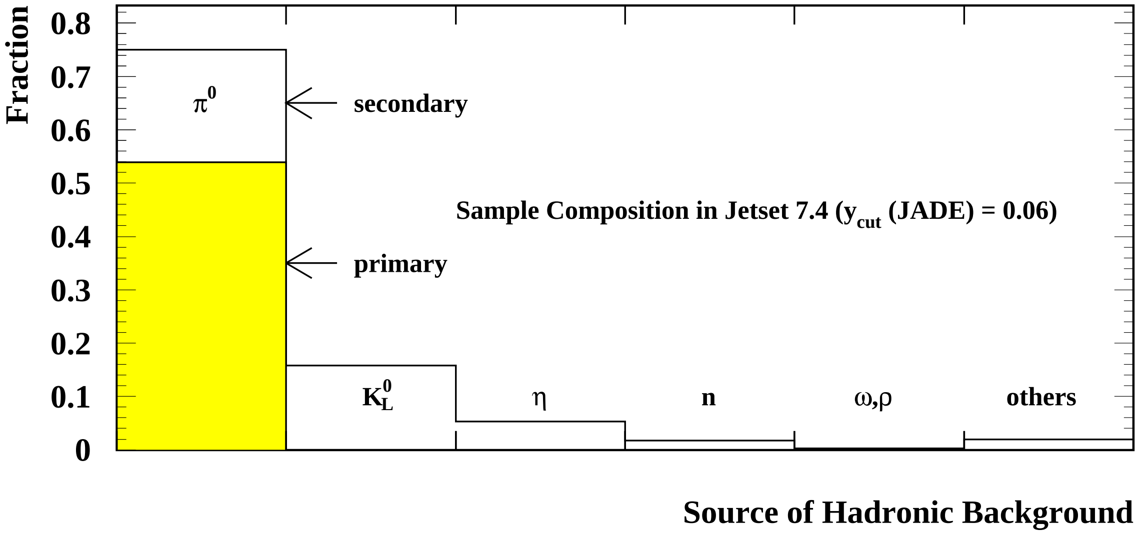

Figure 5.8: The hadronic background composition of the cluster candidate sample as given by JETSET 7.4. The fraction for each source is shown with respect to the total number of selected hadronic clusters in the ECAL.

As discussed in chapter 4, ECAL clusters of these sources differ from single-photon clusters by their shape. This is utilised for the estimation of the hadronic background contribution in the selected sample. The distribution of the cluster shape variable C possesses the necessary discrimination power and a satisfactory agreement for photons in data and Monte Carlo as is proven in the section 4.3 and can be seen in the figures 4.2 (discrimination) and 4.3 (data-Monte Carlo comparison). The C distribution is shown separately for the largest hadronic background sources as generated with JETSET 7.4 in figure 5.9. The inclusive shape of the total 'hadronic' C distribution is dominated by ECAL clusters originating from π^0 decays into two photons. Their C distribution peaks below C=1 whereas the C distributions of all other neutral hadron sources are broad. This results from the kinematics of a two-body decay: the higher the energy of the π^0 the smaller is the angle between the two photons, which therefore produce a narrower

---

[3] Among these are long lived hadrons (e.g. Λ^0), which deposit enough energy in the ECAL, and charged particles (e.g. $\pi^{\pm}$) which may have not been selected by the quality criteria as good tracks or which may come from neutral hadron decays.

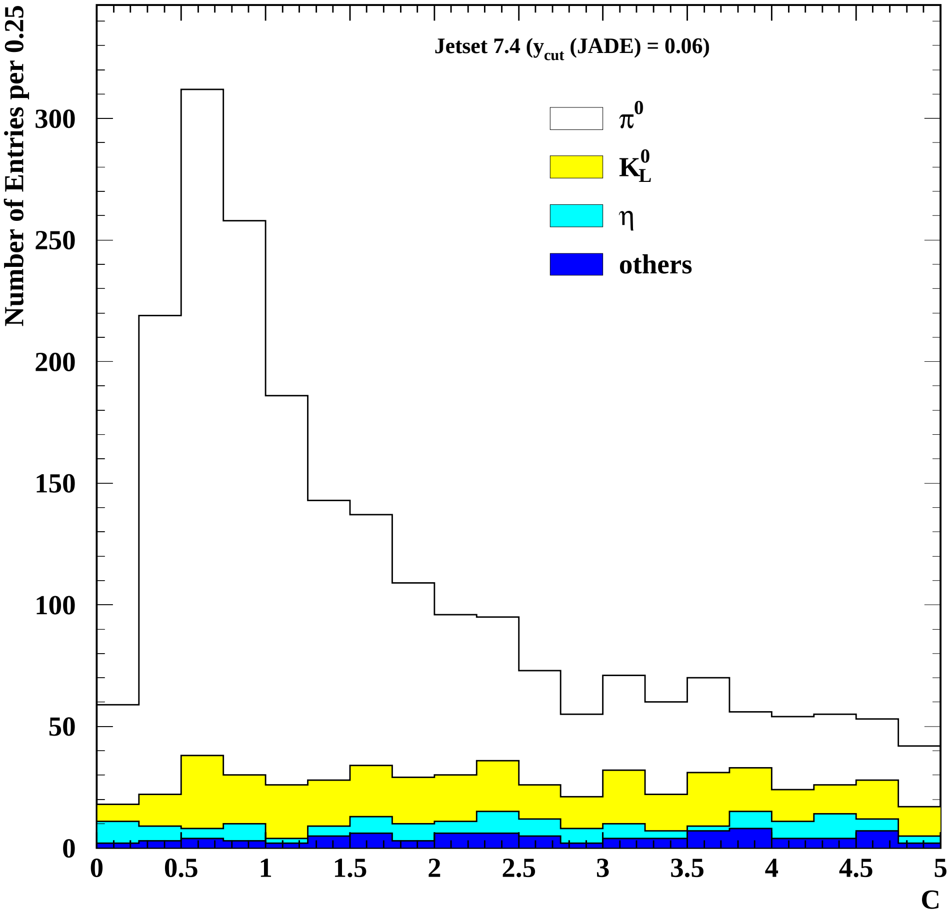

Figure 5.9: The C distribution of the different hadronic background sources in the candidate sample.

cluster of a shape which is similar to the shape of a single-photon cluster. In comparison with the π^0, the η meson decays with a larger opening angle between the two photons because of its mass which is more than four times larger than the π^0 mass. Therefore, η clusters are wider and less photon-like than π^0 clusters at high energies of the mesons, which involves a broad C distribution for electromagnetic showers caused by photons from an η decay.[4]

K_L^0 mesons as well as neutrons may also produce clusters in the ECAL via hadronic interactions with the lead glass. Such clusters have different shapes compared to electromagnetic clusters because hadronic cascades are composed of an electromagnetic component due to π^0 production and a component due to low-energy hadronic activity, and the cascade development is thus more complicated than in the purely electromagnetic case.[5] Therefore, a broad distribution of the photon likeness parameter C is expected and indeed produced by the K_L^0 clusters in the selected

---

[4] On the other hand, the probability that one photon from the decay $\eta \to \gamma\gamma$ generates an isolated single-photon cluster which survives the selection cuts is very small. An η meson with an energy of, say, 7 GeV decays into two photons with a minimum opening angle of 7.5° (most probable case of symmetric decay). Consequently, the cluster of one decay photon would most likely lie inside the isolation cone around the cluster of the other one which thus would be rejected, and vice versa.

[5] The length scale appropriate for hadronic interactions is the nuclear interaction length λ_I. The longitudinal as well as the transverse dimensions of hadronic showers scale as λ_I, which in general is much larger than the radiation length X_0 in massive materials.

Monte Carlo sample, as can be seen in figure 5.9.
The C distribution of all remaining hadronic background sources is shown in figure 5.9, too. However, its contribution to the overall 'hadronic' C shape is only marginal.

5.2.1.2 The Hadronic Background Estimation

The shape of the C distribution is used to estimate the fraction of clusters in the selected candidate sample truly generated by isolated single photons. The corresponding distributions for hadronic ECAL clusters and for single-photon clusters caused by initial and final state radiation are obtained from simulated multihadronic Z^0 decay samples which are generated with JETSET 7.4 at a centre-of-mass energy of exactly the Z^0 mass, and which are then processed with the OPAL detector Monte Carlo program GOPAL. A sample of 8416033 such hadronic events are available from which between 19463 and 5903 (depending on the value of y_{cut} and the jet finder scheme) with final state photon candidates are selected passing the same cuts which are applied to real data.
The C distribution of the selected data clusters is then fitted with a linear combination of the C distributions of single-photon and of hadronic Monte Carlo clusters. As a technique, a binned maximum likelihood method is applied, which takes into account the limited statistics of the utilised Monte Carlo distributions [105]. As starting point of the algorithm serves the expression for the predicted number of events in a bin i:

$$g(C)_i^{pred} = p_\gamma \cdot g(C)_i^\gamma + p_{had} \cdot g(C)_i^{had}, \tag{5.5}$$

where p_γ and p_{had} are called strength factors which include the normalisation factors of the three distributions and which are related to the source fractions f_γ and f_{had} by

$$p_\gamma = f_\gamma \cdot \frac{N_D}{N_\gamma} \qquad \text{and} \qquad p_{had} = f_{had} \cdot \frac{N_D}{N_{had}}, \tag{5.6}$$

where N_D, N_γ, and N_{had} are the total number of events in the data, single-photon, and neutral hadron input histograms. $g(C)_i^\gamma$ and $g(C)_i^{had}$ are the unknown, expected number of events in each bin i for the two sources, whereas $G(C)_i^\gamma$ and $G(C)_i^{had}$ are the corresponding number of events generated by JETSET 7.4. Considering the correlation between the signal and background fraction,

$$f_{had} = 1 - f_\gamma, \tag{5.7}$$

the logarithm of the likelihood $\mathcal{L}$,

$$\begin{aligned} \ln \mathcal{L} \; = \; & \sum_{i=0}^{n_{bins}} G(C)_i^{data} \ln g(C)_i^{pred} - g(C)_i^{pred} \\ & + \sum_{i=0}^{n_{bins}} G(C)_i^\gamma \ln g(C)_i^\gamma - g(C)_i^\gamma + \sum_{i=0}^{n_{bins}} G(C)_i^\gamma \ln g(C)_i^{had} - g(C)_i^{had}, \end{aligned} \tag{5.8}$$

is maximised in a one-parameter fit using the software package MINUIT [106]. As can be seen, the total likelihood is the combined probability of the observed data events $G(C)_i^{data}$ and the

Jade E0		Durham (k_t)	
y_{cut}	Single-photon fraction	y_{cut}	Single-photon fraction
0.005	0.9006 ± 0.0094	0.002	0.8882 ± 0.0097
0.01	0.9118 ± 0.0095	0.004	0.8968 ± 0.0099
0.02	0.9162 ± 0.0107	0.006	0.8925 ± 0.0106
0.04	0.9190 ± 0.0117	0.008	0.8922 ± 0.0107
0.06	0.9124 ± 0.0134	0.01	0.8912 ± 0.0107
0.08	0.8904 ± 0.0153	0.012	0.8950 ± 0.0100
0.1	0.8835 ± 0.0171	0.014	0.8940 ± 0.0120
0.12	0.8635 ± 0.0199	0.016	0.8903 ± 0.0126
0.14	0.8300 ± 0.0231	0.02	0.8860 ± 0.0128
0.16	0.8057 ± 0.0242	0.04	0.8378 ± 0.0175
0.18	0.7723 ± 0.0332	0.06	0.7997 ± 0.0204
0.2	0.7345 ± 0.0287	0.1	0.7800 ± 0.0237

Table 5.2: Single-photon fractions for the Jade and Durham algorithm with twelve different values of y_{cut}. The errors are the combined data and Monte Carlo errors as given by the binned maximum likelihood fit.

observed Monte Carlo events for each source $G(C)_i^{\gamma}$ and $G(C)_i^{had}$ in all n bins of the distribution. More details about the solution of equation 5.8 (e.g. special considerations which apply if one or more of the source Monte Carlos in one bin are zero) may be found in [105].

The fit is based on C distributions in the range between 0 and 5, and performed separately in eight bins of cluster energy. The bins are chosen in such a way that C_{γ} and C_{had} distributions only show a small dependence on the cluster energy. The C distributions resulting from the fit together with the C distributions in data are plotted separately for the eight bins of cluster energy in figure 5.10. As an example, the y_{cut} value 0.06 in the Jade scheme is chosen. The values for χ^2 only taking into account the statistics of the data distribution vary between 19.4 and 55.5 per 19 d.o.f.. The fractions yielded by the fit in the eight energy bins are shown in figure 5.11. As expected, they vary depending on the measured cluster energy, with lower single-photon fractions at higher cluster energies, which is due to the increasing π^0 background as argued above (smaller opening angle of π^0 decay at larger energies). To get the overall single-photon fraction in the selected sample, the weighted mean of the resulting fractions in the eight energy bins taking into account the statistics in each bin is calculated. These overall fractions are listed for both jet algorithms and their twelve different y_{cut} values in table 5.2. The assigned errors are calculated accordingly from the errors given by the binned maximum likelihood fit based on equation 5.8, and thus take into account the effect of finite Monte Carlo statistics. In both jet finder schemes, with increasing y_{cut} values also the errors on the fractions grow, since fewer and fewer events in Monte Carlo as well as in data pass the y_{cut}. Hence, not only for physics but also for technical reasons the analysis will focus on a moderate y_{cut} range, where the measured couplings will be extracted. Especially, for very high values of y_{cut} the input information to the maximum likelihood fit becomes very poor in the lowest cluster energy bin, and for the respective C distributions statistics is lacking.

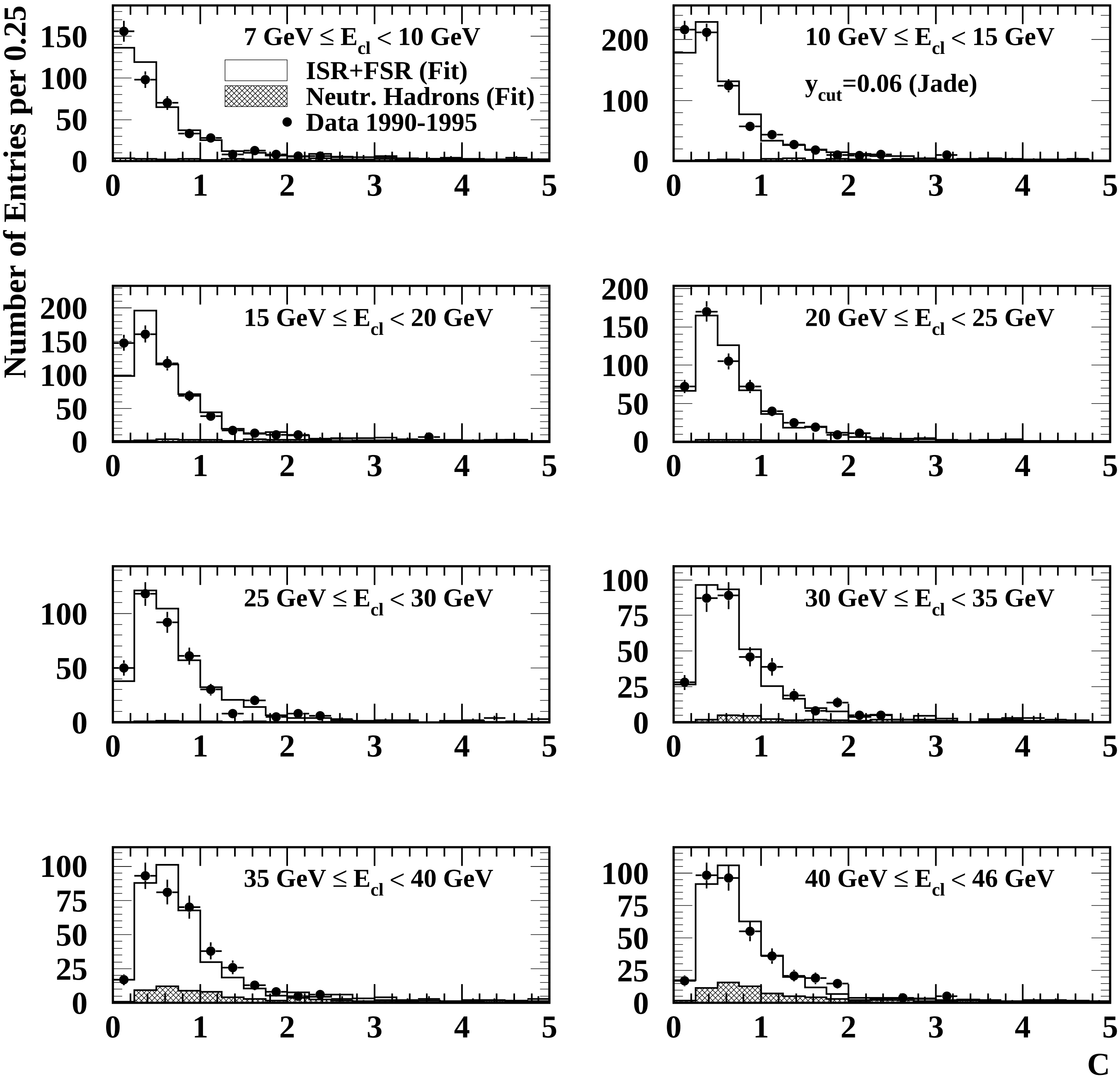

Figure 5.10: The data distributions of the cluster shape variable C in eight bins according to the measured cluster energy and the corresponding fit result in each bin.

To estimate the contribution to the total fit error from the data and Monte Carlo samples used, the error is split up in two according to the statistics of the two samples for each value of y_{cut} in the two jet recombination schemes. The resulting errors are listed together with the total fit errors in table 5.3.

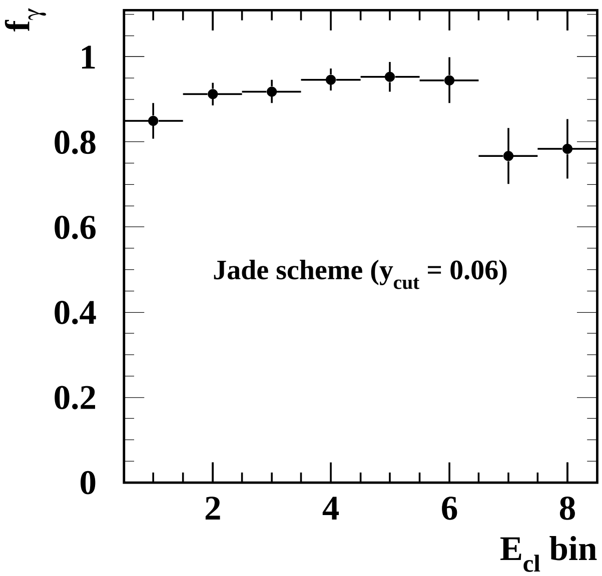

Figure 5.11: The fractions of true single-photon clusters as obtained from the fit in eight energy bins shown in figure 5.10.

Jade E0				Durham (k_t)			
y_{cut}	tot. error	data	MC	y_{cut}	tot. error	data	MC
0.005	0.0094	0.0079	0.0050	0.002	0.0097	0.0082	0.0053
0.01	0.0095	0.0080	0.0051	0.004	0.0099	0.0084	0.0053
0.02	0.0107	0.0091	0.0057	0.006	0.0106	0.0090	0.0057
0.04	0.0117	0.0100	0.0062	0.008	0.0107	0.0091	0.0057
0.06	0.0134	0.0114	0.0070	0.01	0.0107	0.0091	0.0057
0.08	0.0153	0.0130	0.0080	0.012	0.0100	0.0085	0.0053
0.1	0.0171	0.0146	0.0088	0.014	0.0120	0.0102	0.0063
0.12	0.0199	0.0171	0.0101	0.016	0.0126	0.0108	0.0066
0.14	0.0231	0.0209	0.0116	0.02	0.0128	0.0110	0.0066
0.16	0.0242	0.0210	0.0120	0.04	0.0175	0.0151	0.0089
0.18	0.0332	0.0289	0.0164	0.06	0.0204	0.0177	0.0102
0.2	0.0287	0.0251	0.0140	0.1	0.0237	0.0206	0.0118

Table 5.3: The absolute errors on the photon fraction as given by the binned maximum likelihood fit and their estimated contributions from data and Monte Carlo statistics.

5.2.1.3 Cross-Check of the Hadronic Background Estimation

To verify that the binned maximum likelihood method yields reliable results in the estimation of the hadronic background in the selected cluster sample, it has been cross-checked against statements on the rate of isolated neutral hadrons[6] in other measurements by the experiments

---

[6] Here, isolation means an additional energy of less than 500 MeV in a cone of half angle 0.255 rad around the ECAL cluster is allowed. The isolation of the candidate from the jets in the event is not required.

OPAL [107] and L3 [59]. In [107] it is pointed out that JETSET underestimates the rate of isolated η mesons with an energy of $E_\eta > 4.5$ GeV by a factor of 2.07 ± 0.11, and the rate of isolated π^0 mesons in an energy range of $4.5 - 22.825$ GeV by a factor of 1.99 ± 0.05. L3 [59] measures the rate of isolated clusters in their ECAL from all possible neutral hadron sources to be by a factor of 1.88 ± 0.08 larger than predicted with JETSET.

To test the binned maximum likelihood fit which is used in the present analysis, it is performed in 10 bins of cluster energies between 4.5 GeV and 46 GeV using the C distributions of clusters which have passed all cuts except for the y cut. The results are compared with the rate of isolated neutral hadrons as predicted by JETSET. According to the likelihood fit, JETSET underestimates the rate by a factor of

1. 2.02 ± 0.04 for cluster energies between 4.5 to 20 GeV, and
2. 2.05 ± 0.03 for all cluster energies greater than 4.5 GeV,

where the errors represent the uncertainties of the fit results accounting for both data and Monte Carlo statistics. The above factors are similar to those observed in [107] and [59]. Moreover, the tendency of the hadronic background behaviour as seen by L3, which is, that the data-Monte Carlo discrepancy increases with a tighter isolation cut and is largest for intermediate cluster energies (here: $10 < E < 30$) [108] has been confirmed by studies with the present likelihood method.

From these observations it can be concluded that the background estimations resulting from the fit are reliable.

5.2.1.4 Background due to Initial State Radiation

The second group of background contributions to the selected candidate sample, clusters generated by initial state photons is not distinguishable from the signal clusters by means of experimental methods, since the shape of ECAL clusters generated by ISR is the same. Though the ISR background is already reduced by the cuts on the cluster energy and angle, it is still expected to amount to a few percent of the isolated single-photon clusters. The only possibility to estimate the initial state radiation is to rely on Monte Carlo calculations. Here, the recently released Monte Carlo $\mathcal{KK}$ [109] is used. It is based on the calculation of photon emission from the incoming e^+e^- beams up to the second order QED, includes electroweak corrections in first order with higher order extensions, and the exact matrix elements for up to two photons. Because the $\mathcal{KK}$ Monte Carlo is only available on tree level and not as fully processed detector data set, the background due to initial state radiation has to be subtracted on the tree (hadron) level.

Efficiency Correction, Part I

As a consequence, the rate of single photons, which is estimated with the binned maximum likelihood fit, has to be corrected for detector and measurement effects. The efficiency corrections are calculated for each y_{cut} value in the two jet finder schemes,

$$c^{ISR+FSR}(y_{cut}) = \frac{N^{ISR+FSR}_{hadron}(y_{cut})}{N^{ISR+FSR}_{detector}(y_{cut})}, \tag{5.9}$$

Jade E0		Durham (k_t)	
y_{cut}	Correction factor	y_{cut}	Correction factor
0.005	1.127 ± 0.005	0.002	1.128 ± 0.005
0.01	1.124 ± 0.006	0.004	1.134 ± 0.005
0.02	1.128 ± 0.006	0.006	1.142 ± 0.005
0.04	1.138 ± 0.007	0.008	1.140 ± 0.006
0.06	1.141 ± 0.007	0.01	1.144 ± 0.006
0.08	1.147 ± 0.008	0.012	1.141 ± 0.006
0.1	1.142 ± 0.010	0.014	1.129 ± 0.006
0.12	1.127 ± 0.011	0.016	1.125 ± 0.007
0.14	1.113 ± 0.012	0.02	1.110 ± 0.007
0.16	1.086 ± 0.012	0.04	1.092 ± 0.009
0.18	1.072 ± 0.013	0.06	1.074 ± 0.009
0.2	1.067 ± 0.013	0.1	1.055 ± 0.011

Table 5.4: The correction factors $c^{ISR+FSR}(y_{cut})$, which take into account detector inefficiency.

using a sample of events with final or initial state photons selected from the existing 8.4 million multihadronic Z^0 decays generated with JETSET and processed with GOPAL. The photon energy, polar angle, and isolation cuts described previously are applied on the detector and on the hadron level of the JETSET sample, as well in the $\mathcal{KK}$ Monte Carlo, which is linked with the PYTHIA 6.1 Package [110] for the hadronisation of the final partons. The resulting factors $c^{ISR+FSR}(y_{cut})$ are listed in table 5.4 together with their errors due to the limited Monte Carlo statistics. They correct for detector effects and reflect efficiency losses due to photon conversions in the beam pipe and in the central tracking system of the detector, and also distortions of the y_{cut}-dependent photon rate due to incorrect measurements of the photon, jet, and visible energy as well as of the stable particle directions.

ISR Subtraction

After the correction has been applied to the estimated single photon rate on detector level the number of events with an isolated initial state photon of an energy larger than 7 GeV and within a polar angle range of $|\cos\theta_\gamma| < 0.72$ as calculated with $\mathcal{KK}$ is subtracted. The corresponding numbers of ISR events are given in table 5.5. They are calculated based on 16 million hadronic Z^0 decays, in which the events with initial state radiation passing the above cuts are counted and then are normalised to the 3022897 multihadronic Z^0 events which have been collected by the OPAL detector. The given errors in table 5.5 are merely due to the Monte Carlo statistics. Since the interference between initial and final state radiation is expected to be small on the Z^0 peak, its contribution to the photon sample is neglected here. Possible systematic effects from ISR-FSR interference will be discussed later on in subsection 5.4.1.2.

The entirely background and partly efficiency corrected event numbers in the framework of the two jet finder schemes,

$$n^{FSR}_{corr1}(y_{cut}) = n^{FSR}_{raw}(y_{cut}) \cdot f_\gamma(y_{cut}) \cdot c^{ISR+FSR}(y_{cut}) - n^{ISR}_{\mathcal{KK}}(y_{cut}), \tag{5.10}$$

Jade E0		Durham (k_t)	
y_{cut}	Number of ISR events	y_{cut}	Number of ISR events
0.005	342 ± 8	0.002	366 ± 8
0.01	326 ± 8	0.004	351 ± 8
0.02	296 ± 7	0.006	326 ± 8
0.04	256 ± 7	0.008	302 ± 8
0.06	219 ± 6	0.01	282 ± 7
0.08	180 ± 6	0.012	254 ± 7
0.1	141 ± 5	0.014	237 ± 7
0.12	122 ± 5	0.016	217 ± 6
0.14	107 ± 4	0.02	194 ± 6
0.16	96 ± 4	0.04	148 ± 5
0.18	88 ± 4	0.06	125 ± 5
0.2	82 ± 4	0.1	108 ± 5

Table 5.5: The number of expected background events in the selected candidates sample due to initial state radiation as calculated by the $\mathcal{KK}$ Monte Carlo generator on hadron level. The errors reflect the available Monte Carlo statistics.

Jade E0		Durham (k_t)	
y_{cut}	Corrected number of events	y_{cut}	Corrected number of events
0.005	$7484 \pm 68 \pm 58$	0.002	$7668 \pm 74 \pm 60$
0.01	$6744 \pm 62 \pm 53$	0.004	$7101 \pm 69 \pm 57$
0.02	$5833 \pm 61 \pm 50$	0.006	$6557 \pm 69 \pm 55$
0.04	$4714 \pm 54 \pm 44$	0.008	$6165 \pm 66 \pm 53$
0.06	$3853 \pm 51 \pm 41$	0.01	$5745 \pm 61 \pm 50$
0.08	$3189 \pm 49 \pm 40$	0.012	$5435 \pm 54 \pm 46$
0.1	$2624 \pm 46 \pm 37$	0.014	$5040 \pm 60 \pm 48$
0.12	$2174 \pm 45 \pm 35$	0.016	$4755 \pm 60 \pm 48$
0.14	$1846 \pm 47 \pm 35$	0.02	$4278 \pm 55 \pm 44$
0.16	$1601 \pm 44 \pm 32$	0.04	$2984 \pm 56 \pm 42$
0.18	$1427 \pm 57 \pm 37$	0.06	$2418 \pm 56 \pm 40$
0.2	$1292 \pm 47 \pm 32$	0.1	$2003 \pm 56 \pm 39$

Table 5.6: The number of selected candidate events in data corrected for background contributions and detector inefficiencies. The first error contribution represents the statistical uncertainty from data, which has been estimated as explained at the end of section 5.2.1.2. The second contribution combines the statistical uncertainties of the background and efficiency estimation coming from the JETSET and $\mathcal{KK}$ Monte Carlo samples.

are summarised in table 5.6. The added errors are the combined errors from data and Monte Carlo statistics, which enter through the background estimation and the efficiency correction.

Jade E0		Durham (k_t)	
y_{cut}	Correction factors	y_{cut}	Correction factors
0.005	1.708 ± 0.009	0.002	1.780 ± 0.009
0.01	1.588 ± 0.009	0.004	1.646 ± 0.009
0.02	1.507 ± 0.008	0.006	1.596 ± 0.008
0.04	1.447 ± 0.008	0.008	1.559 ± 0.008
0.06	1.428 ± 0.009	0.01	1.538 ± 0.008
0.08	1.428 ± 0.010	0.012	1.522 ± 0.009
0.1	1.441 ± 0.011	0.014	1.516 ± 0.009
0.12	1.465 ± 0.013	0.016	1.510 ± 0.009
0.14	1.494 ± 0.015	0.02	1.509 ± 0.009
0.16	1.532 ± 0.016	0.04	1.542 ± 0.012
0.18	1.559 ± 0.018	0.06	1.622 ± 0.014
0.2	1.611 ± 0.019	0.1	1.816 ± 0.018

Table 5.7: Efficiency corrections for the Jade and Durham algorithm with twelve different values of y_{cut} calculated based on a sample of 8.4 million multihadronic JETSET events.

5.2.2 Efficiency Correction, Part II

In order to compare the measured final state photon rate with the yield of the $\mathcal{O}(\alpha\alpha_s)$ matrix element Monte Carlo GNJETS, the rate has to be corrected for the remaining cuts, which are:

- the polar angle requirement: $|\cos\theta| \leq 0.72$, and
- the first (cone) isolation requirement: $E_{cone}(0.255 \text{ rad}) < 0.25$ GeV,

as well as for fragmentation effects. The latter may also influence the number of jets which are defined in an event, and affect the second isolation criterion, requiring the radiated photon to be isolated from any jet in the event. It is not corrected for the energy requirement as GNJETS allows to compute the exclusive rate of FSR photons with a minimum energy of 7 GeV (c.f. section 2.3.1.5), so that further systematic uncertainties due to such a correction are avoided. As in the case of the detector efficiency correction before the ISR background subtraction, correction factors are determined for each of the twelve y_{cut} values in the two jet finder schemes using the JETSET generator. The final state photons on hadron level meeting all the above requirements and the final state photons on parton level only meeting the jet finder requirement are counted and the correction factors are calculated as

$$c^{FSR}(y_{cut}) = \frac{N^{FSR}_{parton}(y_{cut})}{N^{FSR}_{hadron}(y_{cut})}. \tag{5.11}$$

The hadron-to-parton level corrections $c^{FSR}(y_{cut})$ are listed in table 5.7 for the Jade and Durham algorithm. The listed errors are due to the limited Monte Carlo statistics, which is given by the overall sample of about 8.4 million multihadronic Z^0 decays. The efficiency loss due to the

Jade E0		Durham (k_t)	
y_{cut}	Corrected number of events	y_{cut}	Corrected number of events
0.005	$12786 \pm 117 \pm 154$	0.002	$13648 \pm 132 \pm 167$
0.01	$10707 \pm 99 \pm 125$	0.004	$11685 \pm 114 \pm 137$
0.02	$8788 \pm 92 \pm 105$	0.006	$10466 \pm 110 \pm 125$
0.04	$6822 \pm 78 \pm 86$	0.008	$9611 \pm 102 \pm 115$
0.06	$5503 \pm 73 \pm 77$	0.01	$8835 \pm 94 \pm 107$
0.08	$4554 \pm 70 \pm 73$	0.012	$8271 \pm 82 \pm 100$
0.1	$3780 \pm 66 \pm 69$	0.014	$7642 \pm 91 \pm 99$
0.12	$3184 \pm 67 \pm 66$	0.016	$7182 \pm 91 \pm 96$
0.14	$2758 \pm 70 \pm 66$	0.02	$6456 \pm 84 \pm 90$
0.16	$2454 \pm 68 \pm 63$	0.04	$4601 \pm 87 \pm 83$
0.18	$2225 \pm 88 \pm 70$	0.06	$3922 \pm 91 \pm 85$
0.2	$2081 \pm 76 \pm 65$	0.1	$3638 \pm 101 \pm 97$

Table 5.8: The corrected number of selected candidate events in the two jet finder schemes for twelve different values of y_{cut}. The first error contribution is due to the uncertainty from data statistics, the second contribution represents the combined uncertainty from the Monte Carlo statistics.

polar angle cut as calculated with JETSET amounts to around 30% of the isolated and highly energetic photons independent of the y_{cut}. The isolation cut rejects between 5 and 18% (Jade) resp. 8 and 22% (Durham) of the highly energetic final state photons. The loss is larger at small values of y_{cut}, is getting smaller with increasing values and rises again for very high values of y_{cut}. Small values of y_{cut} mean a weak isolation of the photon candidate from the jets in the event, large values of y_{cut} force most of the events in a 1-jet structure. In both cases, efficiency losses due to the cone isolation become more important.

5.3 The Total Corrected Number of Events with an Isolated Photon

The corrected numbers of final state photons generated by radiation off the final state (anti)quarks in 3022897 multihadronic Z^0 decays,

$$n^{FSR}_{corr2}(y_{cut}) = n^{FSR}_{corr1}(y_{cut}) \cdot c^{FSR}(y_{cut}), \tag{5.12}$$

are summarised in table 5.8. The errors represent the uncertainties due to the limited data and Monte Carlo statistics.

5.4 Systematic Errors

The description of the systematic studies is ordered according to the analysis steps described in the preceding sections.

5.4.1 Uncertainties of the Background Estimation

5.4.1.1 Estimation of Hadronic Sources

The amount of hadronic background clusters in the selected candidate sample is estimated using a binned maximum likelihood fit as described in section 5.2.1.2. This method relies on a proper simulation of the detector, especially on the simulation of electromagnetic showers in the ECAL, and on a correct simulation of the hadronic background composition as generated with JETSET 7.4. Thus, the results of the likelihood fit have to be checked for dependences on possible Monte Carlo deficiencies, both on the detector and the event generator side. The main sources of systematic uncertainties which have been checked are listed in table 5.9 together with the relative error resulting from the fit regarding data and Monte Carlo statistics (column labelled with $C^{\gamma,had}_{MC}$, cf. table 5.2). The estimation of possible systematic biases is described in the following.

For all the subsequently described studies, the likelihood fit has been repeated with C distributions which are differently generated or modelled, depending on which source of systematic uncertainty has been investigated. In each case, the difference between the y_{cut}-dependent fraction originally resulting from the fit and the fraction obtained with the modified C distributions is quoted in table 5.9.

In the column labelled with C^{γ}_{ref}, the systematic error contribution originating from inadequate simulation of single-photon clusters in the ECAL is listed. To quantify this, the maximum likelihood fit has been repeated in each cluster energy bin with C distributions of prompt photons selected with almost hundred percent purity from the $\mu^+\mu^-\gamma$ reference data sample[7] as signal distributions instead of the C distributions of ISR and FSR clusters selected from multihadronic decays simulated with JETSET. For most of the y_{cut} values, the deviation is smaller than the combined statistical error from data and Monte Carlo given by the fit (cf. column one). Note also that the errors resulting when performing the fit with the reference photon sample are larger than the original fit errors.

The second and third column (labelled with C^{had}_{HERWIG} and $C^{had}_{reweighted}$) contain the deviations reflecting the sensitivity of the likelihood fit to the hadronic background composition.
For the numbers quoted in the second column, the fit has been repeated using the C^{had} distribution as resulting from the background spectrum predicted by the HERWIG generator. The observed differences between the fractions of prompt photons obtained from the data fitted with the distribution of C^{had} generated with HERWIG and JETSET are large for high and low (only in the Durham scheme) values of y_{cut}. Note however, that the statistics provided by the HERWIG Monte Carlo is smaller than that of JETSET (2.4 million multihadronic Z^0 decays generated with HERWIG compared to 8.4 million generated with JETSET). The values of χ^2 resulting for the fits only taking into account the statistics of the C distributions in data are always larger in the HERWIG than in the JETSET case. Therefore, considering this deviation in the systematic error combination results in a conservative estimate.
The numbers in the third column reflect the variation of the resulting signal fraction if the likelihood fit is repeated with C^{had} distributions which are modelled by reweighting the relative hadronic background spectrum according to inclusive measurements of neutral hadron

---

[7] which is also used for the data and Monte Carlo comparison described in section 4.3.

Jade E0					
y_{cut}	$C_{MC}^{\gamma,had}$	C_{ref}^{γ}	C_{HERWIG}^{had}	$C_{reweighted}^{had}$	C_{smear}
0.005	±1.0	-2.2	-0.2	-0.6	0.5
0.01	±1.0	-1.9	-2.8	-0.7	0.1
0.02	±1.2	-1.8	1.5	-0.6	1.6
0.04	±1.3	0.6	2.4	-0.8	2.2
0.06	±1.5	0.7	-1.2	-0.9	0.9
0.08	±1.7	1.7	3.3	-1.0	0.9
0.1	±1.9	5.8	2.1	-1.5	-0.1
0.12	±2.3	-1.2	2.6	-0.9	-0.1
0.14	±2.8	-0.4	2.8	-1.3	-0.3
0.16	±3.0	0.4	-2.7	-2.8	-1.9
0.18	±4.3	1.4	8.3	-5.0	-1.0
0.2	±3.9	4.7	10.3	-3.6	1.2

Durham (k_t)					
y_{cut}	$C_{MC}^{\gamma,had}$	C_{ref}^{γ}	C_{HERWIG}^{had}	$C_{reweighted}^{had}$	C_{smear}
0.002	±1.1	-1.5	-6.0	-0.8	0.4
0.004	±1.1	-1.5	-3.6	-0.7	0.1
0.006	±1.2	-1.1	-2.2	-0.8	0.7
0.008	±1.2	-0.4	1.8	-0.8	0.8
0.01	±1.2	-0.1	1.3	-0.9	0.8
0.012	±1.1	-0.4	1.3	-1.1	0.6
0.014	±1.3	-1.2	1.8	-1.1	0.1
0.016	±1.4	-0.8	1.7	-1.2	0.1
0.02	±1.4	0.4	3.1	-1.2	-0.8
0.04	±2.1	0.5	4.8	-1.9	-0.7
0.06	±2.6	2.3	4.5	-2.5	0.2
0.1	±3.0	3.0	5.2	-2.2	3.1

Table 5.9: Systematic error contributions to the single-photon fraction as resulting from the binned maximum likelihood fit. Listed are the uncertainties relative to the single-photon fraction (%). For comparison, the error contributions due to finite Monte Carlo and data statistics of the C distributions (the mere fit error contributions, see table 5.2) are also given in the column labelled with $C_{MC}^{\gamma,had}$. For details concerning the studied systematics see text.

production in Z^0 decays as performed for π^0 and η in [107], and for K_L^0 in [111]. By combining the results of these publications, the relative proportions of π^0, η, and K_L^0 are estimated depending on the energy of the meson. These proportions are compared to the proportions in the hadronic background sample selected from the JETSET events in the corresponding energy bins without applying the isolation requirements. Thus, eight weight factors are extracted, which are applied to the contributing hadronic sources in the candidate sample selected in the corresponding energy bins in consideration of the cone and the y_{cut} isolation. The remodelled C distributions of the hadronic background are used in the fit. For all y_{cut} values, the fitted single-photon fractions are below the results using the JETSET distributions. One has to keep in mind, however, that the results for each y_{cut} are correlated.

In the last column, labelled with C_{smear}, the variation of the single photon fraction is listed for the case that the fit is performed after the tracking parameter resolutions are deteriorated by 10%. This might influence the sample composition, as the selection of isolated clusters is affected. Although the results mostly agree with the originally fitted fractions within the errors, the differences are listed here.

Further systematic studies have been carried out. For instance, it has been checked whether the fit result depends on the bin size of the C distribution, which has been changed by a factor of two. In addition, the entire analysis has been repeated for a different upper C boundary, which has been moved from five to ten. No significant change in the resulting signal rate is detected.

The errors listed in table 5.9 are added up quadratically to the total error on the hadronic background estimation.

5.4.1.2 Estimation of Initial State Radiation

The precision of the integrated cross-sections on which the generation of initial state radiation by the $\mathcal{KK}$ Monte Carlo is based varies between $0.02 - 0.2\%$ [109]. Comparing a sample of $\mathcal{KK}$ events generated with and without ISR-FSR interference an average difference of the photon yields in both scenarios of 1.5% relative to the ISR yield is determined. This number is assigned as a systematic uncertainty of the estimated background from initial state radiation. However, one has to keep in mind, that although initial-final state QED interference is included in the new $\mathcal{KK}$ Monte Carlo, QED-QCD corrections are not. The emission of final-state gluons by quarks which competes with final-state photon radiation is neglected when calculating the ISR-FSR interference. This may change the interference corrections for hadronic final states. In [112] a conservative estimate of 50% is given for this change.

5.4.2 Uncertainties of the Efficiency Correction

Since the determination of the efficiency corrections is based on Monte Carlo, both the event generation and the detector simulation have to be reviewed to search for potential deficiencies in their description of real data.

	$(E_{cl} - E_\gamma)/E_{cl}$	
E_{cl}	[98]	figure 5.12
$7.5 - 10$ GeV	4.7 ± 0.3	4.5 ± 0.09
$10 - 15$ GeV	4.8 ± 0.2	4.0 ± 0.06
$15 - 20$ GeV	3.5 ± 0.2	3.1 ± 0.05
$20 - 35$ GeV	3.7 ± 0.2	3.0 ± 0.03
$35 - 50$ GeV	2.6 ± 0.1	2.2 ± 0.04

Table 5.10: A comparison of the calculated energy resolutions in [98] and in this thesis.

5.4.2.1 Uncertainties due to Deficiencies of the Detector Simulation (Uncertainties of $c^{ISR+FSR}(y_{cut})$)

The following systematic studies have been carried out to determine possible systematic uncertainties of the photon selection due to an inadequate detector simulation:

- The efficiency of the single-photon selection has been compared earlier for the reference sample of $\mu\mu\gamma$ events in data and Monte Carlo. The cluster shape properties which were reviewed are: the number of ECAL blocks contributing to a photon cluster ($N_{blocks} < 16$), its energy weighted first moment ($W < 30$ mrad), and the cluster shape fit variable ($C < 5$). A good agreement was observed for cluster energies larger than 7 GeV (c.f. table 4.3, and the figures 4.3, and 5.6(b)). The shift of the N_{blocks} distribution in data compared to the simulation (c.f. figure 5.6(a)) was found to not result in different efficiencies.

- The accuracy of the track parameter measurement in the central detector has been worsened by 10% which may have an effect on the jet finding and both isolation criteria.

- The energy resolution of the ECAL has been deteriorated by 20%. This number has been chosen because the energy resolution of isolated prompt photon clusters selected in the hadronic JETSET sample and in the $\mu\mu\gamma$ reference data sample differ by up to 20% depending on the cluster energy. The results of the fit which has been performed to estimate the resolution in the JETSET sample in energy bins corresponding to those in [98] can be seen in figure 5.12. In table 5.10, the resolutions obtained by the fit are compared to those in [98]. The relevant expression for the resolution as measured in [98] is quoted as equation 5.4 in this thesis.
  The corrected cluster energies have also been shifted by 0.1-0.2 GeV. The numbers reflect the difference in the mean values of the distribution of of $E_{cl} - E_\gamma$ in the simulation and of $E_{cl} - E_{kin}$ in data, where E_{kin} is the kinematically reconstructed energy of the isolated photon in the $\mu\mu\gamma$ reference sample.

- The angular resolution of the photon clusters has been worsened by 30%.

All those studies result in variations of the photon rate which are much smaller than the statistical errors. The effect on the correction factors $c^{ISR+FSR}(y_{cut})$ listed in table 5.4 is at or below the per mille level.

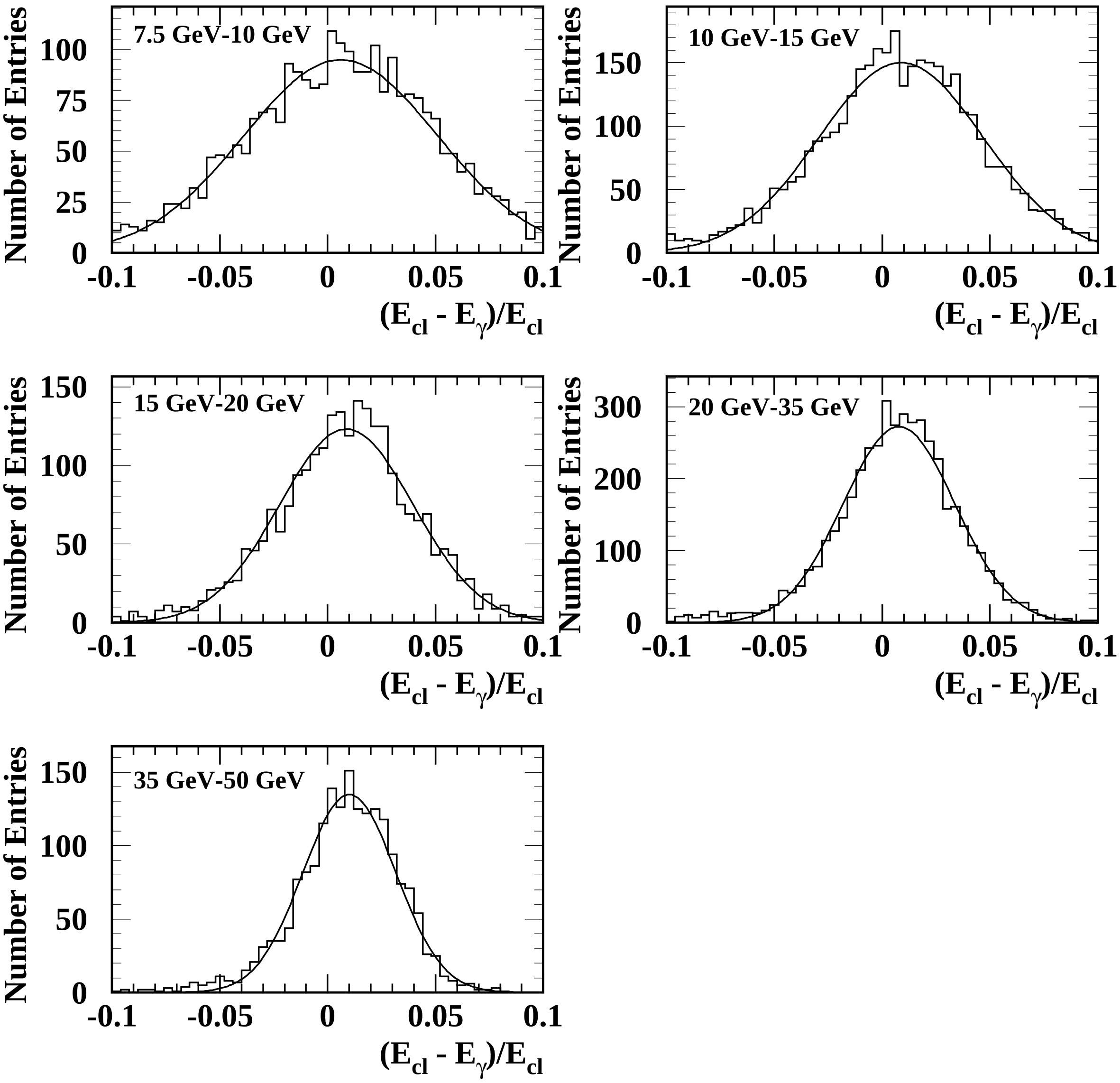

Figure 5.12: The resolution of the corrected energy E_{cl} defined by equation 5.3 as obtained with prompt photons selected from a JETSET sample.

Another and one of the largest contributions to the systematic uncertainty on the correction factor $c^{ISR+FSR}(y_{cut})$ comes from the inadequate simulation of photon conversions. An estimated error of ±10% ([113]) on the simulated conversion rate of around 8% (slightly increasing with higher y_{cut} values) translates into a relative error on the efficiency correction of up to nearly 1% (absolute values of up to 0.01).

The systematic studies described so far are sensitive to the photon selection efficiency on detector level, disregarding possible biases introduced by a potential misrepresentation of the measured jet energy and jet direction in the simulation. To estimate the quality of the jet finding in data and Monte Carlo, events with two jets plus one isolated photon candidate selected as described in section 5.1 are used. The quality of the energy measurement is estimated as suggested in [64] by applying the relation

$$E^i_{recon} = E_{cm}\frac{\sin\alpha_{jl}}{\sum\sin\alpha_{mn}} \tag{5.13}$$

which is valid for three massless particles. E^i_{recon} is the energy of the jet i, and α_{jl} is the opposite angle between the other jet and the photon candidate. The sum goes over all three angles between the jets and the photon candidate. Equation 5.13 allows a determination of the jet energies rather independently of the energy resolution of the detector. The shift

$$\frac{\delta E}{E} = \frac{E_{meas} - E_{recon}}{E_{meas}} \tag{5.14}$$

has been calculated and compared between data and Monte Carlo with full detector simulation and as usual using JETSET as event generator. The distribution of the energy resolution as calculated in the Jade scheme with a value of $y_{cut} = 0.06$ as well as in the Durham scheme with a value of $y_{cut} = 0.01$ is displayed for data and Monte Carlo in the top row of figure 5.13.

The differences of the average shifts $< \delta E/E >_{data} - < \delta E/E >_{MC}$ vary between 0.026 ± 0.010 ($y_{cut} = 0.005$) and 0.0003 ± 0.004 ($y_{cut} = 0.08$) in the Jade scheme as well as 0.019 ± 0.006 ($y_{cut} = 0.004$) and 0.002 ± 0.004 ($y_{cut} = 0.04$) in the Durham scheme. Allowing an energy shift according to these numbers leads to a y_{cut}-dependent change of the calculated photon rate between 0.1% and 0.6% in the Jade case as well as between 0.1% and 0.2% in the Durham case.

The angular resolution of the jet direction is estimated as follows: the hadronic part of the event is boosted into its rest frame where the boost vector is given by the momentum and the recoil mass of the selected photon candidate,

$$M_{recoil} = \sqrt{(E_{cm} - E_{cl})^2 - E_{cl}^2} = E_{cm}\sqrt{1 - 2 \cdot E_{cl}/E_{cm}}. \tag{5.15}$$

Here, E_{cl} is the corrected energy of the photon candidate as defined by 5.3. In this system, the two jets should be colinear. The distributions of the acolinearity angle $\Delta\alpha$ between the boosted jets in data and Monte Carlo are shown in the bottom row of figure 5.13 for the y_{cut} values of 0.02 (Jade algorithm) and 0.006 (Durham algorithm). The mean values of these particular distributions are $7.08^o \pm 0.17^o$ in data and $8.00^o \pm 0.13^o$ in the simulation for Jade resp. $6.64^o \pm 0.17^o$ and $7.75^o \pm 0.14^o$ for Durham. A rescaling of the jet-to-photon candidate angle by $\pm\delta\alpha$, where $\delta\alpha = | < \Delta\alpha >_{data} - < \Delta\alpha >_{MC} |$, depending on the value of y_{cut}, to represent the mean deviations of the simulation from data results in a relative change of the photon efficiency between 0.1 and 1.5%.

The relative systematic uncertainties due to the photon conversion rate as simulated by the detector Monte Carlo, due to the misrepresentation of the jet energies and directions are summarised in table 5.11, together with the errors coming from Monte Carlo statistics. The listed contributions are combined in one error on the efficiency correction $c^{ISR+FSR}(y_{cut})$.

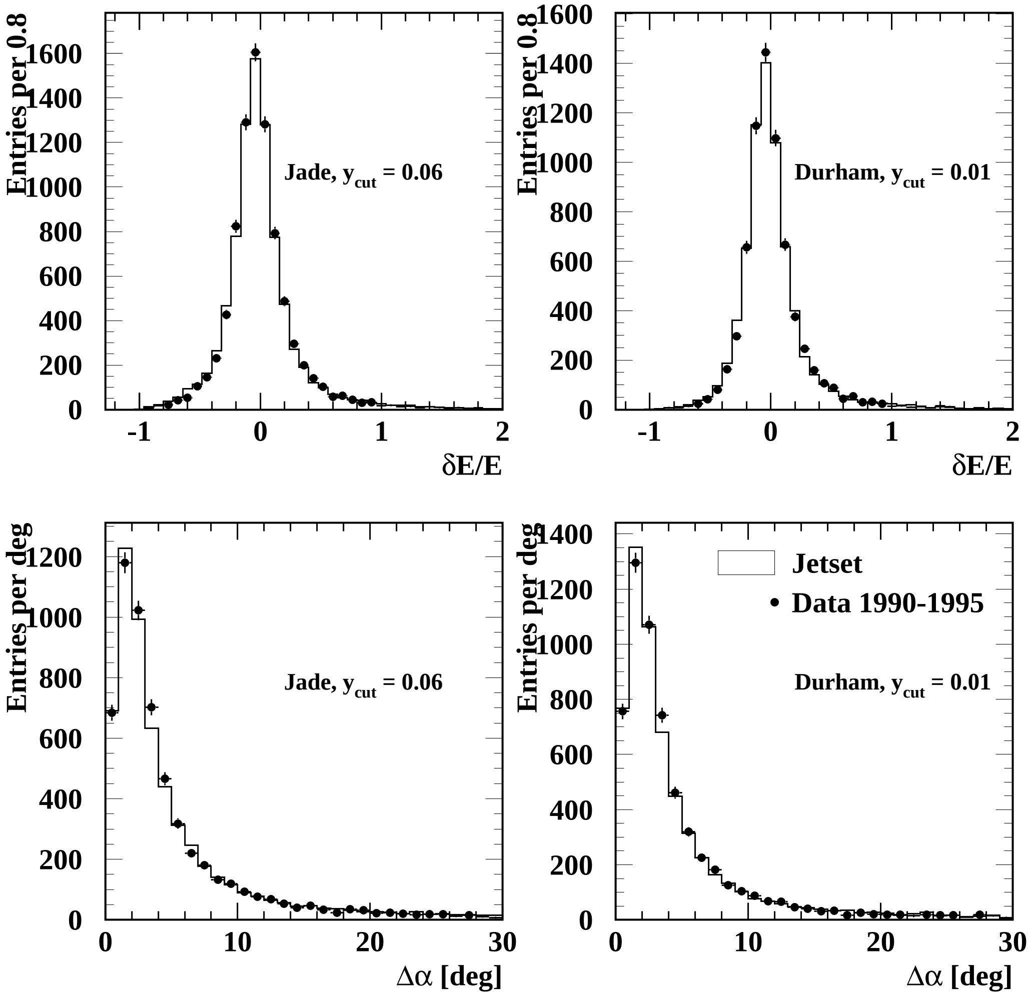

Figure 5.13: The top row shows the energy resolution of the reconstructed jets $\delta E/E$ in data and Monte Carlo for the two jet finder algorithms and some representative y_{cut} values. The bottom row shows the acolinearity angle of the jets from events with two jets plus one photon candidate, after they have been boosted into the hadronic rest system.

5.4.2.2 Uncertainties due to Deficiencies of the Event Generation (Uncertainties of $c^{FSR}(y_{cut})$)

Studies with Different Parton Shower Models

Here, the corrections $c^{FSR}(y_{cut})$ obtained with the JETSET model have been compared to those obtained with the HERWIG and ARIADNE model, which are described in section 2.3. The three models use different parton showering schemes, and moreover, in the HERWIG case a different fragmentation scheme is utilised. All Models are tuned in order to yield a good description of the global characteristics of hadronic Z^0 decays [93,101]. In table 5.12, the

Jade E0					Durham (k_t)				
y_{cut}	stat.	Conv.	Jet energy	Jet angle	y_{cut}	stat.	Conv.	Jet energy	Jet angle
0.005	±0.5	±0.7	±0.5	±1.2	0.002	±0.4	±0.7	±0.1	±1.2
0.01	±0.5	±0.7	±0.5	±1.5	0.004	±0.5	±0.7	±0.2	±1.4
0.02	±0.5	±0.7	±0.6	±1.3	0.006	±0.5	±0.7	±0.2	±1.3
0.04	±0.6	±0.7	±0.4	±1.1	0.008	±0.5	±0.7	±0.1	±1.1
0.06	±0.6	±0.7	±0.3	±1.1	0.01	±0.5	±0.7	±0.1	±1.1
0.08	±0.8	±0.7	±0.1	±0.9	0.012	±0.5	±0.7	±0.1	±1.1
0.1	±0.9	±0.7	±0.1	±0.9	0.014	±0.6	±0.7	±0.1	±1.1
0.12	±1.0	±0.8	±0.5	±0.7	0.016	±0.6	±0.7	±0.1	±1.1
0.14	±1.1	±0.8	±0.2	±0.4	0.02	±0.6	±0.7	±0.1	±1.1
0.16	±1.1	±0.8	±0.5	±0.3	0.04	±0.8	±0.8	±0.1	±0.6
0.18	±1.2	±0.8	±0.5	±0.1	0.06	±0.9	±0.8	±0.1	±0.4
0.2	±1.2	±0.8	±0.3	±0.2	0.1	±1.0	±0.8	±0.2	±0.1

Table 5.11: The relative systematic uncertainties of the correction factor $c^{ISR+FSR}(y_{cut})$, which are most significant (in %).

Jade E0				Durham (k_t)			
y_{cut}	stat.	HERWIG	ARIADNE	y_{cut}	stat	HERWIG	ARIADNE
0.005	±0.5	−11.2	−11.2	0.002	±0.5	−12.8	−12.0
0.01	±0.5	−7.2	−6.8	0.004	±0.5	−9.2	−8.9
0.02	±0.5	−4.1	−4.2	0.006	±0.5	−7.7	−7.4
0.04	±0.6	−1.7	−1.4	0.008	±0.5	−6.1	−5.7
0.06	±0.6	−1.2	−1.0	0.01	±0.5	−4.9	−4.8
0.08	±0.7	−0.9	0.1	0.012	±0.6	−4.3	−3.8
0.1	±0.8	−0.3	−0.1	0.014	±0.6	−3.8	−3.7
0.12	±0.9	−0.3	0.2	0.016	±0.6	−3.6	−3.0
0.14	±1.0	−1.6	−0.9	0.02	±0.6	−3.5	−2.8
0.16	±1.1	−4.2	−1.4	0.04	±0.7	−4.0	−2.1
0.18	±1.1	−5.8	−1.5	0.06	±0.9	−7.1	−2.8
0.2	±1.2	−7.4	−1.0	0.1	±1.0	−13.3	−6.2

Table 5.12: The relative deviations of the correction factors calculated with HERWIG or ARIADNE from the ones calculated with JETSET. For comparison, the relative statistical errors on the factors calculated with JETSET are also listed (in %).

relative deviations of HERWIG and ARIADNE from JETSET are compared to the relative statistical error on the correction factors calculated using JETSET. The available statistics for HERWIG and ARIADNE with 8 million generated hadronic Z^0 decays each is of about the same size as for JETSET.

The relative deviations are larger for lower and higher values of y_{cut} with a largest deviation of -13.3% (for HERWIG and the Durham algorithm). The deviations are small in the intermediate range of y_{cut} values for both jet finder schemes. The deviations stem from the different particle flow around the FSR photons in the three models. As a result, in the JETSET case more photons are rejected on hadron level than in the HERWIG or ARIADNE cases due to the cone isolation requirement. This effect is softened in regions of intermediate y_{cut} values, where the efficiency loss caused by the cone isolation criterion is smallest.

Studies with 'Differential' Correction Factors

The measured photon rates are correlated for different values of y_{cut}. Therefore, it is difficult to quantify the degree of agreement between the theoretical predictions of the matrix element calculation and the data. In [30], it was suggested to study the differential distribution of the photon rates, which is almost statistically independent for the different values of y_{cut}. Calculating the 'differential' correction factors for the three available parton shower models provides an additional systematic cross-check of the y_{cut}-dependent efficiency correction. The differential distribution is defined as

$$\begin{aligned} D_{FSR}(y_{cut}) &= \frac{1}{N_{MH}\delta}[N_{FSR}(y_{cut}-\delta/2) - N_{FSR}(y_{cut}+\delta/2)] \\ &= \frac{1}{N_{MH}\delta}[\sum_i N^{i\rightarrow reject} - \sum_i N^{reject\rightarrow i}], \end{aligned} \tag{5.16}$$

where N_{FSR} is the number of final state photon candidates, and N_{MH} is the number of hadronic Z^0 decays. $N^{i\rightarrow reject}$ is the number of events that have a jet multiplicity i at $y_{cut}-\delta/2$ but that are rejected at $y_{cut}+\delta/2$, whereas $N^{reject\rightarrow i}$ is the number of events that are rejected at $y_{cut}-\delta/2$ but are retained at $y_{cut}+\delta/2$ with a jet multiplicity i. The gains and losses for each i jet event class are statistically independent, so that the 'differential' correction factors,

$$c^{i\rightarrow reject} = \frac{N^{i\rightarrow reject}_{parton}}{N^{i\rightarrow reject}_{hadron}} \quad \text{and} \quad c^{reject\rightarrow i} = \frac{N^{reject\rightarrow i}_{parton}}{N^{reject\rightarrow i}_{hadron}} \tag{5.17}$$

are almost statically independent, too. The differences between the various parton shower models observed for these differential corrections are largest between HERWIG and JETSET and for small values of y_{cut}. They amount up to around 32% in the Jade case and up to around 27% in the Durham case. For $y_{cut} > 0.04$ in the Jade scheme, the differential correction factors agree within 10%. In the Durham scheme, they agree within 10% for $y_{cut} > 0.014$. The emerging deviations are also due to the cone isolation criterion.

The results obtained for the y_{cut}-dependent integral cross-sections calculated with the integral correction factors of tables 5.4 and 5.7 and calculated with the JETSET correction factors differentiated according to the the number of jets in an event agree within 2% (Jade scheme) and 5% (Durham scheme) for all values of y_{cut}.

Studies with the Isolation Cone

Finally the entire analysis has been repeated for different isolation cones, varying the isolation angle between 0.175 and 0.335 rad and allowing up to 0.5 GeV of additional energy deposition in the isolation cone. The largest deviations are observed for a cone half angle of 0.175 rad. For the Jade jet finder, they are below 4% for $y_{cut} \leq 0.1$ and have a peak value of 7.3% for $y_{cut} = 0.2$. The deviations calculated in the Durham scheme are larger, with the highest value of 7.8% at the largest $y_{cut} = 0.1$ and values of around and mostly below 5% for $y_{cut} \leq 0.04$.

Summary

Because the previous considerations are not independent, the estimate which gives the largest positive and the largest negative contribution to the systematic uncertainty for each y_{cut} scenario has been assigned as systematic error on $c^{FSR}(y_{cut})$. Four contributions corresponding to the performed studies have been compared:

- the size of the difference between the corrections from different QCD shower models,
- the size of the uncertainty of the losses due to the cone isolation requirement, where the relative untertainty has been chosen according to the relative differences between the differential corrections in the different QCD models,
- the size of the difference between the integral cross-sections calculated with the integral correction factors and with the correction factors differentiated according to the number of jets in the event,
- the size of the largest deviations in the photon rates if the analysis is repeated for various cone isolations.

The first two are observed as negative, the other two as positive systematic biases for all values of y_{cut}. The dominant contribution to the negative systematic error is given by the second one from the studies with the differential correction factors. Especially, for small values of y_{cut} this systematic uncertainty is much larger than the discrepancy between the integral correction factors, whereas at higher values of y_{cut} also the latter begins to play a role. The positive systematic error is merely due to the last item of the above list. For both jet finders and all values of y_{cut} the variation of the isolation criterion gives the largest systematic deviation. The outcome of the comparison defining the largest deviation as systematic error is listed in table 5.13 together with the correction itself and its error from Monte Carlo statistics.

5.5 Corrected Numbers of Events with an Isolated Photon

The completely background and efficiency corrected numbers of hadronic Z^0 decays with final state radiation normalised to 1000 hadronic Z^0 decays are summarised in this section. In addition to the total numbers, the numbers of FSR events with 1, 2, 3, and more than 3 jets are also measured and displayed in the following. The section concludes with a discussion containing a comparison of the measurement with predictions of the matrix element calculation which is introduced in chapter 2.

Jade E0		Durham (k_t)	
y_{cut}	Correction factors	y_{cut}	Correction factors
0.005	$1.71 \pm 0.02^{+0.06}_{-0.40}$	0.002	$1.78 \pm 0.01^{+0.10}_{-0.35}$
0.01	$1.59 \pm 0.01^{+0.06}_{-0.37}$	0.004	$1.65 \pm 0.01^{+0.08}_{-0.33}$
0.02	$1.51 \pm 0.01^{+0.05}_{-0.22}$	0.006	$1.60 \pm 0.01^{+0.07}_{-0.28}$
0.04	$1.45 \pm 0.01^{+0.05}_{-0.14}$	0.008	$1.56 \pm 0.01^{+0.06}_{-0.23}$
0.06	$1.43 \pm 0.01^{+0.05}_{-0.11}$	0.01	$1.54 \pm 0.01^{+0.06}_{-0.19}$
0.08	$1.43 \pm 0.01^{+0.05}_{-0.03}$	0.012	$1.52 \pm 0.01^{+0.06}_{-0.19}$
0.1	$1.44 \pm 0.01^{+0.06}_{-0.08}$	0.014	$1.52 \pm 0.01^{+0.06}_{-0.13}$
0.12	$1.46 \pm 0.01^{+0.07}_{-0.02}$	0.016	$1.51 \pm 0.01^{+0.07}_{-0.12}$
0.14	$1.49 \pm 0.01^{+0.07}_{-0.05}$	0.02	$1.51 \pm 0.01^{+0.07}_{-0.11}$
0.16	$1.53 \pm 0.02^{+0.04}_{-0.08}$	0.04	$1.54 \pm 0.01^{+0.09}_{-0.07}$
0.18	$1.56 \pm 0.02^{+0.06}_{-0.09}$	0.06	$1.62 \pm 0.01^{+0.11}_{-0.12}$
0.2	$1.61 \pm 0.02^{+0.12}_{-0.12}$	0.1	$1.82 \pm 0.02^{+0.14}_{-0.24}$

Table 5.13: The correction factors $c_{FSR}(y_{cut})$ with their error contributions due to Monte Carlo statistics and estimated from the described systematic studies.

5.5.1 The Total Number

The total number of events with final state photons normalised to 1000 multihadronic Z^0 decays,

$$R_{Z^0 \to (n\text{Jets}+\gamma)}(y_{cut}) \times 1000 = \frac{N_{Z^0 \to (n\text{Jets}+\gamma)}(y_{cut})}{N_{Z^0 \to \text{Hadrons}}} \times 1000 = \mathrm{R}_{FSR}(y_{cut})$$

for the Jade and the Durham scheme are listed in table 5.14. The error contributions in order of appearance are from the data stastics, from the hadronic background estimation, from the ISR estimation, from the efficiency correction $c^{ISR+FSR}(y_{cut})$, and from the efficiency correction $c^{FSR}(y_{cut})$. As can be seen, in general the largest uncertainty comes from $c^{FSR}(y_{cut})$, which corrects for hadronisation effects, for the polar angle cut of $|\cos\theta| \leq 0.72$, and the isolation cone around the photon. The uncertainty is mainly caused by the isolation requirement as the previous systematic studies comparing various parton shower models have shown. The second largest contribution is due to the uncertainty of the hadronic background estimation. Here, a significant error source is insufficiently modelled hadronic background, the possible influence of which has been estimated using reweighted hadronic cluster samples as well as hadronic samples selected from HERWIG.

Potential correlations between $c^{ISR+FSR}(y_{cut})$ and f_γ have been investigated, since their determination is done with the same Monte Carlo sample of 8.4 million hadronic Z^0 decays generated with JETSET. Studies performed with various subsamples have not detected any correlation between $c^{ISR+FSR}(y_{cut})$ and f_γ, so that these are treated as uncorrelated when calculating the total error.

The numbers of the FSR yields in the matrix element Monte Carlo GNJETS and the parton shower model Monte Carlos JETSET, HERWIG, and ARIADNE, which are tuned to describe the global event shapes, are also listed in table 5.14. The agreement between GNJETS and

Jade E0

y_{cut}	Data	ME	JETSET	HERWIG	ARIADNE
0.005	$4.23 \pm 0.05^{+0.03}_{-0.12} \pm 0.005 \pm 0.07^{+0.16}_{-0.99}$		3.33 ± 0.02	4.11 ± 0.02	4.74 ± 0.03
0.01	$3.54 \pm 0.04^{+0.03}_{-0.16} \pm 0.005 \pm 0.06^{+0.14}_{-0.83}$		2.87 ± 0.02	3.48 ± 0.02	4.07 ± 0.02
0.02	$2.91 \pm 0.04^{+0.07}_{-0.08} \pm 0.004 \pm 0.05^{+0.10}_{-0.42}$	$2.87^{+0.11}_{-0.14}$	2.40 ± 0.02	2.85 ± 0.02	3.37 ± 0.02
0.04	$2.26 \pm 0.04^{+0.09}_{-0.03} \pm 0.004 \pm 0.04^{+0.07}_{-0.22}$	$2.28^{+0.06}_{-0.07}$	1.88 ± 0.01	2.20 ± 0.02	2.64 ± 0.02
0.06	$1.82 \pm 0.03^{+0.03}_{-0.05} \pm 0.003 \pm 0.03^{+0.06}_{-0.14}$	$1.89^{+0.03}_{-0.04}$	1.52 ± 0.01	1.77 ± 0.01	2.15 ± 0.02
0.08	$1.50 \pm 0.03^{+0.08}_{-0.03} \pm 0.003 \pm 0.03^{+0.06}_{-0.04}$	$1.51^{+0.02}_{-0.02}$	1.23 ± 0.01	1.42 ± 0.01	1.76 ± 0.02
0.1	$1.25 \pm 0.03^{+0.11}_{-0.03} \pm 0.003 \pm 0.02^{+0.05}_{-0.07}$	$1.22^{+0.01}_{-0.02}$	1.01 ± 0.01	1.16 ± 0.01	1.45 ± 0.01
0.12	$1.05 \pm 0.03^{+0.04}_{-0.03} \pm 0.002 \pm 0.02^{+0.05}_{-0.02}$	$1.03^{+0.01}_{-0.02}$	0.85 ± 0.01	0.98 ± 0.01	1.25 ± 0.01
0.14	$0.91 \pm 0.03^{+0.04}_{-0.02} \pm 0.002 \pm 0.02^{+0.04}_{-0.03}$	$0.92^{+0.03}_{-0.03}$	0.73 ± 0.01	0.85 ± 0.01	1.09 ± 0.01
0.16	$0.81 \pm 0.03^{+0.02}_{-0.05} \pm 0.002 \pm 0.02^{+0.02}_{-0.04}$	$0.83^{+0.03}_{-0.03}$	0.66 ± 0.01	0.75 ± 0.01	0.99 ± 0.01
0.18	$0.74 \pm 0.04^{+0.09}_{-0.5} \pm 0.002 \pm 0.01^{+0.03}_{-0.04}$	$0.76^{+0.03}_{-0.04}$	0.60 ± 0.01	0.68 ± 0.01	0.92 ± 0.01
0.2	$0.69 \pm 0.03^{+0.10}_{-0.04} \pm 0.002 \pm 0.01^{+0.05}_{-0.05}$	$0.73^{+0.04}_{-0.05}$	0.58 ± 0.01	0.63 ± 0.01	0.89 ± 0.01

Durham

y_{cut}	Data	ME	JETSET	HERWIG	ARIADNE
0.002	$4.51 \pm 0.05^{+0.03}_{-0.33} \pm 0.006 \pm 0.07^{+0.24}_{-0.89}$		3.58 ± 0.02	4.45 ± 0.02	5.11 ± 0.03
0.004	$3.87 \pm 0.05^{+0.03}_{-0.20} \pm 0.005 \pm 0.06^{+0.19}_{-0.77}$		3.10 ± 0.02	3.81 ± 0.02	4.42 ± 0.03
0.006	$3.46 \pm 0.05^{+0.03}_{-0.12} \pm 0.005 \pm 0.05^{+0.16}_{-0.60}$	$3.46^{+0.09}_{-0.12}$	2.80 ± 0.02	3.39 ± 0.02	3.97 ± 0.02
0.008	$3.18 \pm 0.04^{+0.08}_{-0.05} \pm 0.005 \pm 0.04^{+0.12}_{-0.46}$	$3.15^{+0.08}_{-0.10}$	2.55 ± 0.02	3.08 ± 0.02	3.65 ± 0.02
0.01	$2.92 \pm 0.04^{+0.06}_{-0.04} \pm 0.004 \pm 0.04^{+0.12}_{-0.37}$	$2.87^{+0.07}_{-0.09}$	2.37 ± 0.02	2.83 ± 0.02	3.37 ± 0.02
0.012	$2.74 \pm 0.04^{+0.05}_{-0.05} \pm 0.004 \pm 0.04^{+0.11}_{-0.34}$	$2.69^{+0.06}_{-0.08}$	2.20 ± 0.02	2.60 ± 0.02	3.13 ± 0.02
0.014	$2.53 \pm 0.04^{+0.07}_{-0.06} \pm 0.004 \pm 0.04^{+0.11}_{-0.22}$	$2.51^{+0.06}_{-0.08}$	2.06 ± 0.02	2.43 ± 0.02	2.92 ± 0.02
0.016	$2.38 \pm 0.04^{+0.06}_{-0.05} \pm 0.004 \pm 0.03^{+0.10}_{-0.19}$	$2.37^{+0.05}_{-0.07}$	1.94 ± 0.02	2.27 ± 0.02	2.75 ± 0.02
0.02	$2.14 \pm 0.04^{+0.10}_{-0.04} \pm 0.003 \pm 0.02^{+0.10}_{-0.16}$	$2.15^{+0.04}_{-0.06}$	1.74 ± 0.01	2.02 ± 0.02	2.49 ± 0.02
0.04	$1.52 \pm 0.04^{+0.10}_{-0.04} \pm 0.003 \pm 0.02^{+0.09}_{-0.07}$	$1.59^{+0.04}_{-0.05}$	1.27 ± 0.01	1.43 ± 0.01	1.84 ± 0.02
0.06	$1.30 \pm 0.04^{+0.09}_{-0.05} \pm 0.003 \pm 0.02^{+0.09}_{-0.09}$	$1.35^{+0.03}_{-0.05}$	1.10 ± 0.01	1.19 ± 0.01	1.60 ± 0.02
0.1	$1.20 \pm 0.04^{+0.09}_{-0.04} \pm 0.003 \pm 0.02^{+0.10}_{-0.16}$	$1.30^{+0.04}_{-0.06}$	1.00 ± 0.01	1.04 ± 0.01	1.47 ± 0.01

Table 5.14: The background and efficiency corrected numbers of events with isolated final state photons per 1000 multihadonic Z^0 decays. The prediction of the $\mathcal{O}(\alpha\alpha_s^{(1)})$ matrix element (ME) Monte Carlo for $\alpha_s^{(1)} = 0.18$ is also listed, as well as the FSR yield in the three considered parton shower models of JETSET, HERWIG, and ARIADNE. The different error contributions to the measurement in order of appearance are from the data stastics, from the hadronic background estimation, from the ISR estimation, from the efficiency correction $c^{ISR+FSR}(y_{cut})$, and from the efficiency correction $c^{FSR}(y_{cut})$. The errors of the ME based predictions are due to a variation of $\alpha_s^{(1)}$ and of the phase space cut-off in the perturbative calculations, whereas the errors of the photon yields in the parton shower model are merely statistical.

data is very good. In contrast, as expected from other measurements [30,31,57–59], which are mentioned at the end of section 2.3.1.4, the FSR yield of JETSET is globally smaller than the yield measured in data.

The distribution of the measured total FSR photon numbers normalised to 1000 multihadronic Z^0 decays depending on the value of y_{cut} is shown in figure 5.14 together with the range of the matrix element predictions using various values for $\alpha_s^{(1)}$ $(0.15 - 0.22)$ and for the theoretical cut-off parameter y_γ $(0.0005 - 0.001)$. These parameter ranges have been fixed adopting suggestions in previous publications ([30, 44, 114]) and results for $\alpha_s^{(1)}$ derived from a fit to the jet rates in the inclusive sample of hadronic Z^0 decays ([115]). The lowest two values of y_{cut} in both jet finder schemes are not considered for the matrix element calculation, because it is not able to describe final states containing more than three partons, whereas in data the contribution to the total number from FSR events with more than three jets is large. As can be seen for both jet finder algorithms, the measurement errors in the intermediate y_{cut} range are smaller than in the regions of small and large y_{cut} values. In these regions, the result is in particular sensitive to the isolation cone requirement causing an efficiency loss, which can only be estimated with Monte Carlo generators. The large error asymmetry visible there is also caused by the systematic uncertainty of $c^{FSR}(y_{cut})$, which has been discussed in section 5.4.2.2.

5.5.2 The 1, 2, and 3 Jet Numbers

The numbers of events containing an isolated, highly energetic final state photon measured separately for 1, 2, 3, and more than 3 jets in the event are listed in the tables 5.15 (Jade E0 algorithm) and 5.16 (Durham algorithm). The numbers are again normalised to 1000 multihadronic events, and the separate error contributions are given in the same order as for the measured total number in the last section. The estimation of the ISR background, and the determination of the efficiency corrections $c^{ISR+FSR}(y_{cut})$, and $c^{FSR}(y_{cut})$, as well as the related systematic studies have been repeated separately for each jet multiplicity. However, for lack of statistics this is not possible for the hadronic background estimation. The number of selected events with 1 jet is too small for low values of y_{cut}, the number of events with 3, and more than 3 jets is too small for high values of y_{cut}. This in particular affects the hadronic background distributions of C (in eight separate energy bins), where the statistics is getting very low. As a consequence, the binned maximum likelihood fit does not deliver reliable results. Therefore, the estimation of the hadronic background contribution for the n jet events $(n = 1, 2, 3, > 3)$ has been extrapolated from the fit results in the overall FSR sample, taking into account particular weights for each energy bin according to the statistics of n jet events in this bin. The related relative systematic uncertainties of the fitted true photon fraction f_γ are taken accordingly from the studies with the overall sample. The proportions of the diverse error contributions are similar to those of the results obtained in the overall sample with the uncertainties due to the efficiency corrections $c^{FSR}(y_{cut})$ and due to the hadronic background estimation being largest.

The distributions of the normalised number of events depending on the values of y_{cut} for events with 1, 2 and 3 jets are displayed in figure 5.15. The matrix element (ME) predictions for those event topologies are also indicated, again as bands of widths, which are fixed by the photon yield for various values of $\alpha_s^{(1)}$ and y_γ (cf. last section).

	Jade E0	
y_{cut}	1 Jet	2 Jet
0.005		$0.99 \pm 0.01^{+0.01}_{-0.03} \pm 0.003 \pm 0.02^{+0.01}_{-0.20}$
0.01	$0.01 \pm 0.000^{+0.000}_{-0.001} \pm 0.000 \pm 0.001^{+0.001}_{-0.001}$	$1.46 \pm 0.02^{+0.01}_{-0.07} \pm 0.003 \pm 0.02^{+0.01}_{-0.29}$
0.02	$0.02 \pm 0.001^{+0.001}_{-0.001} \pm 0.001 \pm 0.001^{+0.001}_{-0.002}$	$1.83 \pm 0.03^{+0.04}_{-0.05} \pm 0.003 \pm 0.02^{+0.01}_{-0.65}$
0.04	$0.05 \pm 0.001^{+0.003}_{-0.001} \pm 0.001 \pm 0.002^{+0.002}_{-0.002}$	$1.83 \pm 0.03^{+0.07}_{-0.03} \pm 0.003 \pm 0.02^{+0.01}_{-0.22}$
0.06	$0.08 \pm 0.002^{+0.002}_{-0.003} \pm 0.001 \pm 0.003^{+0.01}_{-0.003}$	$1.59 \pm 0.03^{+0.02}_{-0.04} \pm 0.003 \pm 0.02^{+0.01}_{-0.18}$
0.08	$0.13 \pm 0.003^{+0.01}_{-0.003} \pm 0.001 \pm 0.004^{+0.01}_{-0.01}$	$1.30 \pm 0.03^{+0.07}_{-0.03} \pm 0.003 \pm 0.02^{+0.01}_{-0.05}$
0.1	$0.17 \pm 0.005^{+0.02}_{-0.005} \pm 0.001 \pm 0.004^{+0.004}_{-0.03}$	$1.03 \pm 0.02^{+0.09}_{-0.03} \pm 0.002 \pm 0.01^{+0.01}_{-0.09}$
0.12	$0.22 \pm 0.006^{+0.01}_{-0.01} \pm 0.001 \pm 0.005^{+0.02}_{-0.02}$	$0.70 \pm 0.02^{+0.03}_{-0.02} \pm 0.002 \pm 0.01^{+0.04}_{-0.01}$
0.14	$0.27 \pm 0.009^{+0.01}_{-0.01} \pm 0.002 \pm 0.005^{+0.005}_{-0.06}$	$0.57 \pm 0.02^{+0.03}_{-0.02} \pm 0.002 \pm 0.01^{+0.01}_{-0.01}$
0.16	$0.32 \pm 0.01^{+0.01}_{-0.02} \pm 0.002 \pm 0.006^{+0.01}_{-0.03}$	$0.46 \pm 0.02^{+0.01}_{-0.03} \pm 0.001 \pm 0.01^{+0.01}_{-0.02}$
0.18	$0.39 \pm 0.02^{+0.04}_{-0.03} \pm 0.002 \pm 0.007^{+0.01}_{-0.04}$	$0.32 \pm 0.02^{+0.04}_{-0.02} \pm 0.001 \pm 0.01^{+0.02}_{-0.01}$
0.20	$0.44 \pm 0.02^{+0.07}_{-0.02} \pm 0.002 \pm 0.008^{+0.01}_{-0.05}$	$0.22 \pm 0.01^{+0.03}_{-0.01} \pm 0.001 \pm 0.01^{+0.004}_{-0.01}$

y_{cut}	3 Jet	> 3 Jet
0.005	$1.81 \pm 0.02^{+0.01}_{-0.05} \pm 0.003 \pm 0.03^{+0.02}_{-0.37}$	$1.50 \pm 0.01^{+0.01}_{-0.04} \pm 0.003 \pm 0.03^{+0.01}_{-0.41}$
0.01	$1.50 \pm 0.02^{+0.01}_{-0.07} \pm 0.003 \pm 0.03^{+0.01}_{-0.31}$	$0.70 \pm 0.01^{+0.004}_{-0.03} \pm 0.002 \pm 0.01^{+0.01}_{-0.19}$
0.02	$0.86 \pm 0.01^{+0.02}_{-0.02} \pm 0.002 \pm 0.02^{+0.01}_{-0.12}$	$0.31 \pm 0.003^{+0.01}_{-0.01} \pm 0.000 \pm 0.01^{+0.01}_{-0.05}$
0.04	$0.29 \pm 0.004^{+0.01}_{-0.004} \pm 0.001 \pm 0.01^{+0.01}_{-0.03}$	$0.03 \pm 0.002^{+0.004}_{-0.001} \pm 0.000 \pm 0.004^{+0.003}_{-0.004}$
0.06	$0.08 \pm 0.001^{+0.001}_{-0.002} \pm 0.001 \pm 0.01^{+0.004}_{-0.01}$	-
0.08	$0.02 \pm 0.000^{+0.001}_{-0.000} \pm 0.000 \pm 0.003^{+0.005}_{-0.002}$	-
0.1	$0.005 \pm 0.000^{+0.000}_{-0.000} \pm 0.000 \pm 0.002^{+0.001}_{-0.002}$	-
0.12	-	-
0.14	-	-
0.16	-	-
0.18	-	-
0.20	-	-

Table 5.15: The background and efficiency corrected numbers of events with isolated final state photons per 1000 multihadron events in the Jade E0 scheme listed separately according to the jet multiplicity in the event. The error contributions are given in the same order as for the total number. If the number of events are per 1000 multihadronic decays is below 0.005, it is not quoted.

	Durham	
y_{cut}	1 Jet	2 Jet
0.002	$0.02 \pm 0.000^{+0.000}_{-0.003} \pm 0.000 \pm 0.002^{+0.003}_{-0.002}$	$1.60 \pm 0.02^{+0.01}_{-0.12} \pm 0.003 \pm 0.02^{+0.01}_{-0.32}$
0.004	$0.04 \pm 0.001^{+0.000}_{-0.003} \pm 0.001 \pm 0.003^{+0.005}_{-0.002}$	$1.95 \pm 0.02^{+0.02}_{-0.10} \pm 0.003 \pm 0.03^{+0.01}_{-0.39}$
0.006	$0.07 \pm 0.001^{+0.001}_{-0.003} \pm 0.001 \pm 0.004^{+0.003}_{-0.004}$	$2.05 \pm 0.03^{+0.02}_{-0.08} \pm 0.003 \pm 0.03^{+0.01}_{-0.73}$
0.008	$0.08 \pm 0.001^{+0.002}_{-0.001} \pm 0.001 \pm 0.004^{+0.003}_{-0.003}$	$2.05 \pm 0.03^{+0.06}_{-0.03} \pm 0.003 \pm 0.03^{+0.01}_{-0.24}$
0.01	$0.11 \pm 0.002^{+0.003}_{-0.002} \pm 0.001 \pm 0.005^{+0.01}_{-0.005}$	$1.97 \pm 0.03^{+0.04}_{-0.03} \pm 0.003 \pm 0.03^{+0.01}_{-0.22}$
0.012	$0.14 \pm 0.002^{+0.003}_{-0.003} \pm 0.001 \pm 0.005^{+0.01}_{-0.01}$	$1.93 \pm 0.03^{+0.04}_{-0.03} \pm 0.003 \pm 0.03^{+0.01}_{-0.08}$
0.014	$0.15 \pm 0.002^{+0.004}_{-0.004} \pm 0.001 \pm 0.01^{+0.005}_{-0.03}$	$1.83 \pm 0.03^{+0.05}_{-0.05} \pm 0.003 \pm 0.02^{+0.01}_{-0.16}$
0.016	$0.18 \pm 0.003^{+0.004}_{-0.004} \pm 0.001 \pm 0.01^{+0.02}_{-0.02}$	$1.75 \pm 0.03^{+0.05}_{-0.04} \pm 0.003 \pm 0.02^{+0.11}_{-0.01}$
0.02	$0.21 \pm 0.003^{+0.01}_{-0.004} \pm 0.001 \pm 0.01^{+0.01}_{-0.05}$	$1.59 \pm 0.03^{+0.07}_{-0.03} \pm 0.003 \pm 0.02^{+0.01}_{-0.03}$
0.04	$0.37 \pm 0.01^{+0.02}_{-0.01} \pm 0.002 \pm 0.01^{+0.01}_{-0.04}$	$1.06 \pm 0.03^{+0.07}_{-0.03} \pm 0.002 \pm 0.02^{+0.01}_{-0.04}$
0.06	$0.51 \pm 0.01^{+0.03}_{-0.02} \pm 0.002 \pm 0.01^{+0.01}_{-0.05}$	$0.71 \pm 0.02^{+0.05}_{-0.03} \pm 0.002 \pm 0.01^{+0.04}_{-0.02}$
0.1	$0.72 \pm 0.02^{+0.05}_{-0.02} \pm 0.003 \pm 0.01^{+0.01}_{-0.07}$	$0.43 \pm 0.02^{+0.04}_{-0.02} \pm 0.001 \pm 0.01^{+0.01}_{-0.01}$
y_{cut}	3 Jet	$>$ 3 Jet
0.002	$1.56 \pm 0.02^{+0.01}_{-0.11} \pm 0.003 \pm 0.03^{+0.01}_{-0.32}$	$1.35 \pm 0.01^{+0.01}_{-0.09} \pm 0.003 \pm 0.02^{+0.01}_{-0.35}$
0.004	$1.25 \pm 0.01^{+0.01}_{-0.06} \pm 0.003 \pm 0.03^{+0.01}_{-0.25}$	$0.70 \pm 0.01^{+0.004}_{-0.03} \pm 0.002 \pm 0.01^{+0.01}_{-0.16}$
0.006	$0.96 \pm 0.01^{+0.01}_{-0.03} \pm 0.003 \pm 0.02^{+0.01}_{-0.13}$	$0.47 \pm 0.005^{+0.003}_{-0.01} \pm 0.001 \pm 0.01^{+0.01}_{-0.10}$
0.008	$0.78 \pm 0.01^{+0.02}_{-0.01} \pm 0.002 \pm 0.02^{+0.01}_{-0.07}$	$0.38 \pm 0.004^{+0.01}_{-0.004} \pm 0.001 \pm 0.01^{+0.01}_{-0.11}$
0.01	$0.66 \pm 0.01^{+0.01}_{-0.01} \pm 0.002 \pm 0.02^{+0.01}_{-0.10}$	$0.26 \pm 0.002^{+0.004}_{-0.003} \pm 0.001 \pm 0.01^{+0.01}_{-0.10}$
0.012	$0.53 \pm 0.01^{+0.01}_{-0.01} \pm 0.002 \pm 0.01^{+0.12}_{-0.02}$	$0.21 \pm 0.002^{+0.003}_{-0.002} \pm 0.000 \pm 0.01^{+0.01}_{-0.04}$
0.014	$0.43 \pm 0.01^{+0.01}_{-0.01} \pm 0.002 \pm 0.01^{+0.01}_{-0.14}$	$0.17 \pm 0.002^{+0.003}_{-0.003} \pm 0.000 \pm 0.01^{+0.004}_{-0.03}$
0.016	$0.35 \pm 0.01^{+0.01}_{-0.01} \pm 0.002 \pm 0.01^{+0.05}_{-0.03}$	$0.14 \pm 0.002^{+0.003}_{-0.002} \pm 0.000 \pm 0.005^{+0.003}_{-0.01}$
0.02	$0.26 \pm 0.004^{+0.01}_{-0.005} \pm 0.001 \pm 0.01^{+0.01}_{-0.01}$	$0.15 \pm 0.001^{+0.003}_{-0.001} \pm 0.000 \pm 0.01^{+0.004}_{-0.08}$
0.04	$0.05 \pm 0.001^{+0.003}_{-0.001} \pm 0.000 \pm 0.004^{+0.003}_{-0.003}$	-
0.06	$0.007 \pm 0.000^{+0.000}_{-0.000} \pm 0.000 \pm 0.001^{+0.001}_{-0.001}$	-
0.1	-	-

Table 5.16: The background and efficiency corrected numbers of events with isolated final state photons per 1000 multihadron events in the Durham scheme listed separately according to the jet multiplicity in the event. The error contributions are given in the same order as for the total number. If the number of events are per 1000 multihadronic decays is below 0.005, it is not quoted.

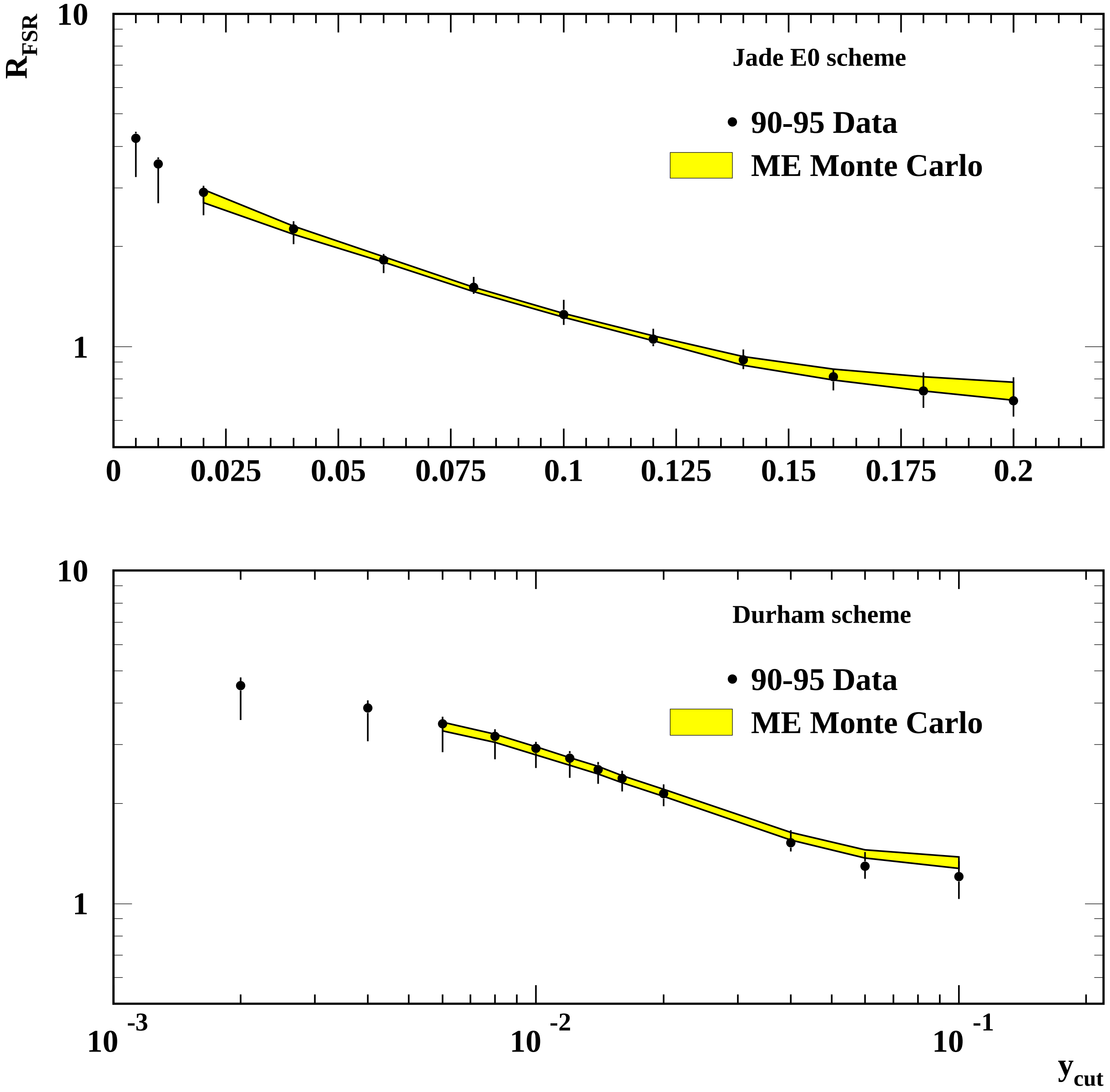

Figure 5.14: The total number of events with FSR per 1000 multihadron events in two jet finder schemes and for twelve values of y_{cut}. The prediction of the $\mathcal{O}(\alpha\alpha_s^{(1)})$ matrix element Monte Carlo is also shown. The band width of the theoretical prediction is a result of a variation of $\alpha_s^{(1)}$ and of the phase space cut-off in the perturbative calculations.

In general, the agreement between ME prediction and measurement is very good for the total, and reasonable for the n-jet rate of events with isolated final state photons. This applies for both jet finders.

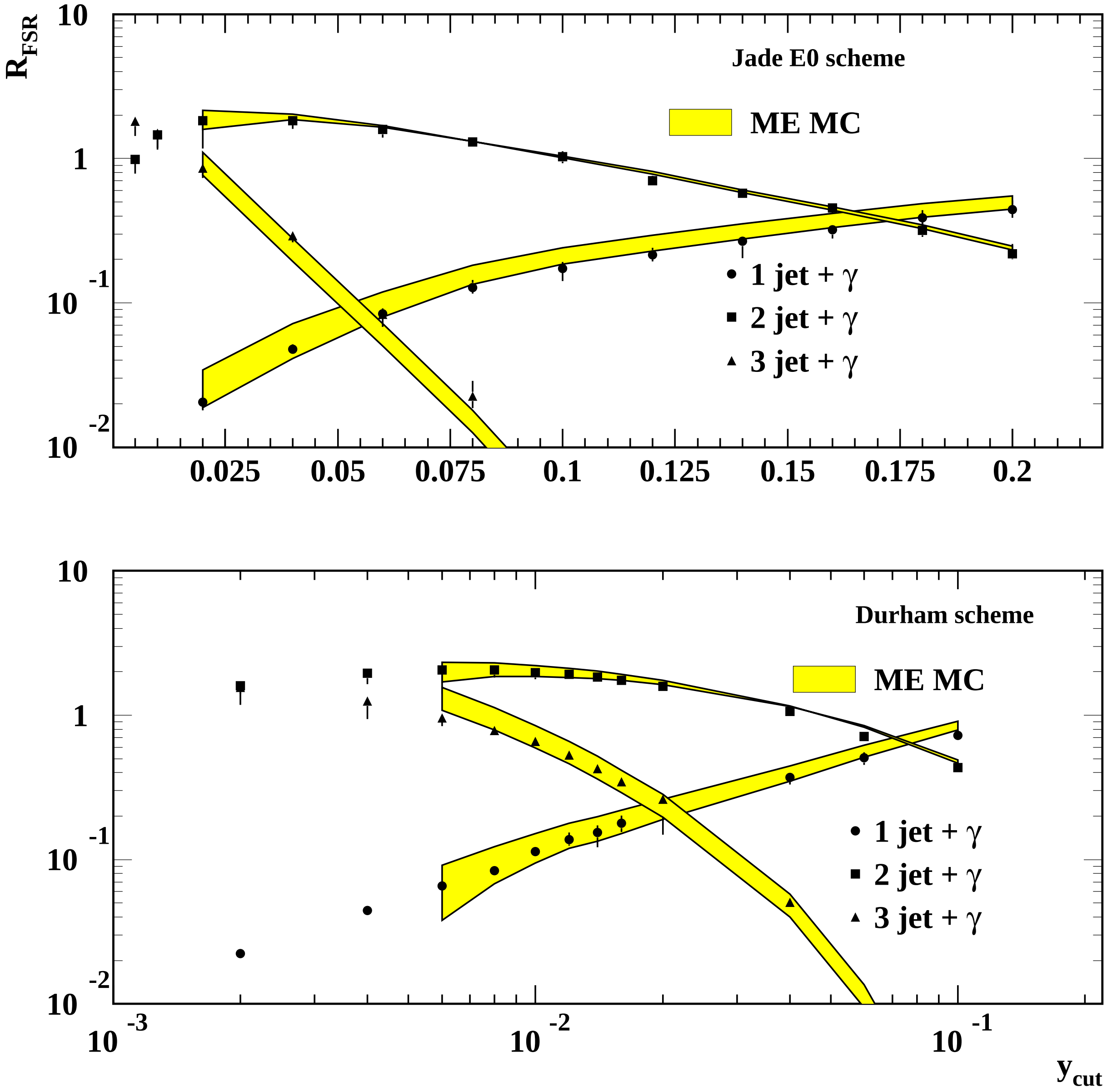

Figure 5.15: The number of events with FSR per 1000 multihadron events in two Jet finder schemes and for twelve values of y_{cut} depicted separately for 1, 2, and 3 jets in the event. The prediction of the $\mathcal{O}(\alpha\alpha_s^{(1)})$ ME Monte Carlo is also shown. The band width of the theoretical prediction is derived as has been described earlier.

In the following, the comparison between measurement and theoretical prediction will be discussed in more detail.

5.5.3 Discussion of the Measured Photon Numbers and Comparison with Matrix Element Predictions

As expected, in figure 5.14 for both, data and ME Monte Carlo, a decrease of the photon rate with increasing y_{cut} is observed for the two recombination schemes. At the lowest considered value of y_{cut} the 3-jet+γ rate dominates (Jade E0) or is at least almost equal to the 2-jet+γ rate (Durham). The 3-jet+γ rate is steeply falling with increasing y_{cut} values in both jet finder schemes, whereas the 1-jet+γ rate is rising steadily, but not as fast. The 2-jet+γ rate also decreases, so that at the largest two y_{cut} values in the Jade and at the largest y_{cut} value in the Durham scheme the 1-jet+γ rate dominates over the 2-jet+γ rate.

As pointed out earlier, the uncertainties of the measurement of the total rate are smallest for the intermediate range of y_{cut} values. This is true as well for the uncertainties of the theoretical calculation. In figure 5.16, the ratio of the total photon yield as predicted by the ME Monte Carlo over the measured photon yield is shown as function of y_{cut}. The error bars in the plots represent the relative experimental error, the lines are the results of the ratio for different Monte Carlo input values of $\alpha_s^{(1)}$ (0.15, 0.18, 0.22). The larger the value for $\alpha_s^{(1)}$ in the ME calculation is chosen, the smaller is the predicted photon rate. This is because gluon emission, the cross-section of which is proportional to $\alpha_s^{(1)}$, diminishes the available phase space for photon emission. For the considered values of $\alpha_s^{(1)}$, the obtained ME results agree with the measurement well within the errors over the whole range of y_{cut} values, except for very large values of y_{cut} in the Durham scheme, where an excess of photons is observed in the ME Monte Carlo relative to the data. However, the size of the deviation is hardly greater than one sigma. It has to be kept in mind, that the ratios are highly correlated for the different y_{cut} values.

The dependence of the individual n-jet+γ yields on $\alpha_s^{(1)}$ is larger than that of the total cross-section. In figure 5.17, the ratios of the 1-, 2-, and 3-jet+γ rates as predicted by the ME Monte Carlo over the measured photon yield are display as functions of y_{cut}. Like in figure 5.16, the relative experimental errors are represented by the error bars, the resulting ratios for $\alpha_s^{(1)} = 0.15, 0.18$, and 0.22 are indicated as lines of different gray scales. Since the cross-section for gluon radiation from either a quark or antiquark is proportional to α_s, the 3-jet+γ rates predicted by GNJETS for the two considered jet finder algorithms increase with increasing values of $\alpha_s^{(1)}$. In contrast to the 3-jet+γ rates, the 1-jet+γ (over the full y_{cut} range) and the 2-jet+γ rates (for small values of y_{cut}) decrease as a function of increasing $\alpha_s^{(1)}$. The sensitivity of the 1-jet+γ can be explained if one considers the case of hard photon radiation off a soft quark. The quark pair in such an event may be combined in one single jets. However, additional gluon emission by one of the quarks increases the invariant mass of the hadronic part of this event. As a result, it is more probable that its hadronic system is combined in two jets instead of one, and thus the event does not appear in the 1-jet+γ record. The decreasing 2-jet+γ for small values of y_{cut} with increasing α_s can be understood similarly. Increasing gluon radiation leads to more events being recombined into 3 jets, which might be either assigned to the 3-jet+γ rate or rejected at all by the requirement $y_{jet\gamma} < y_{cut}$. But in this regard, it should be stressed, that the α_s dependence of the 2-jet+γ rate is much weaker than that of the other two individual rates. This applies in particular to the intermediate y_{cut} range of the Jade, and the upper y_{cut} range of Durham recombination scheme. From the above considerations it can be concluded, that the α_s sensitivities of the n-jet+γ rates cancel each other at least partially, so that the α_s

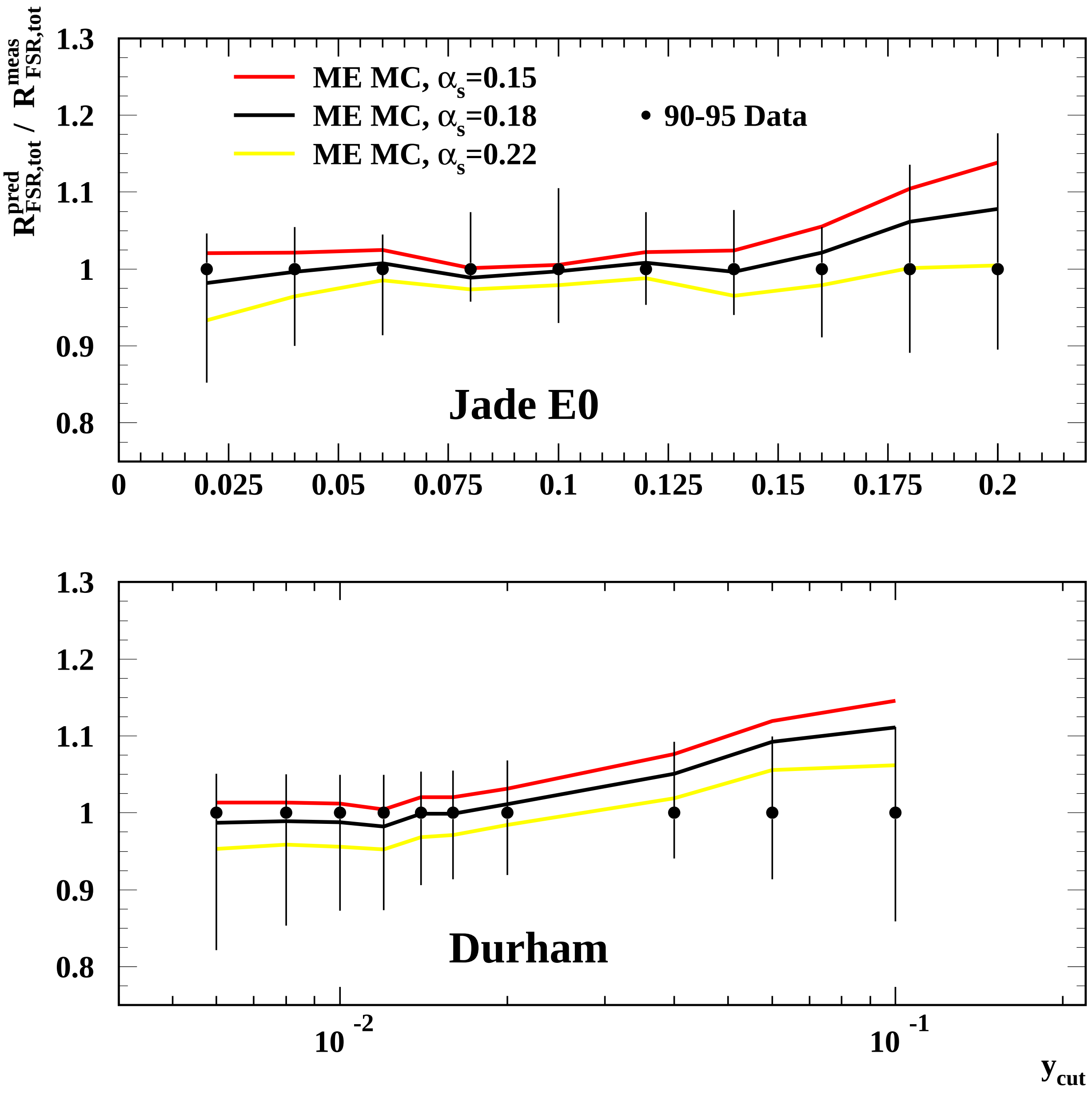

Figure 5.16: Prediction-to-measurement ratio of the total FSR yield in hadronic Z^0 decays as a function of y_{cut} in the two jet finder schemes. The prediction is again calculated with the Monte Carlo GNJETS, which includes matrix elements up to $\mathcal{O}(\alpha\alpha_s)$. The lines denote the ME results for three different values of $\alpha_s^{(1)}$. The error bars on the data give the relative experimental error.

dependence of the total cross-section is weaker than for the individual rates.

The 1-jet+γ rate is overestimated by the $\mathcal{O}(\alpha\alpha_s^{(1)})$ calculations for the central value of $\alpha_s^{(1)} = 0.18$, in the Jade more noticeably than in the Durham scheme. In contrast, it has been

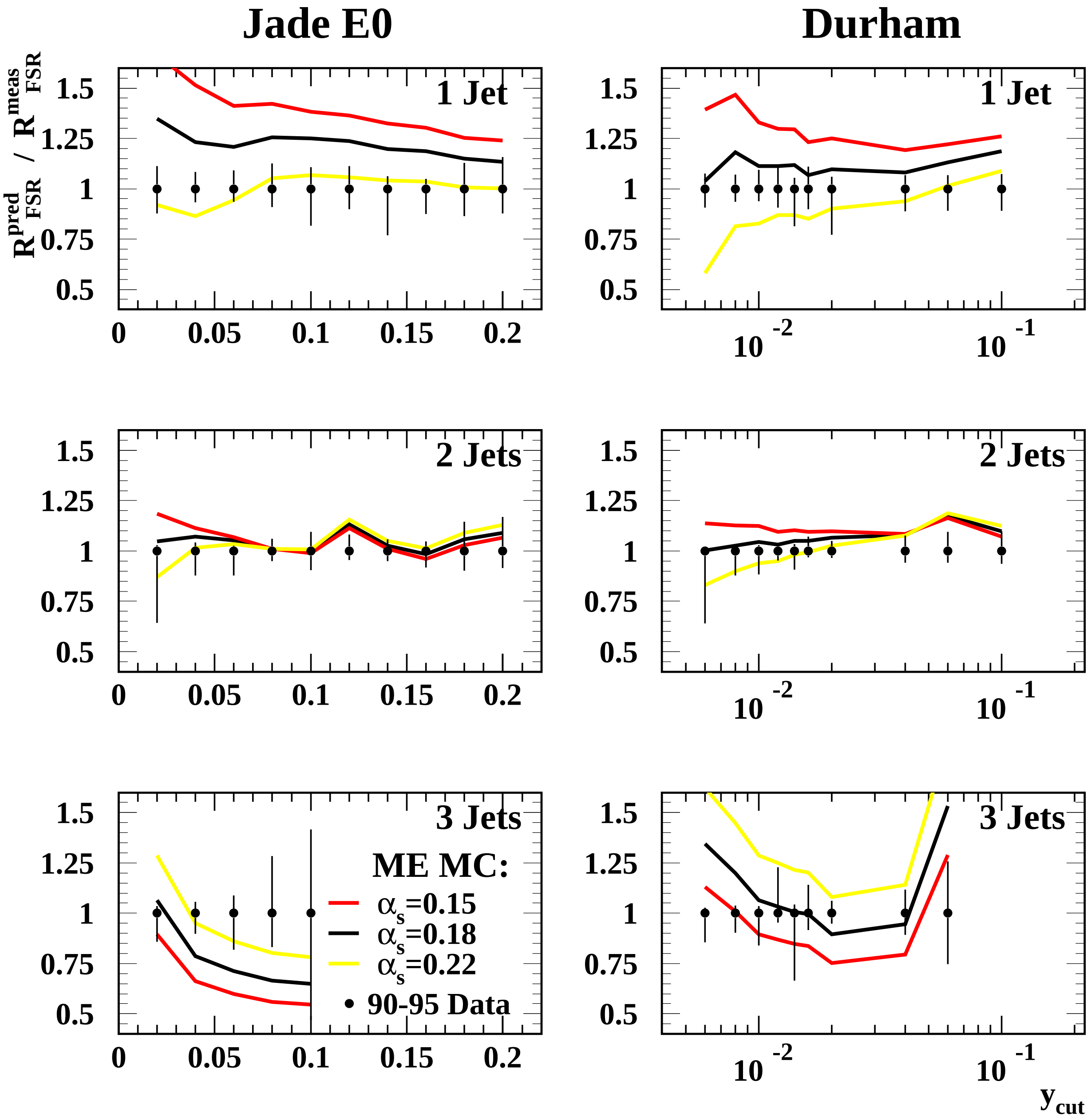

Figure 5.17: Prediction-to-measurement ratio of the FSR yield in hadronic Z^0 decays as a function of y_{cut} in the two jet finder schemes, differentiated according to the jet multiplicity in the event. Further explanations, see previous figure 5.16.

observed in [114], that the 1-jet+γ rate is reproduced well by GNJETS for most y_{cut} values. The measured 1-jet+γ rate of the present analysis is also smaller than the corresponding rate measured in [30].

The 2-jet+γ rate in the Jade scheme agrees well with the prediction of the ME calculation for most y_{cut} values. An upward fluctuation of the prediction-to-measurement ratio is visible at $y_{cut} = 0.02$ ($\alpha_s^{(1)} = 0.15$) and at $y_{cut} = 0.12$ (for all values of $\alpha_s^{(1)}$), the former probably being due to the limited order of the ME calculations. Choosing the central value of $\alpha_s^{(1)} = 0.18$ as input for GNJETS generally leads to a good description of the measured 2-jet+γ rate in both jet finder schemes. In the Durham case, however, again a slight photon excess at high values of y_{cut} is observed for the $\mathcal{O}(\alpha\alpha_s^{(1)})$ prediction, as previously seen in the total and the 1-jet+γ rate.

The 3-jet+γ rate in the Jade recombination scheme is underestimated by GNJETS. The discrepancy is becoming more significant with increasing y_{cut}. The decrease of the 3-jet rate as predicted by the $\mathcal{O}(\alpha\alpha_s^{(1)})$ calculation is faster than in data (see also figure 5.15). This definite tendency is not seen for the Durham algorithm, where the 3-jet rate is overestimated at low and high values of y_{cut}, and reproduced fairly well at intermediate values (at least as far as the central value of $\alpha_s^{(1)} = 0.18$ is concerned). The behaviour in both cases is most probably due to higher order QCD corrections, which are not included in the present matrix element Monte Carlo.

5.6 Results

Following the previous general discussion of the y_{cut}-dependent final state photon numbers in data and matrix element Monte Carlo, showing that its $\mathcal{O}(\alpha\alpha_s^{(1)})$ calculations yield reliable results, the fixing of the strong coupling constant in first order $\alpha_s^{(1)}$ as input parameter of the Monte Carlo, and the determination of the electroweak couplings using this Monte Carlo are adressed now.

5.6.1 Discussion of the Strong Coupling Constant in First Order

Referring to the considerations in section 2.2.1 and to equation 2.18 representing the ratio of 3-jet+γ events to the sum of 2- and 3-jet+γ events, values for $\alpha_s^{(1)}$ can be determined. The measured ratios R_{23}^{γ} as well as the corresponding values of $\alpha_s^{(1)}$ are listed in table 5.17 for the two jet recombination schemes and different y_{cut} values. In the Jade recombination scheme a tendency to higher values of $\alpha_s^{(1)}$ for increasing y_{cut} values becomes visible (see also figure 5.18). This observation is in accordance with what has been stated in the previous section when discussing the measured and the predicted 3-jet+γ event numbers. The increasing excess of 3-jet+γ events in data compared to the perturbative prediction for increasing values of y_{cut} consequently requires higher values of $\alpha_s^{(1)}$. Such a trend of increasing $\alpha_s^{(1)}$ with increasing y_{cut} values has already been observed at the same scale by OPAL [114], and by DELPHI [31], but the errors in these publications have been larger and most values agreed well within their errors.

L3 gets values of $\alpha_s^{(1)}$ between 0.163 and 0.171 from a simultaneous fit of results from ME calculations described in [116] to three data distributions (photon energy, photon angle to nearest jet, and transverse photon energy with respect to the thrust), whereas OPAL obtains

Jade E0		
y_{cut}	R_{23}^{γ}	$\alpha_s^{(1)}$
0.02	$0.319 \pm 0.004^{+0.078}_{-0.031}$	$0.177 \pm 0.002^{+0.038}_{-0.015}$
0.04	$0.138 \pm 0.003^{+0.016}_{-0.013}$	$0.240 \pm 0.004^{+0.028}_{-0.024}$
0.06	$0.050 \pm 0.001^{+0.007}_{-0.009}$	$0.267 \pm 0.006^{+0.039}_{-0.048}$
0.08	$0.017 \pm 0.001^{+0.005}_{-0.003}$	$0.281 \pm 0.008^{+0.084}_{-0.052}$
Durham		
y_{cut}	R_{23}^{γ}	$\alpha_s^{(1)}$
0.01	$0.251 \pm 0.004^{+0.023}_{-0.031}$	$0.179 \pm 0.002^{+0.016}_{-0.021}$
0.02	$0.141 \pm 0.003^{+0.008}_{-0.008}$	$0.218 \pm 0.005^{+0.015}_{-0.016}$

Table 5.17: The measured ratios R_{23}^{γ} defined by equation 2.18, and the resulting values for $\alpha_s^{(1)}$ extracted from a comparison with the matrix element MC for various values of y_{cut}. The first error contribution comes from the data statistics, the second from the combined systematic uncertainties.

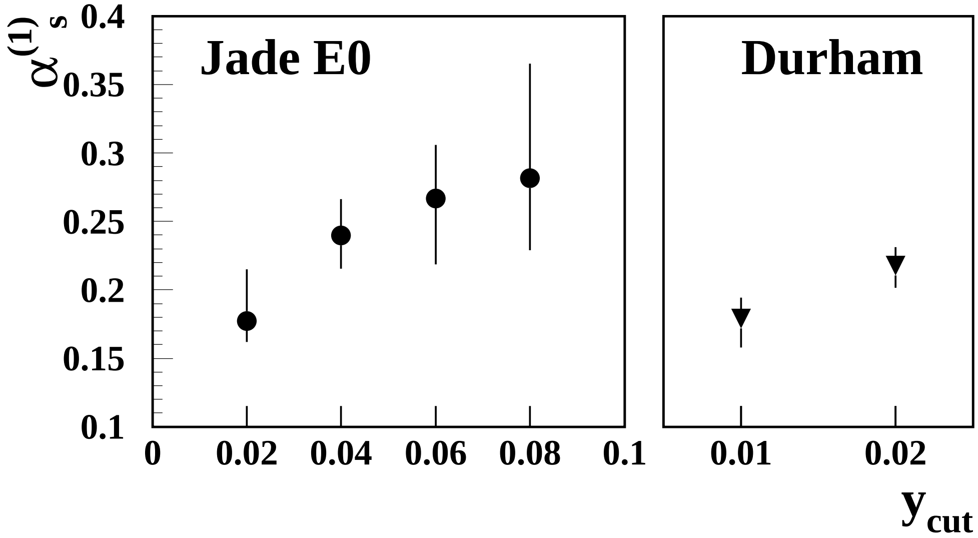

Figure 5.18: Values of $\alpha_s^{(1)}$ depending on y_{cut} as determined from the jet ratios R_{23}^{γ} in the two recombination schemes. The error bars represent the combined experimental and theoretical errors.

values between 0.045 and 0.193 from fitting an alternative ME Monte Carlo (EEPRAD, [40]) to the same distributions.

Moreover, values of $\alpha_s^{(1)}$ have been obtained from fits to jet rates in inclusive hadronic samples: OPAL measures 0.177 in the Jade and 0.21 in the Durham recombination scheme [30,115], L3 measures 0.19 [32].

The spread of these results are not only due to limited statistics, but also caused by the limited order of the available matrix element calculations. Besides, the different approaches which are chosen to restrict the phase space in which the photon yield is calculated lead to different sensitivities of the various results to non-perturbative effects like divergences due to radiated photons collinear with soft quarks [40–44]. However, the sensitivity of the presented analysis to the latter should be small, because all numbers are measured far away from the phase space boundaries. The trend to higher values of $\alpha_s^{(1)}$ for larger y_{cut} values seen in the Jade case of the present analysis may be explained by higher order gluon radiation occurring in data but not implemented in GNJETS. For large values of y_{cut}, decays with multiple gluon radiation may be subsumed in the measured 3-jet+γ rate, which thus is greater than predicted by the $\mathcal{O}(\alpha\alpha_s^{(1)})$ Monte Carlo for the central value of $\alpha_s^{(1)} = 0.18$.

As input value to the matrix element Monte Carlo, $\alpha_s^{(1)} = 0.18$ has been chosen to calculate the electroweak coupling constants and relatedly Z^0 decay widths into up- and down-type quarks.

5.6.2 Determination of the Z^0 Decay Widths into Up- and Down-type quarks

After having narrowed the range of values for $\alpha_s^{(1)}$ from the relative jet rates independently from the electroweak couplings c_{up} and c_{down}, the latter and relatedly the decay widths $\Gamma_{up-type}$ and $\Gamma_{down-type}$ can be calculated. In accordance with the previous studies and with other measurements quoted in the previous section, $\alpha_s^{(1)} = 0.18^{+0.04}_{-0.03}$ is chosen as central input value for the ME Monte Carlo GNJETS, which is used to calculate the $\mathcal{O}(\alpha\alpha_s)$ corrections $F(y_{cut})$ in equation 2.8. From the partial width of Z$^0 \to hadrons + \gamma$ decays the following correlation of the decay widths into up- and down-type quarks is derived:

$$\Gamma_{q\bar{q}\gamma} \equiv \Gamma(\mathrm{Z}^0 \to n\mathrm{Jets} + \gamma)(y_{cut}) = \frac{\alpha}{18\pi}\frac{F(y_{cut})}{K_{QCD}}(8\Gamma_{u-type} + 3\Gamma_{d-type}). \tag{5.18}$$

$\Gamma(\mathrm{Z}^0 \to n\mathrm{Jets}+\gamma)(y_{cut})$ can be expressed in terms of the total hadronic width and the measured FSR rate, thus one gets:

$$8\Gamma_{u-type} + 3\Gamma_{d-type} = R_{\mathrm{Z}^0\to(n\mathrm{Jets}+\gamma)}(y_{cut}) \times \Gamma(\mathrm{Z}^0 \to \mathrm{hadrons})\frac{18\pi}{\alpha}\frac{K_{QCD}}{F(y_{cut})}. \tag{5.19}$$

Taking the world average of $\alpha_s = 0.1184(12)$ and of $\Gamma_{\mathrm{had}} \equiv \Gamma(\mathrm{Z}^0 \to \mathrm{hadrons}) = 1.7438(22)$ GeV as quoted by the PDG [10] one derives

$$8\Gamma_{u-type} + 3\Gamma_{d-type} = 3.46 \pm 0.12^{+0.32+0.25+0.05}_{-0.12-0.17-0.01} \quad \mathrm{GeV}$$

in the Jade scheme at a value of $y_{cut} = 0.08$, where the theoretical and experimental errors are smallest. Accordingly, the value calculated in the Durham scheme at $y_{cut} = 0.016$ is

$$8\Gamma_{u-type} + 3\Gamma_{d-type} = 3.47 \pm 0.10^{+0.15+0.27+0.08}_{-0.13-0.47-0.10} \quad \mathrm{GeV}.$$

In both expressions, the first error contribution is from the data statistics, the second from the background estimation, the third from the efficiency correction, and the fourth from theoretical uncertainties, mainly due to the ME calculation. The correlation of the Z^0 decay widths into up- and down-type quarks is illustrated in the top plot of figure 5.19. The coordinates of the

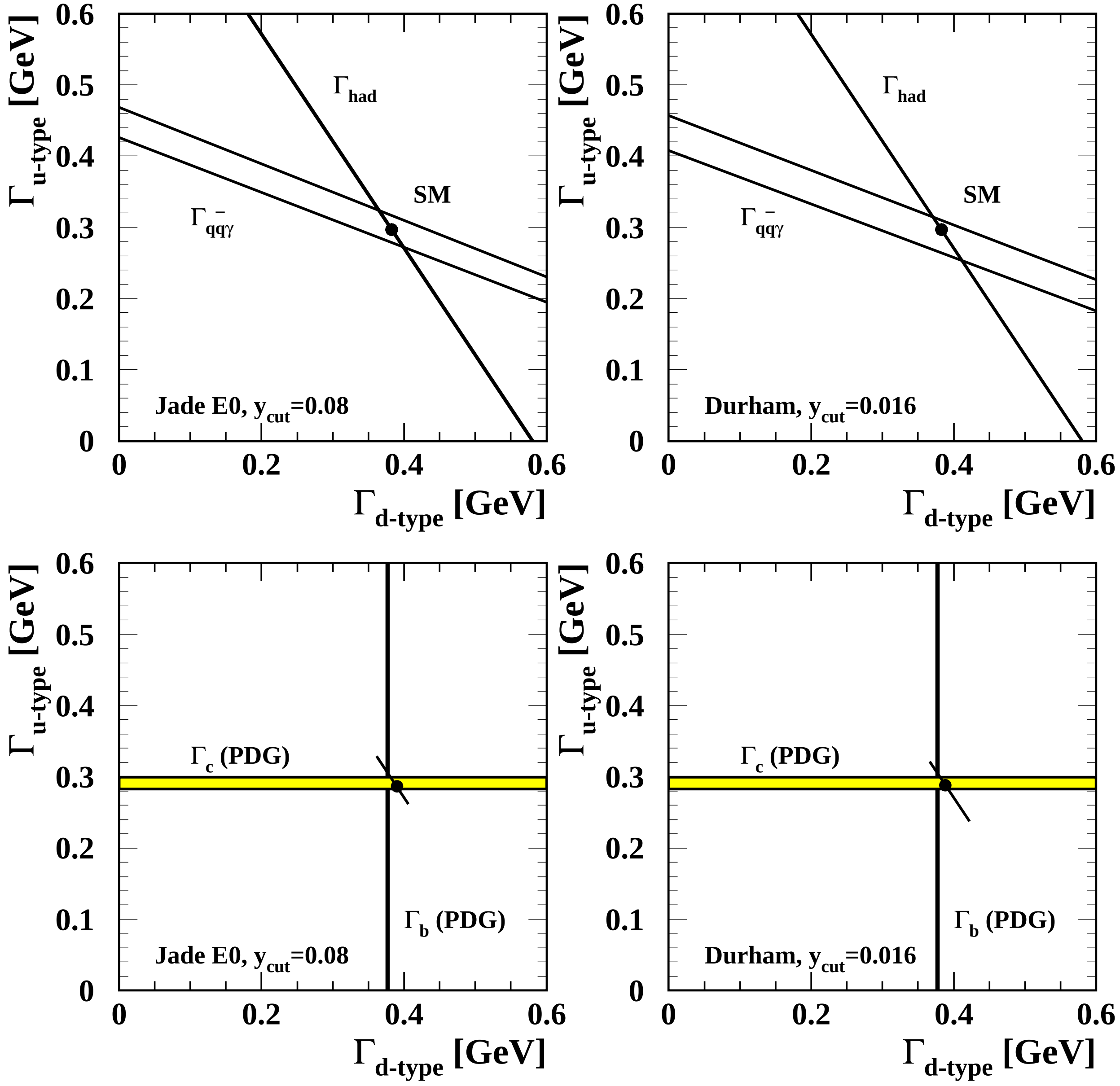

Figure 5.19: Top: Correlation of the decay widths of the Z^0 into up- and down-type quarks. Shown are the relations obtained within one standard deviation from the measured hadronic width (world average as quoted by the PDG) and from the width $\Gamma_{qq\gamma}$ (this measurement).
Bottom: Correlation plot of Γ_{u-type} vs. Γ_{d-type} as obtained from this measurement. The partial widths of the Z^0 decay into charm and bottom quarks are also indicated.

standard model value $(\Gamma_{d-type}, \Gamma_{u-type})^{\mathrm{SM}}$ are also indicated, being well within the intersection region of Γ_{had} and $\Gamma_{q\bar{q}\gamma}$, which is defined by the size of one standard deviation of the present

Coupling	Jade E0		Durham		Standard model prediction
	$y_{cut} = 0.08$	$y_{cut} = 0.12$	$y_{cut} = 0.016$	$y_{cut} = 0.04$	
c_{up}	$1.107^{+0.166}_{-0.095}$	$1.161^{+0.188}_{-0.107}$	$1.116^{+0.128}_{-0.197}$	$1.008^{+0.200}_{-0.129}$	1.148
c_{down}	$1.508^{+0.063}_{-0.111}$	$1.472^{+0.072}_{-0.125}$	$1.502^{+0.131}_{-0.085}$	$1.574^{+0.086}_{-0.134}$	1.477

Table 5.18: The electroweak couplings c_{up} and c_{down} and their total error as extracted from the FSR rate. For comparison, the standard model values are also listed.

$\Gamma_{q\bar{q}\gamma}$ measurement and of the world average of $\Gamma_{\rm had}$. The additional information from $\Gamma_{\rm had} = 2\Gamma_{u-type} + 3\Gamma_{d-type}$ finally leads to widths of the Z^0 decay into up and down-type quarks of (cf. equation 2.23)

$$\Gamma_{u-type} = 286 \pm 12^{+32+25+5}_{-12-17-1} \quad \text{MeV} \qquad \text{and} \qquad \Gamma_{d-type} = 390 \pm 8^{+8+12+1}_{-22-16-4} \quad \text{MeV}$$

in the Jade scheme ($y_{cut} = 0.08$), and

$$\Gamma_{u-type} = 288 \pm 10^{+15+27+8}_{-13-47-10} \quad \text{MeV} \qquad \text{and} \qquad \Gamma_{d-type} = 388 \pm 6^{+9+32+7}_{-10-18-5} \quad \text{MeV}$$

in the Durham scheme ($y_{cut} = 0.016$), where the uncertainties are given in the same order as above. The standard model prediction for Γ_{u-type} and Γ_{d-type} is:

$$\Gamma_{u-type} = 292 \quad \text{MeV} \qquad \text{and} \qquad \Gamma_{d-type} = 386 \quad \text{MeV}.$$

In the bottom plots of figure 5.19 the measured values of Γ_{u-type} and Γ_{d-type} are sketched in the $(\Gamma_{d-type}, \Gamma_{u-type})$ plane. Since the results are fully negatively correlated the one standard deviation contour degenerates to a narrow bar, as can be seen in the two dimensional representation. For comparison, the partial widths of the Z^0 decays into charm and bottom quarks [10] are also indicated.

The relevant values for the couplings c_{up} and c_{down} are listed in table 5.18 together with the numbers extracted at the two y_{cut} values, for which the second smallest errors are observed. The standard model prediction introduced in chapter 2 is also given. All results determined at different y_{cut} values as well as with different jet recombination schemes agree well within their errors, suggesting that the analysis method is stable.

5.6.2.1 Comparison with other Measurements

There exist measurements of the prompt final state photon production rate in hadronic Z^0 decays by all four LEP experiments [30–32, 58]. Three of them have also extracted values for the electroweak coupling constants c_{up} and c_{down} from their measurement. These are listed with their total errors in table 5.19, together with the results of the presented analysis.

Sharing the principle idea of measuring c_{up} resp. c_{down} by taking advantage of the photon coupling to charge, the analyses in particular differed in their methods of background estimation. OPAL [30] estimated the fraction of selected candidates coming from neutral hadrons exploiting isospin symmetry: the measured rate of isolated charged tracks was translated into

Measurement	c_{up}	c_{down}
OPAL([30])	0.94 ± 0.18	1.62 ± 0.12
L3([32])	0.92 ± 0.22	1.63 ± 0.15
DELPHI([31])	$0.91^{+0.25}_{-0.36}$	$1.62^{+0.24}_{-0.17}$
this measurement Jade E0: $y_{cut} = 0.08$	$1.11^{+0.17}_{-0.10}$	$1.51^{+0.06}_{-0.11}$
Durham : $y_{cut} = 0.016$	$1.12^{+0.13}_{-0.20}$	$1.50^{+0.13}_{-0.09}$

Table 5.19: Comparison with other measurements using prompt final state photon production to measure c_{up} and c_{down}.

the rate of isolated neutral particles. Folding the latter with corrections like the hadron rejection efficiency of the requirements on the shape of a shower in the ECAL, which had been determined with the detector simulation, the fraction of neutral hadrons in the selected candidate sample was derived. L3 [32] directly identified and rejected low-energy neutral hadron background by its characteristic shower shape in the ECAL, and estimated the remaining high-energy background from a sample of Monte Carlo events. DELPHI [31] in principle estimated the fragmentation background with JETSET 7.3 [117], but the simulated neutral hadron contamination was rescaled depending on the energy according to cross-checks which had been performed with a sample of non-isolated clusters in the ECAL which could be combined with other clusters and with a sample of isolated cluster candidates anti-tagged by the shower shape requirements.
The background due to initial state radiation was estimated using JETSET 7.3 (OPAL) and DYMU3 [118] (DELPHI), describing ISR in highest order and thus with the highest precision availabe at that time.
The theoretical framework, in which the $\mathcal{O}(\alpha\alpha_s)$ corrections $F(y_{cut})$, the missing link between y_{cut}-dependent FSR rate and cross-section, were calculated, was the same for OPAL and DELPHI, namely GNJETS [44] and EEPRAD [40], whereas L3 used a different approach [116].

As can be seen in table 5.19, the three previous measurements have derived numbers for c_{up} (c_{down}), which are very similar and shifted towards smaller (higher) values than predicted by the standard model. However, the observed shifts are not significant. The results reflect the observation by all four LEP experiments of slightly lower photon rates than predicted with the help of various matrix element calculations at values of $\alpha_s^{(1)}$ between 0.118 and 0.21 [30–32, 58].

The present measurement may also be compared to measurements of the branching fractions of the Z^0 into heavy and light quarks. The average values of the Z^0 decay widths Γ_c and Γ_b as given by the PDG are indicated in the bottom plots of figure 5.19 (as pointed out earlier in this section). The decay widths into u, d/s quarks can be inferred from a publication by OPAL [119], where a measurement of the branching fractions of Z^0 into up- and down-type light quarks employing high-momentum stable particles in a jet as tag for the quantum numbers of the according primary quark is presented. To obtain the branching ratio $R_q = \Gamma_{Z^0 \to q\bar{q}}/\Gamma_{\rm had}$ from this measurement of

$$R_{q'} = \frac{\Gamma_{q\bar{q}}}{\Gamma_{d\bar{d}} + \Gamma_{u\bar{u}} + \Gamma_{s\bar{s}}} = \frac{R_q}{R_d + R_u + R_s}$$

this Measurement	$R_{up-type}$	$R_{down-type}$
Jade E0: $y_{cut} = 0.08$	$0.164^{+0.025}_{-0.014}$	$0.224^{+0.009}_{-0.016}$
Durham : $y_{cut} = 0.016$	$0.165^{+0.019}_{-0.029}$	$0.223^{+0.020}_{-0.013}$
OPAL [119]	R_u	$R_{d,s}$
	$0.160 \pm 0.019 \pm 0.019$	$0.230 \pm 0.010 \pm 0.010$

Table 5.20: Comparison with a measurement of branching fractions of the Z^0 into light quarks.

Relative error in % for E0 scheme							
OPAL([30])				this measurement			
y_{cut}	0.005	0.06	0.20	y_{cut}	0.005	0.06	0.20
Statistics	3.7	4.9	7.6	Statistics	1.1	1.9	4.5
Monte Carlo statistics	2.2	2.6	3.9	Monte Carlo statistics	1.2	1.4	3.1
Background	4.1	3.4	3.2	Background	$^{+0.7}_{-2.8}$	$^{+1.5}_{-2.4}$	$^{+15.1}_{-5.4}$
Jet energies Acceptance of multihad. Photon efficiency	1.2	1.7	1.8	$c^{ISR+FSR}(y_{cut})$	1.7	1.6	1.4
Energy and isolation cut	13.0	5.0	7.0	$c^{FSR}(y_{cut})$	+3.7 -23.3	+3.3 -7.7	+7.3 -7.4
Sum	14.3	8.4	11.6	Sum	14.0	6.6	14.2

Table 5.21: Comparison of the error contributions in the former and the present analysis of FSR events.

the constraint

$$R_d + R_u + R_s = 1 - R_c - R_b$$

assuming $R_c + R_b = 0.380 \pm 0.010$ is used, which results in the values listed in table 5.20 together with the branching ratios $R_{up-type}$ and $R_{down-type}$ as obtained from the measured final state photon rate.

5.6.2.2 Discussion of Measurement Errors

In table 5.21, the uncertainties of the previous and the present measurement of prompt photon production in hadronic Z^0 decays to determine c_{up} and c_{down} with the OPAL detector are compared. The relative error contributions at three y_{cut} values in the E0 scheme are listed. Due to the different methods of background estimation, they cannot be given in exactly the same manner. Therefore, the uncertainties given in [30] are rearranged such, that they account for similar effects as studied in the present measurement. As explained in section 5.2.1.2, to estimate the size of the effect from either Monte Carlo or data statistic on the background estimation the error contributions have been scaled corresponding to the data and Monte Carlo statistics available for the fit (c.f. table 5.3). The error contribution from data is as expected larger than that from Monte Carlo. To the Monte Carlo statistics uncertainty quoted in table 5.21 not only the error of the binned maximum likelihood fit contributes but also the statistical error from the efficiency correction which is estimated using JETSET and the detector Monte Carlo GOPAL.

Except for $y_{cut} = 0.20$, the sums of the errors in the present measurement (building the average of the positive and the negative contribution) are smaller. The ranking of the error contributions according to their size is similar in both measurements with the last uncertainty listed being largest, and the background uncertainty being second largest. However, a large asymmetry of these errors is visible in the present measurement. For both contributions, the systematic error estimates are conservative, always taking the largest deviation observed for each y_{cut} (and in the likelihood fit case also for each study) as uncertainty. The largest deviation noticed in the systematic study of the binned maximum likelihood fit for almost all values of y_{cut} is, for example, caused by using C distributions of neutral hadron clusters generated with HERWIG. However, the available sample of HERWIG events is with about 2.4 million hadronic Z^0 decays much smaller than the JETSET sample, which is utilised for the fit. Studying the efficiency corrections (cf. table 5.21, row labelled energy and isolation cut and $c^{FSR}(y_{cut})$) also HERWIG gives the largest systematic deviation yielding smaller correction factors c^{FSR}, and thus, producing the large error asymmetry in particular at small values of y_{cut}. Such an asymmetry is not seen for the errors as given by the previous OPAL measurement, although the authors of [30] note, that for larger y_{cut} HERWIG gives somewhat smaller c^{FSR}. Remarkably, the error on c^{FSR} in the present measurement are not smaller than in [30], even though there, in contrast to the present measurement, the photon rates have also been corrected to compensate the losses due to the cut on the photon energy. One may conclude from this, that the systematics of the efficiency corrections is dominated by the uncertainty in the Monte Carlo description of the energy flow around the photon candidate. Especially, the estimation of this effect seems to be more pessimistic in the present analysis compared to [30]. A less strict cone isolation requirement, allowing more energy inside the isolation cone might lead to a smaller systematic uncertainty.

Chapter 6

Summary and Conclusions

In this thesis, a determination of the electroweak couplings to up- and down-type quarks has been presented. The determination is based on the measurement of the number of prompt photons radiated off the final state quarks in e^+e^- reactions at the Z^0 resonance. The whole data sample of multihadronic Z^0 decays taken by the OPAL experiment during the LEP1 phase between 1989 and 1995 is used for the measurement, and a total of 10400 candidates for decays with radiated isolated photons are selected. The main effort in this analysis has been put into the estimation of the hadronic background to the selected candidate clusters in the electromagnetic calorimeter of OPAL. Compared to earlier measurements of the isolated final state photon cross-section, an alternative method has been applied in this thesis, employing a binned maximum likelihood fit of simulated distributions of a photon likeness variable C to the relevant data distributions of C. It has been shown in studies of simulated and measured shower shapes produced by photons when interacting with the lead glass of the calorimeter, that the showers are described well by the detector simulation and that the binned maximum likelihood method yields reliable results. The background due to photons produced by initial state radiation of the incoming leptons has been calclulated by using the new Monte Carlo generator $\mathcal{KK}$.

Applying two jet finder algorithms, Durham and Jade E0, to the selected events allows a comparison of the measured number of photons produced by final state radiation with the yield of matrix element calculations of $\mathcal{O}(\alpha\alpha_s)$. A good agreement is observed between data and theoretical predictions. From the measurement of the ratio of events with three jets and a photon to those with two jets and a photon, a value of α_s in first order of $0.177^{+0.038}_{-0.015}$ is determined. This α_s value serves as input parameter for $\mathcal{O}(\alpha\alpha_s)$ matrix element calculations which are then used to determine the electroweak coupling constants. The resulting couplings are

$$c_{up-type} = 1.107^{+0.166}_{-0.095} \qquad \text{and} \qquad c_{down-type} = 1.508^{+0.063}_{-0.111}. \tag{6.1}$$

They are related to the partial decay widths

$$\Gamma_{up-type} = 286^{+43}_{-24}\text{MeV} \qquad \text{and} \qquad \Gamma_{down-type} = 390^{+17}_{-29}\text{MeV}. \tag{6.2}$$

The error is dominated by the systematic uncertainties due to the cone isolation requirement and the overall modelling of parton showers in hadronic final states at the Z^0 resonance. The values are in good agreement with the Standard Model expectation of

$$\Gamma_{up-type} = 292\mathrm{MeV} \qquad \text{and} \qquad \Gamma_{down-type} = 386\mathrm{MeV}. \tag{6.3}$$

The measurement result also agrees with an earlier measurement performed by OPAL based on lower data statistics and utilising alternative methods for the background estimation [30], and with the results of the other LEP experiments [31,32,119].

Appendix A

Comparing Different Cluster Shape Fit Programs

To get the best possible photon identification three different algorithms to identify photon clusters in the barrel region of the electromagnetic calorimeter were compared. The one which is chosen is described in chapter 4. The other two are briefly recapulated here. The first one is a maximum entropy fit (MEF) which is described in [120]. It is based on Bayes' Theorem.

The results of the comparison between the χ^2 cluster shape fit (CSF) and the maximum entropy method are shown in figure A.1. The purities and efficiencies for six different energy bins are plotted. Four variables are under investigation, two from the maximum entropy method, two from the χ^2 fit. The number of maxima or four vectors that could be fitted in the cluster N_{4vec} and the variable MOM (a kind of "moment of inertia") are the figures of merit for the maximum entropy method in this comparison. The variables supplied by the χ^2 fit are C which is defined in chapter 4 and R_{mom}. R_{mom} is defined by

$$R_{mom} = \frac{\Sigma_{i=1}^{N_{blocks}} r_i \cdot (E_{meas,i} - E_{exp,i})}{\Sigma_{i=1}^{n} E_{meas,i}} \tag{A.1}$$

and corresponds to the difference of the weighted averages of the radial distance from the shower origin, i.e. $< r >_{meas} - < r >_{exp}$. If R_{mom} is less than zero the cluster is smaller than an ideal photon cluster. From both, efficiency plot and purity plot in figure A.1, it becomes evident that the χ^2 method yields a better performance than the maximum entropy fit. Both variables of the maximum entropy fit are less powerful in identifying photons in the electromagnetic calorimeter and separating them from clusters caused by hadronic background. Therefore the maximum entropy is not used in our anlysis. For the two cluster shape fit variables R_{mom} and C more detailed studies were carried out which showed that C always yields higher purities at comparable efficiencies.

The third cluster shape fit under investigation is implemented in the χ^2 fit routine but it is based on an analytical integration mode compared to the VEGAS integration used in the 'old' version. The 'new' cluster shape fit is based on a so called 'ring fraction' method where for each calorimeter block, a fixed number of rings are defined centred around the origin of the electromagnetic shower [121]. By integrating the same two dimensional, empirically determined

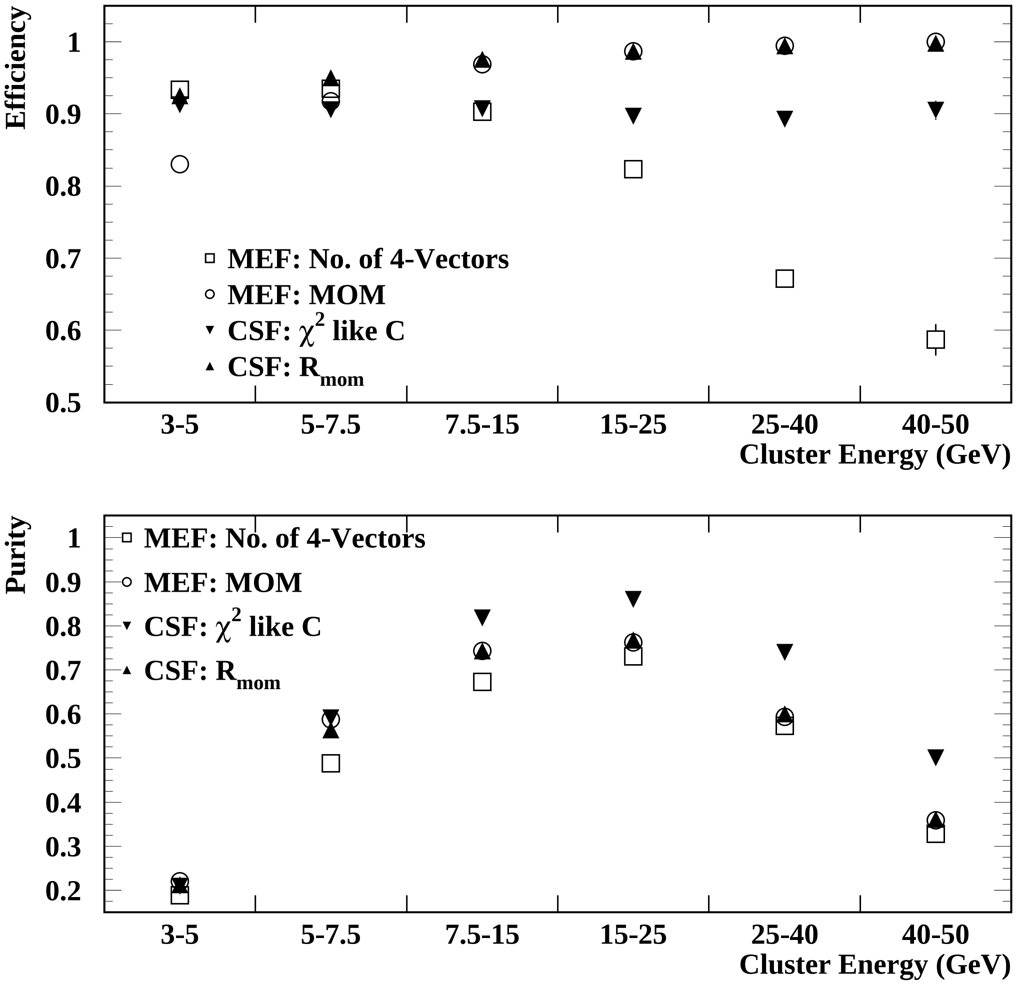

Figure A.1: Efficiencies and purities in the single-photon identification for two different cluster fit methods. Two cut variables are from the maximum entropy fit (MEF) and two are from the cluster shape fit (CSF).

shape function as introduced in chapter 4 over these ring segments the energy deposited in the ring fractions lying in each calorimeter block is derived. Thus, as for the 'old' fit one gets an expected energy E_i^{exp} for each block in the cluster depending on the set of angles (θ,ϕ) of the shower origin. The procedure in the 'new' version is the same as for the 'old' one apart from the block integration and the same variables C and R_{mom} are calculated. The 'new' algorithm is much faster (about four times according to its author) but has the disadvantage that the defined rings in the integration are equidistant therefore are independent of the curve shape of the energy profile function. The flexible VEGAS algorithm on the other hand automatically concentrates the evaluations of the integrand in those regions where the values of the integrand become very large. As a result the performance of the VEGAS method should be better. To archieve a comparable performance to that of the VEGAS integration the ring distances have to be chosen smaller in particular around the assumed shower origin to account for the profile function.[1]

In figures A.2 the photon efficiencies that were calculated for the 'new' and the 'old' version of the CSF are compared for data and Monte Carlo. This is again done for six bins of the cluster energy. The sample of $Z^0 \to \mu^+\mu^-\gamma$ events was selected from data taken at the Z pole between 1990 and 1995 as described in section 4.3. The Monte Carlo sample corresponds to the 1994 detector configuration, i.e. the year in which most of the data were collected. The figures A.2 reveal a weakness of the ring fraction method for higher cluster energies where the efficiency of the 'new' CSF version is declining. At the same time, the efficiency derived with the 'old' version does not depend on the cluster energy. In addition, a large discrepancy between data and Monte Carlo efficiency is observed for the 'new' version at cluster energies larger then 25 GeV. This might be a consequence of the simpler ring integration with a step size fixed by the radii of the rings around the cluster centre regardless of its profile. Figure A.3 shows that the efficiencies of the 'new' and 'old' CSF are of the same magnitude except for the already mentioned two highest energy bins.

For the analysis, the VEGAS based cluster shape fit is finally chosen despite its CPU consumption because it showed an overall performance that was better than the two alternatively studied shower shape fit methods.

---

[1] In this case the "ring fraction" integration would become more time consuming but this has not been quantified yet.

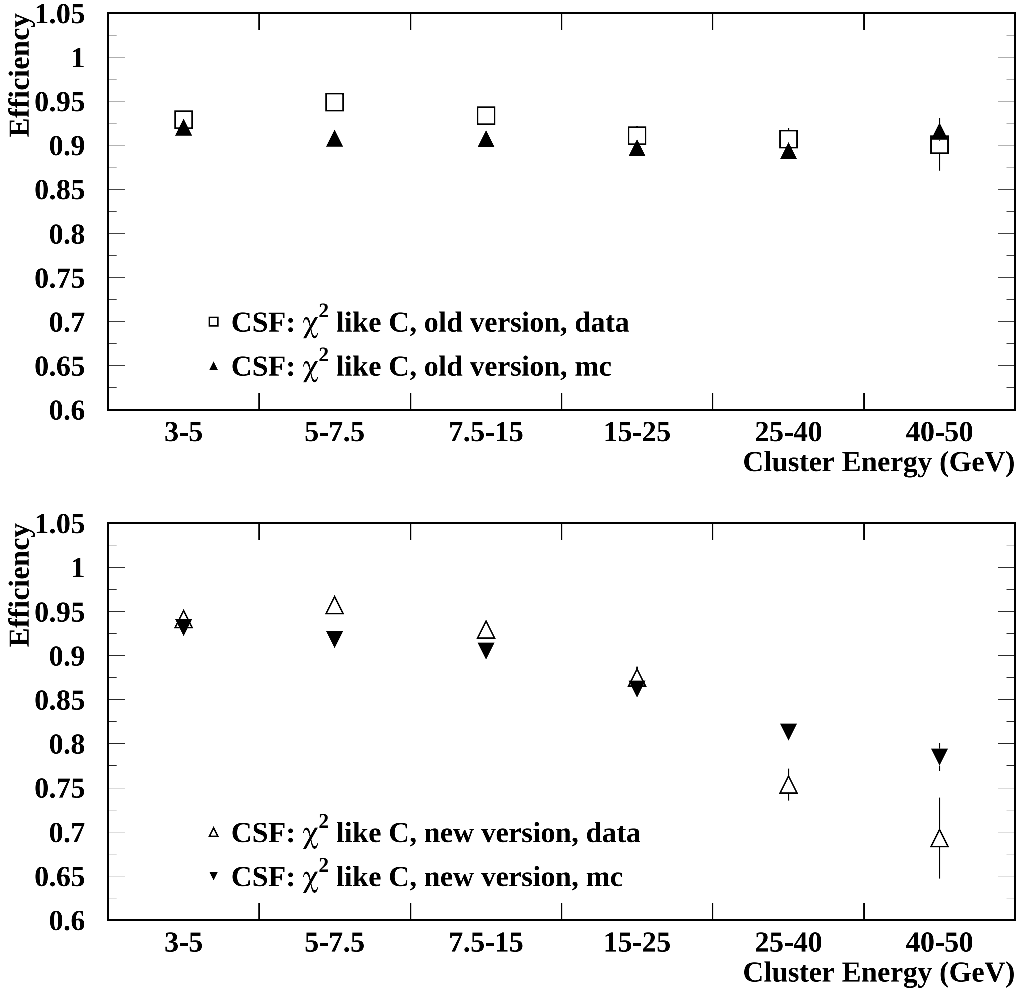

Figure A.2: Efficiencies of the single-photon identification in $Z^0 \rightarrow \mu^+\mu^-\gamma$ Monte Carlo (94) and data (90-95) for two different cluster fit methods: the 'ring fraction' method ('new' ,the bottom plot), and the VEGAS method ('old', the top plot). For details see text.

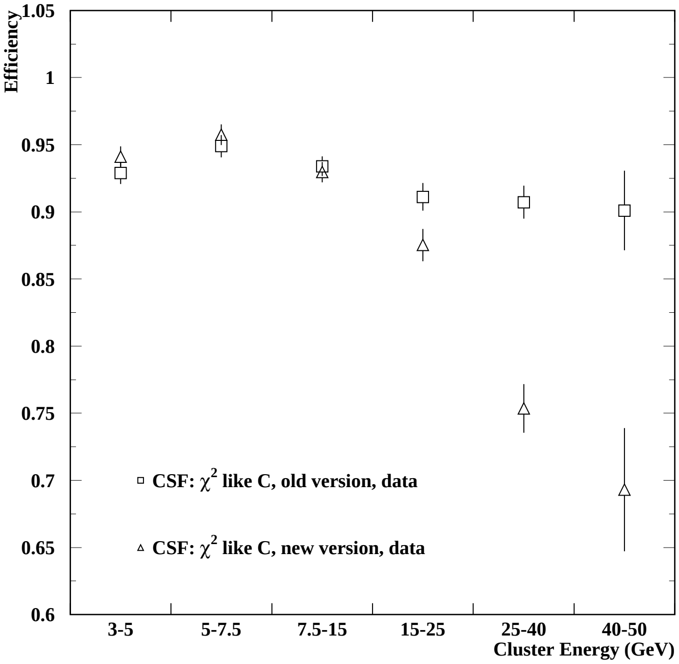

Figure A.3: Efficiencies of the single-photon identification for two different cluster fit methods in $Z^0 \to \mu^+\mu^-\gamma$ data: the 'ring fraction' method ('new'), and the VEGAS method ('old'). For details see text and figure A.2.

Bibliography

[1] G. N. Lewis. Nature, Vol. 118, Part 2, December 18, 1926, page 874-875.

[2] H. Fritzsch and M. Gell-Mann, “Current Algebra: Quarks and What Else?,”. in: Proc. XVIth Int. Conf. on High Energy Physics, Chicago 1972, 135.

[3] H. Fritzsch, M. Gell-Mann, and H. Leutwyler, “Advantages of the Color Octet Gluon Picture,” *Phys. Lett.* **B47** (1973) 365–368.

[4] D. J. Gross and F. Wilczek, “Ultraviolet Behavior of Nonabelian Gauge Theories,” *Phys. Rev. Lett.* **30** (1973) 1343.

[5] H. D. Politzer, “Reliable Perturbative Results for Strong Interactions?,” *Phys. Rev. Lett.* **30** (1973) 1346.

[6] S. L. Glashow, “Partial Symmetries of Weak Interactions,” *Nucl. Phys.* **22** (1961) 579–588.

[7] S. Weinberg, “A Model of Leptons,” *Phys. Rev. Lett.* **19** (1967) 1264–1266.

[8] A. Salam, “Weak and Electromagnetic Interactions,”. Originally printed in *Svartholm: Elementary Particle Theory, Proceedings Of The Nobel Symposium Held 1968 At Lerum, Sweden*, Stockholm 1968, 367-377.

[9] P. W. Higgs, “Broken Symmetries, Massless Particles and Gauge Fields,” *Phys. Lett.* **12** (1964) 132–133.

[10] **Particle Data Group** Collaboration, D. E. Groom *et al.*, “Review of Particle Physics,” *Eur. Phys. J.* **C15** (2000) 1.

[11] **OPAL** Collaboration, G. Abbiendi *et al.*, “Tests of the Standard Model and Constraints on New Physics from Measurements of Fermion Pair Production at 189-GeV at LEP,” *Eur. Phys. J.* **C13** (2000) 553, `hep-ex/9908008`.

[12] E. Laermann, T. F. Walsh, I. Schmitt, and P. Zerwas, “Direct Photons in e^+e^- Annihilation,” *Nucl. Phys.* **B207** (1982) 205.

[13] E. Fernandez *et al.*, “Direct Photon Production in e^+e^- Annihilation,” *Phys. Rev. Lett.* **54** (1985) 95.

[14] **JADE** Collaboration, W. Bartel *et al.*, “A Study of Photon Production in Hadronic e^+e^- Annihilation,” *Z. Phys.* **C28** (1985) 343.

[15] **TASSO** Collaboration, W. Braunschweig *et al.*, “Evidence for Direct Photons From Quarks in Electron - Positron Annihilation,” *Z. Phys.* **C41** (1988) 385.

[16] G. Altarelli, R. K. Ellis, G. Martinelli, and S.-Y. Pi, “Processes Involving Fragmentation Functions beyond the Leading Order in QCD,” *Nucl. Phys.* **B160** (1979) 301.

[17] W. Furmanski and R. Petronzio, “Singlet Parton Densities beyond Leading Order,” *Phys. Lett.* **B97** (1980) 437.

[18] G. Curci, W. Furmanski, and R. Petronzio, “Evolution of Parton Densities Beyond Leading Order: The Nonsinglet Case,” *Nucl. Phys.* **B175** (1980) 27.

[19] E. Witten, “Anomalous Cross-Section for Photon - Photon Scattering in Gauge Theories,” *Nucl. Phys.* **B120** (1977) 189–202.

[20] C. H. L. Smith, “QCD Predictions for Processes Involving Real Photons,” *Phys. Lett.* **B79** (1978) 83.

[21] **ALEPH** Collaboration, D. Buskulic *et al.*, “First Measurement of the Quark to Photon Fragmentation Function,” *Z. Phys.* **C69** (1996) 365–378.

[22] **OPAL** Collaboration, K. Ackerstaff *et al.*, “Measurement of the Quark to Photon Fragmentation Function Through the Inclusive Production of Prompt Photons in Hadronic Z^0 Decays,” *Eur. Phys. J.* **C2** (1998) 39, `hep-ex/9708020`.

[23] D. W. Duke and J. F. Owens, “Quantum Chromodynamics Corrections to Deep Inelastic Compton Scattering,” *Phys. Rev.* **D26** (1982) 1600.

[24] J. F. Owens, “Large Momentum Transfer Production of Direct Photons, Jets, and Particles,” *Rev. Mod. Phys.* **59** (1987) 465.

[25] M. Gluck, E. Reya, and A. Vogt, “Parton Fragmentation into Photons beyond the Leading Order,” *Phys. Rev.* **D48** (1993) 116–128.

[26] L. Bourhis, M. Fontannaz, and J. P. Guillet, “Quark and Gluon Fragmentation Functions into Photons,” *Eur. Phys. J.* **C2** (1998) 529, `hep-ph/9704447`.

[27] **OPAL** Collaboration, M. Z. Akrawy *et al.*, “Evidence for Final State Photons in Multi - Hadronic Decays of the Z^0,” *Phys. Lett.* **B246** (1990) 285–296.

[28] P. Mattig and W. Zeuner, “Final State Photon Bremsstrahlung in $e^+e^- \to Z^0 \to$ hadrons as a Tool for a Precise Measurement of the Weak Quark Couplings,” *Z. Phys.* **C52** (1991) 31–42.

[29] **OPAL** Collaboration, G. Alexander *et al.*, “A Measurement of the Electroweak Couplings of Up and Down Type Quarks Using Final State Photons in Hadronic Z^0 Decays,” *Phys. Lett.* **B264** (1991) 219–232.

[30] **OPAL** Collaboration, P. D. Acton *et al.*, "Studies of Strong and Electroweak Interactions Using Final State Photon Emission in Hadronic Z^0 Decays," *Z. Phys.* **C58** (1993) 405–418.

[31] **DELPHI** Collaboration, P. Abreu *et al.*, "Study of Prompt Photon Production in Hadronic Z^0 Decays," *Z. Phys.* **C69** (1995) 1–14.

[32] **L3** Collaboration, O. Adriani *et al.*, "Determination of Quark Electroweak Couplings from Direct Photon Production in Hadronic Z Decays," *Phys. Lett.* **B301** (1993) 136–144.

[33] **JADE** Collaboration, W. Bartel *et al.*, "Experimental Studies on Multi - Jet Production in e^+e^- Annihilation at Petra Energies," *Z. Phys.* **C33** (1986) 23.

[34] **JADE** Collaboration, S. Bethke *et al.*, "Experimental Investigation of the Energy Dependence of the Strong Coupling Strength," *Phys. Lett.* **B213** (1988) 235.

[35] S. Catani, Y. L. Dokshitzer, M. Olsson, G. Turnock, and B. R. Webber, "New Clustering Algorithm for Multi - Jet Cross-Sections in e^+e^- Annihilation," *Phys. Lett.* **B269** (1991) 432–438.

[36] N. Brown and W. Stirling, "Finding Jets and Summing Soft Gluons: A New Algorithm," *Z. Phys.* **C53** (1992) 629–636.

[37] G. Kramer and B. Lampe, "QCD Corrections to Final State Photon Bremsstrahlung in e^+e^- Annihilation," *Phys. Lett.* **B269** (1991) 401–406.

[38] G. R. Farrar and B. L. Ioffe, "$e^+e^- \to \gamma +$ Hadrons," *Phys. Lett.* **B71** (1977) 118.

[39] G. Kramer and H. Spiesberger, "Matrix Element Calculation of Quark Bremsstrahlung in $O(\alpha\alpha_s)$,". Presented at Workshop on Photon Radiation from Quarks, Annecy, France, Dec 2-3, 1991, DESY-92-022.

[40] E. W. N. Glover and W. J. Stirling, "Isolated Hard Photon Radiation in Multijet Production at LEP," *Phys. Lett.* **B295** (1992) 128–135.

[41] Z. Kunszt and Z. Trocsanyi, "QCD Corrections to Photon Production in Association with Hadrons in e^+e^- Annihilation," *Nucl. Phys.* **B394** (1993) 139–168, `hep-ph/9207232`.

[42] E. L. Berger, X. Guo, and J. Qiu, "Breakdown of Conventional Factorization for Isolated Photon Cross Sections," *Phys. Rev. Lett.* **76** (1996) 2234–2237, `hep-ph/9512281`.

[43] E. L. Berger, X. Guo, and J. Qiu, "Isolated Prompt Photon Production in Hadronic Final States of e^+e^- Annihilation," *Phys. Rev.* **D54** (1996) 5470–5495, `hep-ph/9605324`.

[44] P. Mattig, H. Spiesberger, and W. Zeuner, "On the Comparison of Matrix Element Calculations of $O(\alpha\alpha_s)$ with the Measurement of Photon Emission in Hadronic Z^0 Decays," *Z. Phys.* **C60** (1993) 613–632.

[45] V. N. Gribov and L. N. Lipatov, “e^+e^- Pair Annihilation and Deep Inelastic e p Scattering in Perturbation Theory,” *Sov. J. Nucl. Phys.* **15** (1972) 675–684.

[46] Y. L. Dokshitzer, “Calculation of the Structure Functions for Deep Inelastic Scattering and e^+e^- Annihilation by Perturbation Theory in Quantum Chromodynamics. (in russian),” *Sov. Phys. JETP* **46** (1977) 641–653.

[47] G. Altarelli and G. Parisi, “Asymptotic Freedom in Parton Language,” *Nucl. Phys.* **B126** (1977) 298.

[48] F. Halzen and A. D. Martin, “Quarks and Leptons: An Introductory Course in Modern Particle Physics,”. New York, Usa: Wiley (1984) 396p.

[49] V. V. Sudakov, “Vertex Parts at Very High-Energies in Quantum Electrodynamics,” *Sov. Phys. JETP* **3** (1956) 65–71.

[50] T. Sjöstrand, “High-Energy Physics Event Generation with PYTHIA 5.7 and JETSET 7.4,” *Comput. Phys. Commun.* **82** (1994) 74–90.

[51] G. Marchesini *et al.*, “HERWIG: A Monte Carlo Event Generator for Simulating Hadron Emission Reactions with Interfering Gluons. Version 5.1 - April 1991,” *Comput. Phys. Commun.* **67** (1992) 465–508.

[52] L. Lönnblad, “ARIADNE Version 4: A Program for Simulation of QCD Cascades Implementing the Color Dipole Model,” *Comput. Phys. Commun.* **71** (1992) 15.

[53] M. H. Seymour, “Photon Radiation in Final State Parton Showering,” *Z. Phys.* **C56** (1992) 161–170.

[54] T. Sjöstrand, “Prompt Photons in Hadronic Events at LEP,”. Presented at the Workshop on Photon Radiation From Quarks, Annecy, France, Dec 2-3, 1991.

[55] B. A. Kniehl and L. Lönnblad, “Renormalization Scales in Electroweak Physics: and Photon Radiation in the Dipole Model and in the Ariadne program,”. Two papers given at the Workshop on Photon Radiation from Quarks, Annecy, France, Dec 2-3, 1991.

[56] S. Bentvelsen, “QCD Tests with High Angle Soft Photons at OPAL,”. Proceedings of the 28th International Conference on High-energy Physics (ICHEP 96), Warsaw, Poland, 25-31 Jul 1996, Vol.I (1997) 757-760.

[57] **ALEPH** Collaboration, D. Decamp *et al.*, “Measurement of Isolated Photon Production in Hadronic Z Decays,” *Phys. Lett.* **B264** (1991) 476–486.

[58] **ALEPH** Collaboration, D. Buskulic *et al.*, “Measurement of Prompt Photon Production in Hadronic Z Decays,” *Z. Phys.* **C57** (1993) 17–36.

[59] **L3** Collaboration, O. Adriani *et al.*, “Isolated Hard Photon Emission in Hadronic Z^0 Decays,” *Phys. Lett.* **B292** (1992) 472–484.

[60] **OPAL** Collaboration, K. W. Bell, "Photon Radiation from Quarks at OPAL," *Nucl. Phys. Proc. Suppl.* **64** (1998) 32.

[61] B. Andersson, G. Gustafson, and B. Soderberg, "A General Model for Jet Fragmentation," *Z. Phys.* **C20** (1983) 317.

[62] C. Peterson, D. Schlatter, I. Schmitt, and P. Zerwas, "Scaling Violations in Inclusive e^+e^- Annihilation Spectra," *Phys. Rev.* **D27** (1983) 105.

[63] S. Bethke, "Jets in Z^0 Decays,". Talk given at Workshop on QCD: 20 Years Later, Aachen, Germany, 9-13 Jun 1992. Publ. in: Proceedings P M Zerwas and H A Kastrup World Sci., Singapore (43-72) (and further references therein).

[64] **OPAL** Collaboration, P. D. Acton *et al.*, "Properties of Multi - Hadronic Events with a Final State Photon at $\sqrt{s} = M_{Z^0}$," *Z. Phys.* **C54** (1992) 193–210.

[65] **OPAL** Collaboration, K. Ahmet *et al.*, "The Opal Detector at LEP," *Nucl. Instrum. Meth.* **A305** (1991) 275–319.

[66] P. P. Allport *et al.*, "The OPAL Silicon Microvertex Detector," *Nucl. Instrum. Meth.* **A324** (1993) 34.

[67] P. P. Allport *et al.*, "The OPAL Silicon Strip Microvertex Detector with two Coordinate Readout," *Nucl. Instrum. Meth.* **A346** (1994) 476–495.

[68] J. R. Carter *et al.*, "The OPAL Vertex Drift Chamber," *Nucl. Instrum. Meth.* **A286** (1990) 99.

[69] M. Hauschild *et al.*, "Particle Identification with the OPAL Jet Chamber," *Nucl. Instrum. Meth.* **A314** (1992) 74–85.

[70] O. Biebel *et al.*, "Performance of the OPAL Jet Chamber," *Nucl. Instrum. Meth.* **A323** (1992) 169.

[71] G. Aguillion *et al.*, "Thin Scintillating Tiles with High Light Yield for the OPAL Endcaps," *Nucl. Instrum. Meth.* **A417** (1998) 266.

[72] S. Petzold, "Measurement of the Heavy Flavour and Trilinear Gauge Boson Couplings at LEP,". DESY-THESIS-1999-002.

[73] **OPAL** Collaboration, K. Kawagoe, "Calorimeters in the OPAL Detector,". Prepared for International Conference on Calorimetry in High-energy Physics, Batavia, IL, 29 Oct - 1 Nov 1990.

[74] **OPAL** Collaboration, G. Abbiendi *et al.*, "Precision Luminosity for Z^0 Lineshape Measurements with a Silicon-Tungsten Calorimeter," `hep-ex/9910066`.

[75] J.-G. An *et al.*, "A Study of the Selfquenched Streamer Mode Using a Nitrogen Laser," *Nucl. Instrum. Meth.* **A267** (1988) 396.

[76] J.-G. An *et al.*, "Influence of Gas Mixture and Primary Ionization on the Performance of Limited Streamer Mode Tubes," *Nucl. Instrum. Meth.* **A267** (1988) 386.

[77] C. Beard *et al.*, "Thin, High Gain Wire Chambers for Electromagnetic Presampling in OPAL," *Nucl. Instr. Meth.* **A286** (1990) 117.

[78] P. W. Jeffreys *et al.*, "Development Studies for the OPAL Endcap Electromagnetic Calorimeter Using Vacuum Photo Triode Instrumented Lead Glass," *Nucl. Instrum. Meth.* **A290** (1990) 76.

[79] M. D. Rousseau, R. M. Brown, P. W. Jeffreys, M. Edwards, and M. Sproston, "A Single Stage Photomultiplier / Amplifier Combination for Use in Intense Magnetic Fields. (Talk)," *IEEE Trans. Nucl. Sci.* **30** (1983) 479.

[80] P. W. Jeffreys *et al.*, "A Phototriode Instrumented Lead Glass Calorimeter for Use in a Strong Magnetic Field in OPAL,". Submitted to Int. Europhysics Conf. on High Energy Physics, Bari, Italy, Jul 18-24, 1985.

[81] R. M. Brown *et al.*, "An Electromagnetic Calorimeter for Use in a Strong Magnetic Field at LEP Based on CEREN 25 Lead Glass and Vacuum Phototriodes," *IEEE Trans. Nucl. Sci.* **32** (1985) 736.

[82] **The LEP Higgs Working Group: ALEPH, DELPHI, L3, OPAL** Collaboration, "Status of the Higgs Boson Search,". Talk given at the LEP Seminar, 3 Nov 2000.

[83] J. Allison *et al.*, "The Detector Simulation Program For the OPAL Experiment at LEP," *Nucl. Instrum. Meth.* **A317** (1992) 47–74.

[84] R. Brun, F. Bruyant, M. Maire, A. C. McPherson, and P. Zanarini, "GEANT3,". CERN-DD/EE/84-1.

[85] C. Hawkes, D. Lellouch, M. Redmond, O. Schaile, and M. Schröder, "ROPE410,". OPAL-Offline note 16/OFFL-0487.

[86] K. Kawagoe, "A Program to Fit Shower Clusters in the OPAL Electromagnetic Barrel,". TKYLEP-89, 30th May 1988.

[87] K. Meier, "Research on Photon Production by Electron - Positron Annihilation at the Petra Storage Ring,". DESY F11-84/01.

[88] E. Longo and I. Sestili, "Monte Carlo Calculation of Photon Initiated Electromagnetic Showers in Lead Glass," *Nucl. Instrum. Meth.* **128** (1975) 283.

[89] B. Rossi, "High-Energy Particles,". Englewood Cliffs, NJ: Prentice-Hall (1952) 569 p.

[90] G. A. Akopdzhanov *et al.*, "Determination of Photon Coordinates in Hodoscope Čerenkov Spectrometer," *Nucl. Instr. Meth.* **140** (1977) 441.

[91] G. P. Lepage, "A New Algorithm for Adaptive Multidimensional Integration," *J. Comput. Phys.* **27** (1978) 192.

[92] J. A. Nelder and R. Mead *Computer Journal* **7** (1965) 308.

[93] **OPAL** Collaboration, M. Z. Akrawy *et al.*, "A Measurement of Global Event Shape Distributions in the Hadronic Decays of the Z^0," *Z. Phys.* **C47** (1990) 505–522.

[94] **OPAL** Collaboration, P. D. Acton *et al.*, "Precision Measurements of the Neutral Current from Hadron and Lepton Production at LEP," *Z. Phys.* **C58** (1993) 219–238.

[95] R. Barlow, J. Becker, P. Clarke, G. Quast, G. Richards, T. Smith, N. Watson, and T. Wyatt, "A Detailed Description of the 1991 Muon Pair Analysis,". OPAL Technical Note TN109, 23rd July 1992.

[96] N. Oldershaw, "LEP1 Muon Pair Cross-section and Forward-backward Asymmetry,". OPAL Technical Note TN547, 8th June 1998.

[97] **OPAL** Collaboration, P. D. Acton *et al.*, "A Measurement of Photon Radiation in Lepton Pair Events from Z^0 Decays," *Phys. Lett.* **B273** (1991) 338–354.

[98] P.Mattig, "Photon Energy Resolution in the Leadglass Calorimeters,". OPAL Technical Note TN324, 9th October 1995.

[99] S. Jadach, B. F. L. Ward, and Z. Was, "The Monte Carlo Program KORALZ, for the Lepton or Quark Pair Production at LEP/SLC Energies: From Version 4.0 to Version 4.04 (and further references therein)," *Comput. Phys. Commun.* **124** (2000) 233, `hep-ph/9905205`.

[100] **OPAL** Collaboration, G. Alexander *et al.*, "Measurement of the Z^0 Line Shape Parameters and the Electroweak Couplings of Charged Leptons," *Z. Phys.* **C52** (1991) 175–208.

[101] **OPAL** Collaboration, G. Alexander *et al.*, "A Comparison of b and (u d s) Quark Jets to Gluon Jets," *Z. Phys.* **C69** (1996) 543–560.

[102] **OPAL** Collaboration, K. Ackerstaff *et al.*, "Search for Chargino and Neutralino Production at $\sqrt{s} = 170$ GeV and 172 GeV at LEP," *Eur. Phys. J.* **C2** (1998) 213–236, `hep-ex/9708018`.

[103] T. Omori, S. Asai, I. Nakamura, and S. Yamashita, "A Matching Algorithm: MT Package,". OPAL Technical Note TN381, July 1996.

[104] S. Mihara and S. Yamashita, "MT 3.00 A New Algorithm to Calculate Energy Flow Based on MT Package,". OPAL Technical Note TN574, November 1998.

[105] R. Barlow and C. Beeston, "Fitting Using Finite Monte Carlo Samples," *Comput. Phys. Commun.* **77** (1993) 219–228.

[106] F. James and M. Roos, "'MINUIT' a System for Function Minimization and Analysis of the Parameter Errors and Ccorrelations," *Comput. Phys. Commun.* **10** (1975) 343.

[107] **OPAL** Collaboration, K. Ackerstaff *et al.*, "Photon and Light Meson Production in Hadronic Z^0 Decays," *Eur. Phys. J.* **C5** (1998) 411, `hep-ex/9805011`.

[108] **L3** Collaboration, D. Kirkby, "A Study of Hadronic Backgrounds to Isolated Hard Photon Production with L3," `hep-ex/9505012`.

[109] S. Jadach, B. F. L. Ward, and Z. Was, "The Precision Monte Carlo Event Generator KK for Two-Fermion Final States in e^+e^-collisions," `hep-ph/9912214`.

[110] T. Sjostrand *et al.*, "High-Energy-Physics Event Generation with PYTHIA 6.1," `hep-ph/0010017`.

[111] **OPAL** Collaboration, R. Akers *et al.*, "The production of Neutral Kaons in Z^0 Decays and their Bose-Einstein Correlations," *Z. Phys.* **C67** (1995) 389–402.

[112] S. Jadach, B. Pietrzyk, E. Tournefier, B. F. L. Ward, and Z. Was, "Initial-Final-State Interference in the Z Line-Shape," *Phys. Lett.* **B465** (1999) 254, `hep-ph/9907547`.

[113] **OPAL** Collaboration, R. Akers *et al.*, "Measurement of Single Photon Production in e^+e^- Collisions near the Z^0 Resonance," *Z. Phys.* **C65** (1995) 47–66.

[114] **OPAL** Collaboration, R. Akers *et al.*, "Comparisons of the Properties of Final State Photons in Hadronic Z^0 Decays with Predictions from Matrix Element Calculations," *Z. Phys.* **C67** (1995) 15–26.

[115] **OPAL** Collaboration, P. D. Acton *et al.*, "A Global Determination of $\alpha_s(M_{Z^0})$ at LEP," *Z. Phys.* **C55** (1992) 1–24.

[116] D. Kirkby, "QCD Corrections to Isolated Hard Photon Production in e^+e^- Annihilation,". CALT-68-1822.

[117] T. Sjostrand, "PYTHIA 5.6 and JETSET 7.3: Physics and Manual,". CERN-TH-6488-92.

[118] J. E. Campagne and R. Zitoun, "The DYMU2 Event Generator,". In *Brighton 1989, Proceedings, Radiative corrections* 271- 287. (see HIGH ENERGY PHYSICS INDEX 29 (1991) No. 8663).

[119] **OPAL** Collaboration, K. Ackerstaff *et al.*, "Measurement of the Branching Fractions and Forward-Backward Asymmetries of the Z^0 into Light Quarks," *Z. Phys.* **C76** (1997) 387–400, `hep-ex/9707019`.

[120] M. A. Thomson, "The Use of Maximum Entropy in Electromagnetic Calorimeter Event Reconstruction," *Nucl. Instrum. Meth.* **A382** (1996) 553–560.

[121] J. Steuerer. Private Communication.

Acknowledgements

An dieser Stelle möchte ich die Menschen erwähnen, die mich in den Jahren der Entstehung dieser Arbeit begleitet haben.

Bedanken möchte ich mich zunächst bei Herrn Prof. Wagner, der mir die Besuche von Plenarwochen, Workshops und Sommerschulen ermöglichte. Die Montagsmeetings stellten immer echte Prüfsteine für mich dar und halfen mir gleichzeitig, meine Arbeit regelmäßig kritisch zu überprüfen.

Mein Dank gilt auch Herrn Prof. Heuer, der sich um die Weiterfinanzierung meiner Arbeit kümmerte und mir damit ermöglichte, dieselbe zu einem Ende zu bringen.

Besonderen Dank an Dr. Ties Behnke, Dr. Klaus Desch und Dr. Wolfram Zeuner, die durch konstruktive Kommentare zu dieser Arbeit beigetragen haben.

Den anderen Mitgliedern der Gruppe F-LC sei auch gedankt. Sie haben mir insbesondere in der Endphase meiner Arbeit sehr geholfen. Mathieu vielen Dank für den Tip, daß es manchmal besser ist, ganz neu anzufangen. Auch dem assoziierten F-LC-Mitglied Stefan Schmitt vielen Dank für hilfreiche Diskussionen zu meiner Analyse.

Nicht vergessen möchte ich, mich bei den Mitgliedern der ehemaligen Gruppe F-OPAL zu bedanken, besonders bei Silke und Christoph, Diamant-Alex und Jens, deren humorvolle Art ich sehr schätze.

Herzlichen Dank an Sandra, Andrea, Hollywood, Magnum, Siegfried, Martin, Kristian, Markus, Daniela und Carsten für gute Unterhaltungen dies- und jenseits der Physik. Carsten gilt sowieso mein besonderer Dank — für das reibungslose Funktionieren der “Zweck-WG” und vieles mehr.

Mein größter Dank gilt meiner Familie, meinen Eltern und meinem Bruder, die mich mit ihrer herzlichen und humorvollen Art immer wieder daran erinnert haben, was wirklich wichtig ist.